



SAPIENZA
UNIVERSITÀ DI ROMA

Automatic tolerance inspection through Reverse Engineering: a segmentation technique for plastic injection moulded parts

Facoltà di Ingegneria Civile e Industriale

Corso di Dottorato in Ingegneria Industriale e Gestionale

XXX Ciclo

Michele Bici

Matricola n° 1047404

Advisor

Prof.ssa Francesca Campana

Co-advisor

Alessio Trifirò

Ph.D. Thesis

Academic Year: 2016/2017

*The task is, not so much to see
what no one has yet seen; but to
think what nobody has yet
thought, about that which
everybody sees.*

(Erwin Schrodinger)

*...audacia opus est; nemo nisi
victor pace bellum mutavit.*

(Gaius Sallustius Crispus, *De
Catilinae coniuratione*, 58)

*To Romano, for teaching me that
“family is the most important
thing you have, especially when it
seems you cannot bear it
anymore”.*

Summary

Abstract and thesis structure	1
Chapter 1 – State of the art and introduction.....	3
1. <i>Reverse Engineering techniques in industrial engineering ..</i>	<i>3</i>
2. <i>Research topics in Reverse Engineering</i>	<i>6</i>
3. <i>Reverse Engineering in product inspection</i>	<i>10</i>
4. <i>Reverse Engineering for injection moulding</i>	<i>13</i>
4.1 <i>Injection Moulding Process</i>	<i>13</i>
4.2 <i>Requirements for die set-up inspection via RE</i>	<i>18</i>
Chapter 2 – Inspection hardware and data protocol	21
1. <i>An overview of the acquisition methods</i>	<i>21</i>
1.1 <i>Non- contact methods.....</i>	<i>22</i>
1.2 <i>Contact methods.....</i>	<i>25</i>
2. <i>System performance and hardware selection</i>	<i>27</i>
3. <i>Acquisition strategy and set-up.....</i>	<i>35</i>
Chapter 3 – RE post-processing for automatic recognition	41
1. <i>Problem Description</i>	<i>41</i>
2. <i>Formulation</i>	<i>43</i>
2.1 <i>Voxel definition</i>	<i>43</i>
2.2 <i>Local surface recognition via threshold analysis.....</i>	<i>47</i>
2.3 <i>Fitting of surfaces</i>	<i>50</i>
2.4 <i>Sensitivity analysis for Ransac parameters.....</i>	<i>54</i>
2.5 <i>Region growing</i>	<i>59</i>
3. <i>Workflows of implemented strategies</i>	<i>62</i>
3.1 <i>Overview of the implementation.....</i>	<i>65</i>
3.2 <i>Usage of Parallel Computing.....</i>	<i>65</i>
4. <i>Discussion</i>	<i>68</i>

Chapter 4 – Set-up and evaluation of the algorithms	71
1. Materials and methods	71
2. Voxel structure and local surface recognition	72
2.1 Din Rail Clip	72
2.2 Flange for Aeronautical Applications	80
3. Threshold for surface recognition	87
3.1 Threshold transferability.....	91
4. Fitting for cylinders and curved surfaces	92
4.1 Intrinsic Reference System and LM(Kasa) algorithm	92
4.2 MLESAC algorithm.....	95
5. Discussion	100
Chapter 5 –Measure and data management	103
1. Inspection data management	103
1.1 Inspection workflow and automation	103
1.2 PDM	107
2. Standards and practice to assess the measures	110
2.1 Proposed approaches	112
3. Summary of the expected errors	116
3.1 Post-processing a Johansson block.....	117
4. Discussion	119
Chapter 6 - Case studies	121
1. Presentation of the case studies	122
1.1 Cover.....	123
1.2 Test Button.....	129
1.3 Latching Lever.....	137
1.4 Handle	145
Conclusions	153
Acknowledgements	157

List of Tables	165
References	167
Annex 1	181

Abstract and thesis structure

This work studies segmentations procedures to recognise features in a Reverse Engineering (RE) application that is oriented to computer-aided tolerance inspection of injection moulding die set-up, necessary to manufacture electromechanical components. It will discuss all steps of the procedures, from the initial acquisition to the final measure data management, but specific original developments will be focused on the RE post-processing method, that should solve the problem related to the automation of the surface recognition and then of the inspection process.

As it will be explained in the first two Chapters, automation of the inspection process pertains, eminently, to feature recognition after the segmentation process. This work presents a voxel-based approach with the aim of reducing the computation efforts related to tessellation and curvature analysis, with or without filtering. In fact, a voxel structure approximates the shape through parallelepipeds that include small subset of points. In this sense, it represents a filter, since the number of voxels is less than the total number of points, but also a local approximation of the surface, if proper fitting models are applied.

Through sensitivity analysis and industrial applications, limits and perspectives of the proposed algorithms are discussed and validated in terms of accuracy and save of time. Validation case-studies are taken from real applications made in ABB Sace S.p.A., that promoted this research. Plastic injection moulding of electromechanical components has a time-consuming die set-up. It is due to the necessity of providing dies with many cavities, which during the cooling phase may present different stamping conditions, thus defects that include lengths outside their dimensional tolerance, and geometrical errors.

To increase the industrial efficiency, the automation of the inspection is not only due to the automatic recognition of features but also to a computer-aided inspection protocol (path planning and inspection data

management). For this reason, also these steps will be faced, as the natural framework of the thesis research activity.

The work structure concerns with six chapters. In Chapter 1, an introduction to the whole procedure is presented, focusing on reasons and utilities of the application of RE techniques in industrial engineering. Chapter 2 analyses acquisition issues and methods that are related to our application, describing: (a) selected hardware; (b) adopted strategy related to the cloud of point acquisition. In Chapter 3, the proposed RE post-processing is described together with a state of art about data segmentation and surface reconstruction. Chapter 4 discusses the proposed algorithms through sensitivity studies concerning thresholds and parameters utilised in segmentation phase and surface reconstruction. Chapter 5 explains briefly the inspection workflow, PDM requirements and solution, together with a preliminary assessing of measures and their reliability. These three chapters (3, 4 and 5) report final sections, called “Discussion”, in which specific considerations are given. Finally, Chapter 6 gives examples of the proposed segmentation technique in the framework of the industrial applications, through specific case studies.

Chapter 1 – State of the art and introduction

1. Reverse Engineering techniques in industrial engineering

In industrial engineering, the creation or retrieve of geometrical models from existing objects has now become a routine. A common interpretation of the phrase “Reverse Engineering”, first used in few publications in the 1970s revolves around copying an original (Bradley & Currie, 2005). In these terms, Reverse Engineering pertains to “imitation”, meaning the process of replicating the performance of an existing product in one or more of its performance areas (Knight, et al., 2009). By this, derives that RE processes can be used by companies for benchmark purposes, to maintain a competitive position, through the extraction of specification from competitors’ products or by military powers to take an advantage over antagonists, making a “reverse-engineering” of whatever equipment they can get. However, in these cases, the definition of Reverse Engineering as reported, limits the discussion to simplify the process of information extraction.

In a broader sense, Reverse Engineering (RE) can be defined as the creation of a set of specifications for an existing part by someone different from the original designers (Rekoff, 1985). According to this, nowadays, RE technology allows the creation of a digital model using data collected from an existing component and it is essentially based on analysis and measurement of a specimen or a set of them. Researches from areas such as image processing, computer graphics, advanced manufacturing and virtual reality has converged around creating a computer-based representation of the authentic component. While conventional engineering transforms engineering concepts and models into real parts, in RE, real parts are transformed into virtual models and concepts. The existence of a computer model provides enormous gains in improving the quality and the efficiency of design, manufacture and analysis.

There are many reasons to utilise Reverse Engineering as a design methodology. For example, a list of few common reasons can be (Curtis, et al., 2011):

- To have a comparison between products through a competitive benchmarking, (Harrington, 1991), (Raja & Fernandes, 2008);
- In preparation of a concrete imitation of a product, (Musker, 1998);
- To obtain technical data and information that do not exist or are not available, (Pal, et al., 2006), (Creehan & Bidanda, 2006), (Urbanic & El Maraghy, 2009), one of the main example of this reason is in architectural and cultural heritage (Núñez Andrés, et al., 2012), (Sansoni & Docchio, 2005), (Sansoni, et al., 2009);
- To obtain technical data that the original supplier is no longer willing or able to provide, (Thompson, et al., 1999), (Raja & Fernandes, 2008);
- To reduce time-to-market, (Raja & Fernandes, 2008);
- To enrich existing data and information, (Ingle, 1994);
- To be able to customise product design, in fields like dentistry or orthopaedic prosthesis (Fasbinder, 2010), (Martorelli & Ausiello, 2013) (Knopf & Al-Naji, 2001);
- To perform product verification, detecting and overcoming defects of a part (Ingle, 1994), (Bici, et al., 2017);
- To aid in product design (Hsiao & Chuang, 2003), also using measures and quality checks to perform improvements in design (Bici, et al., 2017);
- To investigate and control patent law infringement, (Ohly, 2009);
- To support in academic field or other learning environments, (Ohly, 2009), (Mowery, et al., 2004);

This list is obviously not exhaustive, but it illustrates the RE flexibility. Due to this enormous set of reasons to utilise RE technologies, it is important to know what factors increase difficulties in Reverse Engineering operations. This knowledge is beneficial, both for original designers and for who is going to obtain the digital model of the component. To reduce risks of imitation, original designers can design

products that are more difficult to be acquired by RE, thereby maintaining a market advantage over their competitors. On the other hand, the decision of applying RE techniques must be evaluated, keeping in mind time and cost that will be faced, taking into account the return of investments of such actions. In literature (Curtis, et al., 2011), (Raja & Fernandes, 2008), barriers in the RE process are investigated. A barrier to RE is anything that impedes the extraction of information about a product from the product itself (Harston & Mattson, 2010). Barriers to RE may include cases generated by the original designers, as the complexity of turbine blade surfaces or as inaccessibility of hidden or microscopic features of an embedded circuit. Sometimes, barriers are due to lacks of RE process as an inadequate measurement equipment, or even an inexperienced engineer with an inadequate knowledge and practice about the application of the RE techniques.

A common way to say RE, nowadays, is referring to the acquisition step through the words “3D scanner”. The meaning of “scanner”, compared to “photocopier” may give a good explanation of RE technology (Varady, et al., 1997). A photocopier produces a simple copy of an original piece of paper onto another piece of paper, a scanner, instead, inputs a page into a computer but can also recognize characters and figures, providing a text file or an image file. Similarly, a 3D copier can be seen as a device that machines a copy with the same shape of a solid object (e.g. the pantographic process used for making copies of keys). On the contrary, a 3D scanner not only captures raw data from the component but also interprets data, creating a model that can be completely analysed, modified and improved.

Looking at the whole Reverse Engineering process, in literature (Barbero, 2009), (Huang & Tai, 2000), (Bradley & Currie, 2005), it is possible to recognise that an ideal RE system should not only be able to reconstruct a complete geometric model of a piece, but should also be able to capture the initial design intent. With this in mind, data capture is not the unique starting point of this complex process. At the same time, automated modelling of surface often is not the only final goal, leaving the door open for more interactive, knowledge driven approaches

concerning the product development steps (comparison between original design intent and optimization evolution, tools for aiding design manufacturing, and so on). In this scenario, the surface acquisition must be correlated with other information, like physical characteristics of the object (surface aspect and texture, feature recognition), milling g-code (e.g. to control the process or to achieve tolerance), laser scan data or CMM data (e.g. to recover lack of information or to follow the part ID code during acquisition) (Anwer & Mathieu, 2016).

Finally, the correlation between RE and Rapid Prototyping must be cited, since often they are proposed as a natural duo, (Onuh, et al., 2001), (Jamieson & Hacker, 1995). Researches into the two technologies are often intersected and their fundamental application theory has become interrelated for several fields. Reasons concern with their common approach to manage the shape, basically, by slices (if we assume a laser scanner as a RE instrument) and STL format for the digitalization; and with the Rapid Prototyping ability of giving functional prototypes of the parts. They can be extremely useful in fields where aesthetic or manual interaction with the design is relevant, such as car-body and jewelry design (Fudos, 2006) (Stamati & Fudos, 2005), clinical, dental or biomedical applications. RE engineering, currently, is used also to acquire parts of human body (Knopf & Al-Naji, 2001), (Kim, et al., 2016) to produce prostheses or orthoses, directly through an Additive Manufacturing technology or producing, in an additive way, scaffolds or dies where, respectively, organs can be grown or materials with a comparable-to-real density can be moulded.

2. *Research topics in Reverse Engineering*

RE encompasses several tools and methods suitable to make digital models of real parts. As reported in (Varady, et al., 1997), (Bradley & Currie, 2005), generally, they can be divided in a sequence of four macro-steps:

1. Data Acquisition;
2. Data Processing;
3. Segmentation and Surface (or feature) Fitting;
4. CAD Model Creation.

Obviously, these phases are not clearly separated, often they can overlap and, sometimes, the whole process needs to be iterated to reach an accurate solution. Nevertheless, this division in macro-phases can help to take in mind requirements and issues to be solved.

Specific research works are present in literature for each of them. As reported, one of the main issues is *data acquisition* (or data capture). It is the process of acquiring a component through the XYZ coordinates of the points on its external surface. Result of data acquisition is the so-called cloud of points. It is managed as an array of discrete coordinates, with density and distribution related to the sensor adopted for the acquisition. Digitization can be either manual or automated, using a wide range of hardware. Some specific methods of acquisition are briefly discussed in Chapter 2, a general taxonomy consider a division between contact and non-contact methods (Varady, et al., 1997).

Data acquisition also pertains to the definition of the views necessary to acquire the whole component. It defines the problem of orientation and re-composition of multiple acquisitions. Operations of *View registration* combines these multiple sets of data, by alignment and refer them to a global coordinate system. Different strategies are adopted to solve the problem of defining certain references: (a) part positioning through datum; (b) acquisition of targets outside the component; (c) feature recognition in multiple views for data alignment; (d) best-fit alignment of the multiple views through overlapped regions. The most adopted algorithm for this step is the Iterative Closest Point (ICP), although other solutions are present in the field of image vision, point set registration. Approximations of view registration are mainly related to best-fit or feature recognition for the reference axes definition (e.g. from target spheres), (Rabbani, et al., 2007), (Sequeira, et al., 1998), (Barone, et al., 2012), (Tao & Jiyong, 2007). By this derives that multiple views must be

carefully planned and correlated with the type of alignment methods, taking care also that surface quality (reflective or not), undercuts or deep holes and complexity of shape are relevant aspects that can reduce the effectiveness of the acquisition procedures, at the same way of vibrations, neatness or bad set-ups.

Generally, after the view registration, the distribution of points has a much higher density than necessary, so data thinning methods and filters are used to select random samplings or organised subsets of points (Ali, et al., 2009), (Pauly, et al., 2002), (Moenning & Dodgson, 2003). This step is called *data filtering*. In some cases, only 10% of the original scanned points may be indispensable to reach acceptable results (Piegl & Tiller, 2001), (Dey, et al., 2001). Filters can also be applied to reduce noise provided by specific problems like surface reflection or vibrations, and, if present, some specific filters and clean-up methods can be used to remove outliers (Masuda & Murakami, 2010).

Steps 3 and 4, *data segmentation* and *surface fitting* are necessary for the CAD model creation. Different strategies and algorithms can be applied according to the final aim of the application, or the complexity of the shape. Segmentation is important for automatic recognition of the features. It divides data points into sets that can be fitted by an appropriate single surface or feature (Lee, et al., 2003), (Azernikov, et al., 2003), (Shamir, 2008). Several approaches are present in literature (Attene, et al., 2006b), like, for example, the voxel approach that is applied in bio-imaging, video-gaming and urban/industrial scenes (Aijazi, et al., 2013). They derive from image analysis and artificial vision, areas where automatic feature recognition is the main core of the problem. About voxel approach, more detailed explanations will be given in Chapter 3.

Surface reconstruction can be made by fitting or by tessellation, which is a triangular mesh, used to approximate shapes. Typically, it is a Delaunay triangulation (Okabe, et al., 1992). It means that each triangle has a circumcircle that does not contain any other points except the vertex of its triangle (Figure 1). This property makes the Delaunay

triangulation a convex hull of the points, thus of the surfaces of the cloud of points.

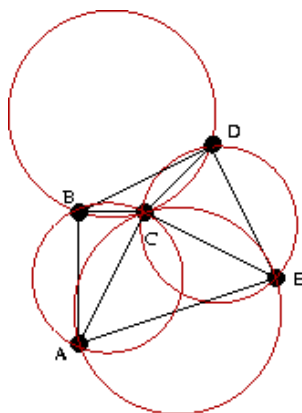


Figure 1. Example of Delaunay triangles (Peterson, 2017).

Surface fitting is applied on segment sets or can be derived by curve networks directly derived from scans. More in detail, occasional applications or extremely complex free-form surfaces may be achieved directly through surface modelling, adopting B-Spline curves directly derived from points aligned according to laser scans. In many practical cases, coupling automatic segmentation and surface fitting together with surfacing via scans can improve detail resolution of complex free forms or can fix holes due to partial data acquisitions.

Obviously, there are several peculiar applications of RE that lead to methods *ad-hoc* for each (e.g. the recognition of symmetry planes in (Di Angelo, et al., 2013), (Di Angelo & Di Stefano, 2014)). Into the universe of utilisation and development of RE methods, there are methods of RE used for quality and tolerance automatic inspection. In particular, this thesis wants to apply automatic tolerance evaluation in the injection moulding manufacturing field. For this reason, in the next section, specific topic of RE applied to tolerance inspection will be focused.

3. Reverse Engineering in product inspection

Current manufacturing environment has a continuously increasing level of competition and uncertainty. In order to stay in competition, a manufacturing system has to have characteristics of high flexibility and possibility of reconfiguration assuring that its structures or components can be adaptive. One of the major issues of being flexible for a manufacturing system is the identification of changes and uncertainties during production (Bi & Wang , 2010). RE methods and systems may help this through surfaces or features digitalization of the analysed component, identifying changes and uncertainties of the geometric shape in the respect of the nominal model.

Fields of application with high value-added, already apply RE techniques for geometrical and tolerance shape control (e.g. waveguide manufacturing, aerospace). In the automotive sector, RE is currently used for springback evaluation in sheet metal forming, like explained in (Das, et al., 2017), (Brogiato, et al., 2001). In (Amodio, et al., 2001), an original set-up suitable to analyse many stamping defect including shape deviation, is presented. Other image vision solutions, able to output the part of product shape or a view of it, are currently used for quality inspection during manufacturing.

RE techniques integrated with Computer-Aided tools for tolerancing and inspection may be seen as part of the methods suitable to implement the so-called “Smart (or Intelligent) Manufacturing” (Davis, et al., 2015). The benefits of their adoption may be enhancing predictions of manufacturing problems and improving the product-process final quality. As discussed in (Bici, et al., 2017), RE in correlation with CAT&I and PDM can help “Smart (or Intelligent) Manufacturing”, planning, automation and post processing of component inspection.

Common obstacles to more intensive application of shape digitalization for tolerance inspection are:

- data acquisition hardware and software with proper accuracy;

- automation of both experimental and post-processing steps;
- updating industrial protocol and workers knowledge.

Lack of accuracy and automation can sometimes be overcome by proper investments, and customised solutions, in particular:

- robots and CAM may help data acquisition automation and planning;
- ad-hoc research on automatic feature recognition may support and improve point-cloud post-processing;
- Product Data Management and Computer Aided Inspection tools may aid workers to change operational approach.

Many papers discuss solutions and open issues about RE in the inspection process. There are also several methods and techniques with specific pros and cons, and specific fields of usage. (Savio, et al., 2007), (Li & Gu, 2004) present a review of the state concerning inspection techniques for free-form surfaces¹, considering their difficulties in the respect of other feature-based parts. More in details in (Savio, et al., 2007), the free-form measuring post-process is discussed from the metrological point of view, starting from the geometric tolerance definition of a free form surface. According to the ISO prescriptions (ISO2011, 2004), (ISO14405-1, 2016), (ISO14405-2, 2011), for shape deviation analysis, they distinguish the necessity of a nominal surface, to be compared with the acquisition. In addition, the presence of datum is required if localization or orientation must be checked. Nevertheless, they affirm some lack of prescriptions as discussed in (Meneghello, et al., 2003), (Gabbia, 2016).

From the measurement planning point of view, both (Li & Gu, 2004) and (Savio, et al., 2007) highlight as peculiar, problems related to the adoption of RE methods. They are the registration of multiple views and the registration with the nominal CAD model for the shape comparison, together with another kind of problem that is related to free-form shapes,

¹ According to them, a free-form surface is a "complex" surface described by a set control points as it happens, for example, via NURBS.

such as sampling strategy of the measurement points. In case of registration, as already described in Section 2, the solution relies on ICP algorithms. Finally, sampling strategy of the measurement points can be approached similarly to touching probe protocol. In (Savio, et al., 2007), also the problem of uncertainty and traceability of the results is discussed. In particular, they present errors that can be distinguished in experimental and software errors. The first ones include deviation errors due to the experimental acquisition system (e.g. tip compensation in CMM contact probe, or error sources in optical methods, like reflections) or problems due to part positioning on the measurement platform (e.g. shape deformation of sheet metal or flexible parts due to gravity, clamping or device contact). The second ones pertain to errors induced by registration and reconstruction algorithms, together with file format translations. To evaluate them, traceability methods are proposed like: (a) points generation by numerical simulations; (b) calibration by parts of already known precision; (c) multiple measurement strategies comparison (see also (Martínez, et al., 2010)).

From the tolerance assessment point of view, errors in the acquisition step are critical. For this reason, contact probes with CMM are predominant in many applications. Nevertheless, as pointed out in (Li & Gu, 2004), acquisition speed and data amount of optical sensors may be suitable for many industrial applications, so that new enhancements on optical-based systems are closing the gap.

More recently, the automation of the inspection has become a discussed topic, together with the definition of a suitable workflow of the inspection process. In (Gao, et al., 2006), the concept of *Nominal Inspection Frame* is introduced to compare a digitised shape with its CAD model. This frame allows the extraction of tolerance metadata associated to the CAD model, via macros, and their attribution to the digitised shape. One of the limit of the work concerns with the fact that the definition of the *Nominal Inspection Frame* is made interactively, partially solving the automation problem. Nevertheless, its definition may support batch comparison giving a common frame, for routine comparisons.

Similar concepts are introduced in (Di Angelo, et al., 2011), (Di Angelo, et al., 2012), (Di Angelo, et al., 2013), where a nominal frame, defined as an intrinsic frame, is used to create a *Geometric Model for Tolerancing (GMT)*. This model gives a complete description of geometrical and topological parameters and other information, under a knowledge based approach. GMT is automatically generated using a process of feature recognition both in 3D CAD and in 3D scanning models (Di Angelo & Di Stefano, 2015). The control of specification in acquired model is done using a *Computer Aided Gauge (CAG)*, (Di Angelo, et al., 2017), which implements control specifications of tolerances reported in GTM. The process for product inspection and control is done through a query to measured models, having as input information obtained from the nominal 3D CAD.

Other ancillary topics concerns with data extraction and correlation of the information related to the nominal and measured values. It may help both the automation of the process, through the extraction of the tolerance prescription from the model, and the management of the information, see for examples (Campana & Germani, 2008), (Germani, et al., 2010).

Finally, concerning tolerance measurements, the inspection has to accomplish standards and problems of statistical consistence. Many works assess these relevant topics (ISO2011, 2004), (Cuesta, et al., 2009), (Martínez, et al., 2010), (Martínez, et al., 2008), (Meneghello, et al., 2003), that will be partially faced in Chapter 5 without the opinion of give an exhaustive discussion, that is far from our goals.

4. Reverse Engineering for injection moulding

4.1 Injection Moulding Process

As explained in (Bici, et al., 2014), injection moulding is a widespread manufacturing systems for high volume production. RE may play an important role to understand weakness of the product-process design, aiding the die set-up process.

Injection Moulding (or Injection Molding in American-English), is a process, ideated and patented for the first time in 1872, to obtain parts by injecting material into a mould. Materials can vary, from metals (in that case the process is called Die-Casting), glasses, elastomers, to, commonly thermoplastic and thermosetting polymers. Original material is fed into a heated barrel, then mixed and forced into a mould cavity or die, where it cools and hardens in dependence to the configuration and shape of the cavity (Todd, et al., 1994). Figure 2 gives a schematic overview of devices necessary to carry out the process.

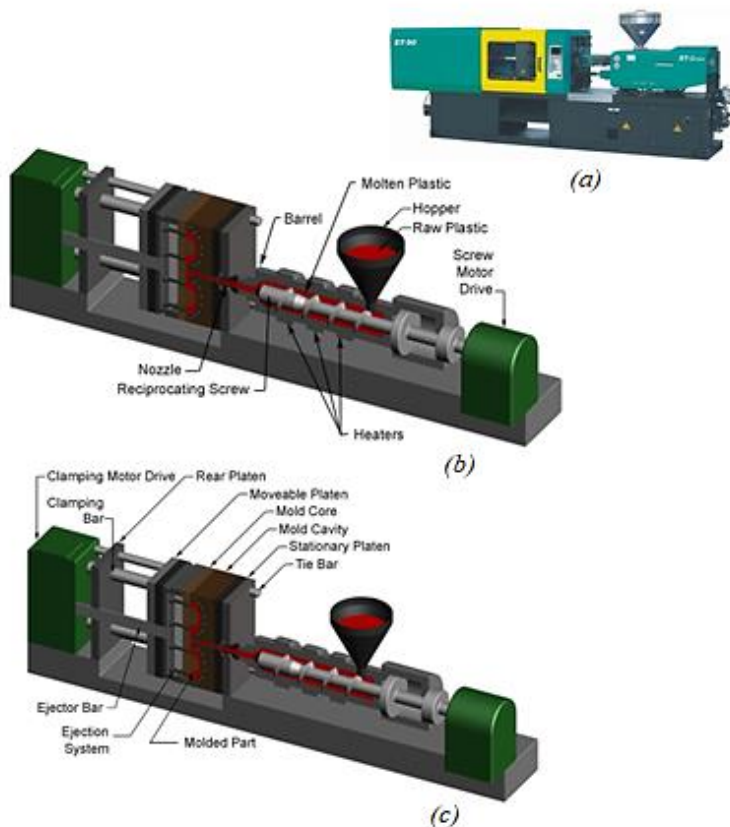


Figure 2. An example of an injection moulding machine (a), and its main components (b), (c).

Injection moulding is used, to obtain components in a wide dimensional range. Obviously, they have to be designed taking in mind problems and properties of the adopted material, machine and die. There are many types of materials that may be used in injection moulding. Most polymers may be used including thermoplastic², thermosets³ and some elastomers⁴. When these materials are used in the injection moulding process, their raw form is usually small pellet or a fine powder. Colorants can be added to control colours of final parts. The selection of a material for creating injection-moulded parts is not solely based upon the desired characteristics of the final part. While each material has different properties that will affect the strength and function of the final product, these properties also dictate the processing parameters used in processing these materials, as, for example, the injection temperature, injection pressure, mould temperature, ejection temperature and cycle time. A comparison between the most common used polymers, through their properties and applications is reported in Annex 1, at the end of this elaborate.

Injection moulding is the most common modern method of manufacturing plastic parts and it is ideal for producing high volumes of the same object. In fact, according to the length range of the part, a mould can be of a single cavity or multiple cavities. In case of multi-cavities moulds, cavities can be related to several parts or replications of a unique part. It is of the utmost importance that processes must be accurately controlled in order to obtain parts of the same characteristics and

² *A thermoplastic, or thermo-softening plastic, is a plastic material, a polymer, that becomes pliable or mouldable above a specific temperature and solidifies upon cooling (Baeurle, et al., 2006)*

³ *A thermosetting polymer, also called a thermoset, is a polymer that is irreversibly cured from a soft solid or viscous liquid pre-polymer or resin. The process of curing changes the resin into an infusible, insoluble polymer network, and is induced by the action of heat or suitable radiation often under high pressure, or by mixing with a catalyst (McNaught & Wilkinson, 1997).*

⁴ *Elastomers, elastic polymers or rubbers, are polymers with viscoelasticity (having both viscosity and elasticity) and very weak inter-molecular forces, generally having low Young's modulus and high failure strain compared with other materials. At ambient temperatures, rubbers are thus relatively soft ($E \sim 3\text{MPa}$) and deformable (Alemán, et al., 2007), (De, 1996).*

properties, especially in case of multiple identical cavities. Figure 3 shows some example of single and multiple cavities, in relation with different typologies of material adduction.

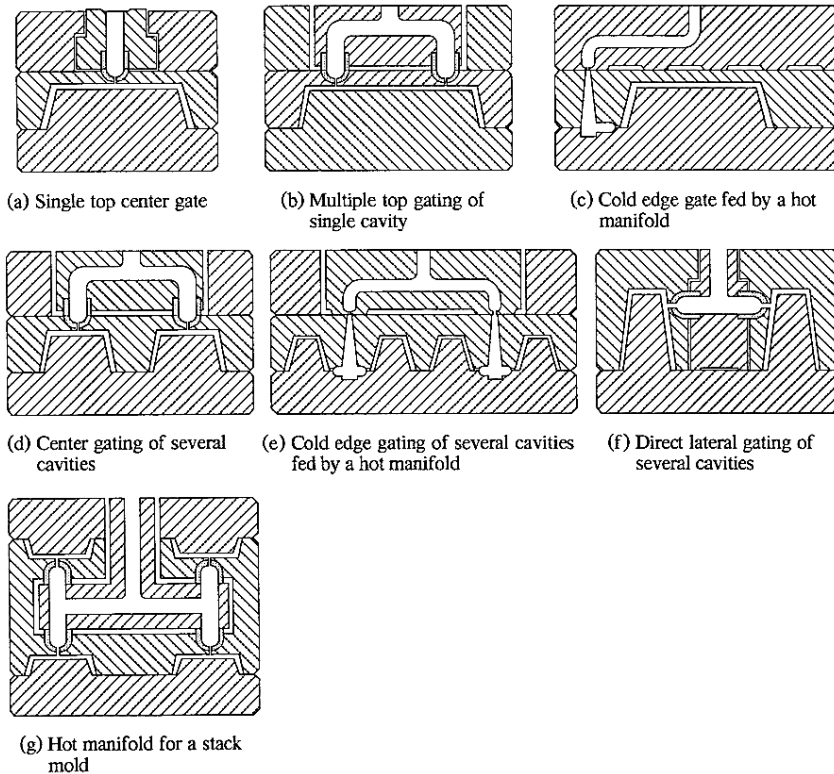


Figure 3. Different typologies of material adduction solutions.

Due to the nature of the process, injection moulded components are usually affected by undesired features like parting-line marks, sprue marks, gate marks and ejector pin marks and also by shape defects like warpage (Malloy, 1994). Gate and sprue marks occurs at gates that join the melt-delivery channels to the cavity. Parting lines, burrs and ejector pins marks (some examples are reported in Figures 4 and 5) result from several causes: misalignments, wear, gaseous vent, clearances for adjacent parts in relative motion, dimensional differences of the mating surfaces contacting the injected polymer. This last cause may be attributed to non-uniform, pressure-induced deformation during injection or non-uniform thermal expansion and contraction of mould components.

When the component is ejected from die, internal stresses, due to shrinkage, can lead to warpage, causing shape deviations connected to structure's stiffness and to the degrees of freedom (springback), reducing the durability and resistance of moulded plastic parts. The internal stresses can be relieved by annealing the part after moulding, however, there is, often, a high probability of dimensional changes, unless the part is properly fixed. Likewise, components can begin to distort or warp at elevated usage temperatures (e.g. in over for paint treatment or in a hot summer day), if residual orientation levels are high. Frozen-in orientation can cause anisotropic behaviour with respect to mould shrinkage and needed end-use properties. In literature (Xie, et al., 2010), (Sun, et al., 2006), these and other problems, connected to the characteristics of products (Song, et al., 2011), (Huang & Tai, 2001), are discussed, simulated and very often solved optimising the whole process, (Stanek, et al., 2011), (Stanek, et al., 2011b).

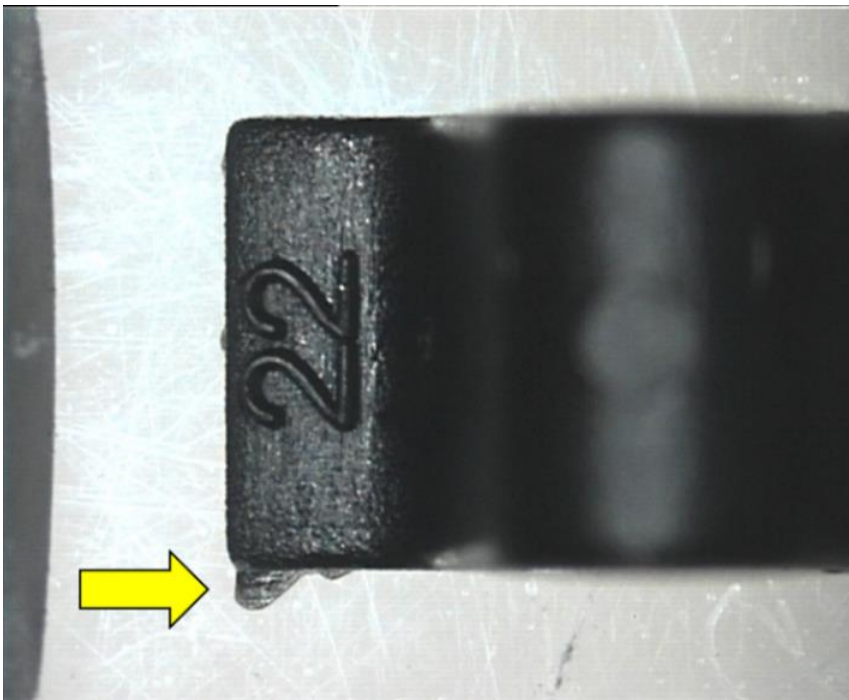


Figure 4. Example of burr.

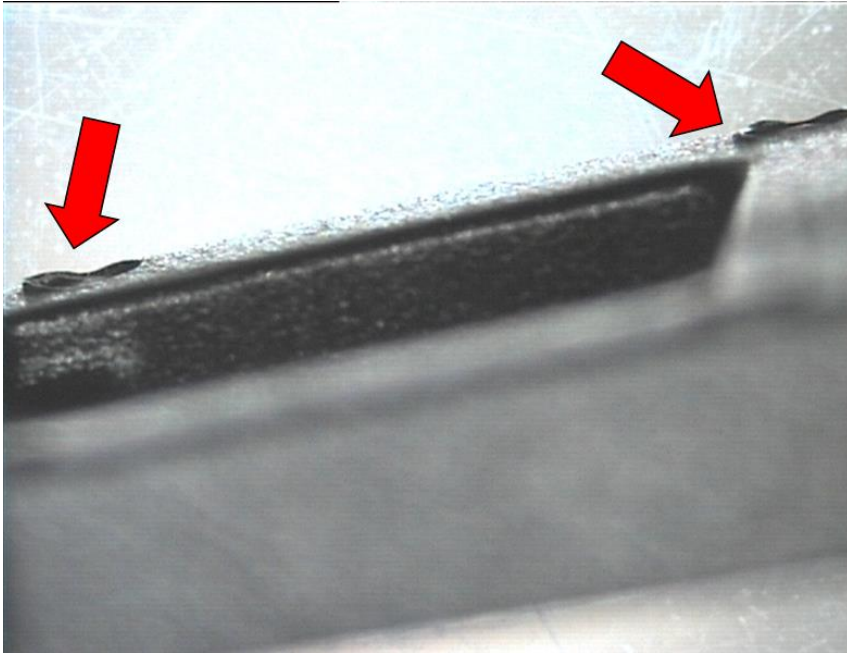


Figure 5. Example of ejector pin marks.

4.2 Requirements for die set-up inspection via RE

Many of these defects affect dimensional and geometrical tolerances of the parts. For this reason, in electromechanical assemblies, inspection of functional tolerance represents a relevant aspect to validate die design, in particular if a large amount of parts is made as multiple cavities on a single die. In the case of injection moulded parts, RE and CAT&I may play a relevant role not only in quality inspection but also in die set-up (Beiter & Ishii, 1997). For Companies with high volume of assemblies, it becomes extremely useful to evaluate supplies and manage a large number of suppliers per component, thanks to robust protocols and procedures that reduce repetitive and tedious actions and efficiently process large amounts of data (Beiter & Ishii, 1997), (Busick, et al., 1994).

This thesis discusses a segmentation technique to carry out a GD&T inspection system based on a non-contact RE digitalization system, with the aim of automatic post-processing the point clouds of multicavities

injection moulded parts. According to the reviews described in the previous sections, the automation will be made according to a CAT&I approach. It means to provide solution to achieve:

1. proper automation to the component digitalization and the acquisition paths
2. robust and accurate post-processing of the digitalised parts to measure both dimensional and geometric tolerance
3. proper automation to extract from the CAD model the requested measures and to recognise them on the digitalized parts
4. optimization of the CAT&I measurement protocol in a PDM perspective.

Although the adopted methodologies will be described as a general-purpose inspection workflow, some assumptions will be made according to the specific application made through case studies that are derived from ABB SACE electromechanical components. These components are in the dimensional range between 25-150 mm. They can be bulk components or thin shells, 0.5-0.8 mm thick. Free-form may be occasionally present. Dimensional tolerance are predominant on geometric ones, since shrinkage effects is one of the most critical defect in die set-up. Nevertheless, global deflections are interesting also, as residual stresses effects, thus as cooling problems indicators.

As common industrial practice, dimensioning prescriptions to be measured are listed in a tabular protocol that reports upper and lower bounds of the prescriptions. They can be distinguished into functional and not general prescriptions. Often they are hundreds and they must be replicated and analysed for each cavity, so to evaluate critical positions on the die and how many cavities per die are critical. It means time-consuming operations, usually made manually, with possible mistakes and confusion. In addition, suitable techniques to see the results must be thought with the aim of simplifying the dialogue among component designer, quality inspector and die supplier.

Referring to this specific industrial case:

- Chapter 2 will define the adopted digitalization hardware, its automation in terms of multiple parts acquisitions and path planning.
- Chapter 5 will discuss the strategy of the proposed PDM, highlighting its usefulness for the industrial practice in the respect of manual reporting.
- Chapter 6 will present results related to several industrial cases in order to point out advantages of the automation.

Chapter 2 – Inspection hardware and data protocol

1. An overview of the acquisition methods

As already discussed in Section 2 of Chapter 1, data acquisition (or data capture) is the starting point of an RE process. There are many different methods and technologies used to acquire shape and data from a component, (see Table 1 at page 24). Essentially, each technology is characterised by specific mechanism or phenomenon used for interacting with surfaces or volumes of the component that has to be acquired. Mainly, RE acquisition methods can be divided in two branches:

- Non-contact methods;
 - Optical Systems;
 - Acoustic Systems;
 - Magnetic Systems.

- Contact methods;
 - CMM guided;
 - Robot arms guided;

In the first case, light, sound or magnetic fields are used to acquire; in the second one, the surface is acquired by the touch of a mechanical probe connected to several types of arm (they are also known as tactile methods). Obviously, in each type, successive specific analysis are performed to obtain a list of coordinates from the physical acquisitions, as, for example, in laser scanners, the utilisation of laser's time-of-flight to determine distance. Each single method or technology has his pros and cons. This involves that the system must be chosen carefully, paying attention to the characteristics of the component and to the possible results of acquiring compared to the desired ones.

1.1 Non- contact methods

Nowadays, non-contact methods have reached a good level of confidence for RE (Son, et al., 2002), (Carbone, et al., 2001), in particular for those based on laser scanner heads. This because of the high-speed acquisition and consequently, the reduction of the relation performance-cost. Nevertheless, historically, measurement uncertainty, for these systems, is not completely known and definable, causing important disadvantages. Researchers (Cuesta, et al., 2009) performed efforts to increase accuracy of laser systems, allowing the usage in inspection systems. However, in the set of non-contact systems, several categories can be highlighted:

- Triangulation;
- Structured Light;
- Image Analysis;
- Interferometry;
- Ranging.

In *Triangulation* methods, position of the target point is deduced through location and angles between light sources and photo-sensing devices. Usually, the light source has a high level of energy, and it is given out at a specified angle onto the surface of interest. Through a photosensitive device, as, for example, a video camera, the light reflection of the surface is acquired, and then, with geometric triangulation of the known angle and distances, the position of a point relative to a reference plane can be calculated. Both light source and camera may be placed on a moving platform in order to acquire multiple scans. The most common used high-energy light source is laser. Through triangulation methods, data can be acquired with very fast rates. The accuracy depends by the resolution of the photosensitive device and by the distance between scanners and surfaces. (Barbero & Ureta, 2011). They are the most common laser systems (laser stripes), because of their higher precision and lower cost with regard to other non-contact systems such as structured light or image analysis. Scanning Laser Heads, Stereo-Vision Systems, and Photogrammetric Systems are part of this category.

Under this point of view, *Structured Light methods* can be seen as particular type of triangulation. These methods, among which is included the Moirè method, are used through the projection of light patterns upon a surface, capturing an image of the resulting pattern reflected by the component. Then, the resulting image must be analysed in order to obtain coordinates of surface points. These methods can acquire large amounts of data with a single image. In spite of this, the image analysis can be very complex.

In addition, *Image Analysis* are similar to the structured light ones, but they do not rely on projected patterns, using stereo pairs in order to obtain enough information to determine height and coordinate position. This type of methods are difficult to be used, because of the complex correlation of image pairs and of the research of landmarks in them. Some examples of these methods are Shape from X and Texture Gradients.

Interferometry methods can measure distances through wavelengths utilising interference patterns. These methods have a very high level of accuracy due to the fact that visible light has a wavelength of the order of hundreds of nanometres (nm), compatible with most of the RE applications. Obviously, in some applications, other parts of the electromagnetic spectrum can also be utilised. Practically, through a light source of high energy both a beam of monochromatic light to probe the components and a reference beam for comparison with the reflected light can be provided.

There are, obviously, several other methods, for example *Ranging* ones which are based on the measurement of time-of-flight of a light ray, typically laser or pulsed light.

A resume of specific properties of each considered non-contact method is reported in Table 1.

	Sensibility	Speed	Robustness	Performance / costs
Laser Triangulation	+ -	+	+ -	+
Structured Light	+	++	+ -	++
Stereo Vision	+	-	-	+
Photogrammetry	+	-	+ -	+ -
Time of flight	+	-	+	-
Interferometry	++	+	+ -	+ -
Moiré fringe range Contours	+ -	+	-	-
Shape from focusing	-	++	-	+ -
Shape from shadows	-	++	-	+ -
Texture gradients	-	+	+ -	+ -
Shape from shading	-	++	-	+ -

Table 1. List of non-contact acquisition methods and general comparison regarding some properties (sensibility, speed, robustness, relation between performances and costs), (Broggiato, et al., 2002).

Other methods can be included in the non-contact set, but seen as hybrid. In fact, for these techniques, sensors must be in contact or drowned with mediums of wave propagation. These types of data acquisition methods are acoustic, in which sound waves are reflected by a surface, and magnetic, in which a magnetic field is interfaced with the surface. Acoustic methods have been utilised, for a long period, for distance measuring, e.g. the sonars. Sometimes acoustic methods have been integrated into automatic focus cameras in order to determine range, with a method similar to the time-of-flight one, launching a sound wave from a source, making it reflected of by a surface, calculating the distance by the knowledge of sound speed. Often, these methods have interference

or noise problems, in addition to a low level of accuracy. Measurement of a magnetic field involves an evaluation of the strength of a magnetic field source. Though the usage of magnetic touch probes, it is possible to obtain the location and the orientation of a stylus within the field. Usually, a trigger allows the user to record only specific point data, when the stylus is positioned at a point of interest. Magnetic resonance is utilised in application similar to the ultrasound methods, in order to acquire internal material and defects. For example, MRI (Magnetic Resonance Imaging) activates atoms in the material, measuring the response.

1.2 Contact methods

The other branch of RE method is represented by *contact (or tactile) methods*. They use mechanical arms to touch the surface and obtain a data acquisition, determining the relative coordinate locations through the placement of sensing devices in the joints of the arms. These methods are limited by the physical constraints on measuring devices. For example, a tactile measuring system can be obtained mounting a touch probe on a 3-axes milling machine, but it could not be useful for acquiring concave surfaces. These methods are considered the most robust because of a general less noise, and more accuracy and repeatability, but they are practically not competitive in terms of acquisition speed. In fact, one of the main disadvantages of these contact systems is the high operation time required to obtain a large set of points of each surface, and this time increases as much as the surfaces to be controlled are more complex.

The most common used tactile method is with touch-trigger probes mounted on a Coordinate Measuring Machines (CMM).

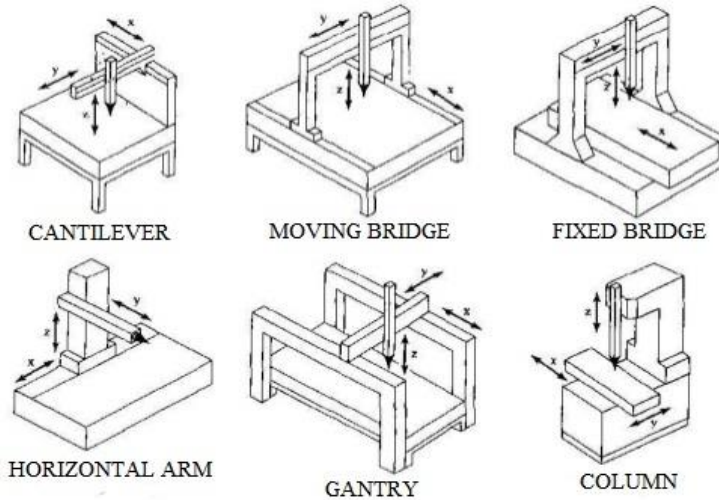


Figure 6. Different mechanical structures of CMMs.

Typically, their handling systems are 3-axes (see in Figure 6, examples of different types of CMMs) and they can be programmed to follow paths along a surface or a plane. They can collect data with a very high level of accuracy, until, in some cases, $1\mu\text{m}$, nearly noise-free. For this reason, they are used in operations for control of dimensional and geometrical tolerances (GD&T) and inspections with contact (touching probes) and non-contact (principally with laser heads) systems (Martínez, et al., 2010). In contact technologies, CMMs have the leadership for tolerance and quality control processes (Li & Gu, 2004), because of the known process of calibration of those machines and the low uncertainty in measurement. In fact, in case of non-contact systems, the uncertainty has values at least one order of magnitude higher than the contact ones (Feng, et al., 2001). However, in the recent years, some improvements has been performed, reaching competitive values or trying to define calibration procedures for 3D scanners similar to that defined by the ISO 10360-2 (ISO10360-2, 2009) for CMMs (Genta, et al., 2016). Contact processes with touch-trigger probes are commonly used due to their good relation between performances and costs.

Contact CMM measurement typologies depend not only by the machine but also by the mounted probe; they can be categorised into two sets:

- Point-to-point: each point is acquired at a time, and the probe leaves the surface after each acquisition of single point. One of the main con of this method is the low speed of acquisition due to all the time lost moving the probe.
- Scan: the probe is always in contact with the surface, the measurement is in a continuous manner, giving the possibility to acquire points quite faster than the point-to-point method.

Some requirements of a CMM, in order to obtain a good acquisition, can be highlighted: static and dynamic stiffness, possibility to have several blocking and grasping system in order to change orientations of pieces, accessibility for maintenance and handling easiness.

2. System performance and hardware selection

Generally speaking, every measuring method has to interact with the surface, plane, feature or internal material through a phenomenon or a union of them. The speed with which the phenomenon operates and the typical speed of the sensor device, obviously determines the speed of the data acquisition. The selected sensor type also influences the accuracy and the amount of analysis needed to compute acquired data.

Major problems, connected to the practice, in these procedures are (Varady, et al., 1997):

- *Calibration.* It is, obviously, an indispensable part of the set-up, which may influence negatively the rest of the procedure. Systematic errors may be caused by lens distortions, non-linear electronics in cameras, wrong positioning of the acquiring table, and other similar causes. Calibration operations are necessary to obtain fundamental parameters as orientations and position of cameras or probes and to determine the

values of eventual systematic sources of errors. In fact, this issue could be extremely influencing for results accuracy in non-contact systems.

- *Accessibility.* Sometimes, because of the peculiar topology or configuration of the component to be acquired, obtain usable data could be extremely difficult. Common examples of inaccessible surfaces are holes and their internal cylindrical surfaces. Generally, problems of accessibility can be solved, or attenuated, through multiple scans or acquisitions. Problems of accessibility have different connotations depending of the type of method. In non-contact ones, it depends from reciprocal orientations of scanner and component, and to the feature specific dimensions (e.g. an hole could be completely acquirable or not regards to its ratio between height and radius). In contact systems, it is also function of the dimensions of probe and handling system.
- *Accuracy.* As explained, it depends about the type of system and its quality chosen or available. In optical systems, accuracy is dependant mainly from the resolution of the used camera. In addition, distances between sensors (of both type of methods) and measured surface, and the accuracy of the moving parts or arms can contribute to the overall measurement error. In contact systems, it is influenced by the different mechanical structure of the handling systems (Figure 6).
- *Occlusion.* It is caused by shadowing or obstruction of scanners and sometimes, also, of probes. This type of issue, extremely dependant by the disposition of pieces or their conformation, is solved with acoustic and magnetic systems, or with the usage of multiple scanning ones. For contact systems, solutions, when existing, for this issue, may require different positioning and fixturing of pieces.
- *Fixturing.* Similarly to the self-occlusion or to occlusion often caused by the multi-pieces positioning, some occlusions can arise by the typology of clamping and blocking systems. Often, but only in non-contact systems, the clamping system is acquired together with the piece, becoming part of the scan data. Elimination and cleaning of fixture data can be extremely difficult and may need multiple views.
- *Multiple Views.* The usage of multiple view is important for solving problems arisen from occlusion and inaccessibility, but often they

introduce errors due to registration problems. Naturally, “view” is a term proper, conceptually, of the non-contact acquisitions, but the same problems are present in contact methods while partial point clouds need to be merged. The general problem is to define references and it can be solved in several ways, as, for example, part positioning through datum, acquisition of targets outside the component, feature recognition in multiple views or with best-fit alignment of the multiple views through overlapping operations (Rabbani, et al., 2007), (Gagnon, et al., 1994), (Yau, et al., 2000).

- *Noise and Incomplete Data.* Sometimes, elimination of noise in a data caption is not an easy issue, principally due to the fact that noise can be introduced in many ways as, for example, extraneous vibrations (for contact systems), specular reflections (in non-contact case), etc. Through filtering approaches, those problems can be moderated or eliminated but the user have to choose accurately the moment in the RE procedure when the operation of filtering has to be done. The operation of filtering may destroy the natural distribution and “sharpness” of data, resulting smoothed regions instead of sharp edges, and this process is not ever desirable because sometimes it leads to difficulties in identification of features. For missing or incomplete data, there are similar problems when a restoration operation has to be done. Missing or incomplete data are due to causes like inaccessibility and occlusions.
- *Surface Finish.* Often, smoothness and layers can affect significantly the data acquisition. In these cases, there is an increased production of noise respect to a smooth surface. Reflective coatings or layers can also affect the accuracy of optical methods. This problem is solved using white-mat paint, which unfortunately introduce a thickness of material that, in some ranges, can influence the measurement.

All the explained problems become fundamental while we are approaching a control of tolerance and quality on injection moulded pieces. In our research, the aim is automatic tolerance inspection of injection moulding pieces, obviously affected by manufacturing problems, like those just explained. In addition, there are issues connected

to the use of RE techniques that must be taken in mind, as explained in the previous paragraph.

Analysis will be conducted on components of electromechanical systems of electrical and circuit-breaker systems, produced by ABB S.p.A. using measurements to perform tolerances controls, with the target of an evaluation of components and, especially, of the dies used to mould. In this way, it could be possible to classify and evaluate suppliers and die quality, starting a continuous improvement process through modifies and re-engineering of component and/or moulds themselves.

Examples of components are shown in Figure 7. Their dimensions, in majority, vary in a range of 5÷250 mm.

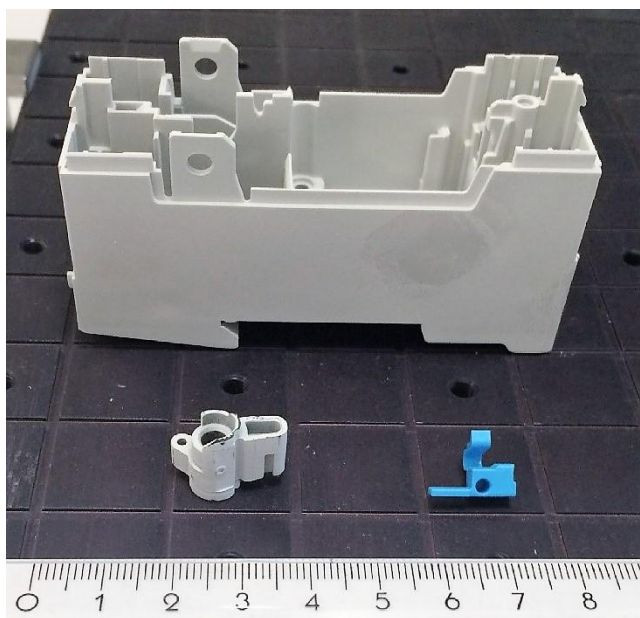


Figure 7. Examples of components with dimensional reference (cm).

They are usually moulded in multi-cavities dies, and samples, placed in different position of the die, give the possibility of evaluation of thermal effect during the whole process. Components are generally acquired putting multiple samples of the same die on the measuring table.

An example of multi-component disposition and acquisition is reported in Figure 8.



Figure 8. The laser scanner in use during the measurement of a series of components.

Taking care of the necessary requirements for speeding-up the acquisition time without losing accuracy, the adopted measured system is a CMM portal equipped by a laser scanner.

The laser scanner is a Nikon LC15Dx (Figure 9). It has a probing error of $2.5\ \mu\text{m}$ (obtained with test comparable to (ISO10360-2, 2009)) an accuracy of $3.9\ \mu\text{m}$ and the capability of acquiring approximately 70000 points/s and 900 points per line, with a resolution, in terms of point spacing, of $22\ \mu\text{m}$ (Nikon Metrology, 2017). Dimensions and values of the Field Of View (FOV)⁵ are reported in Figure 10.

⁵ *Field Of View (FOV), for optical instruments, is a solid angle through which a detector is sensitive to electromagnetic radiation.*



Figure 9. Nikon LC15Dx Laser Scanner.

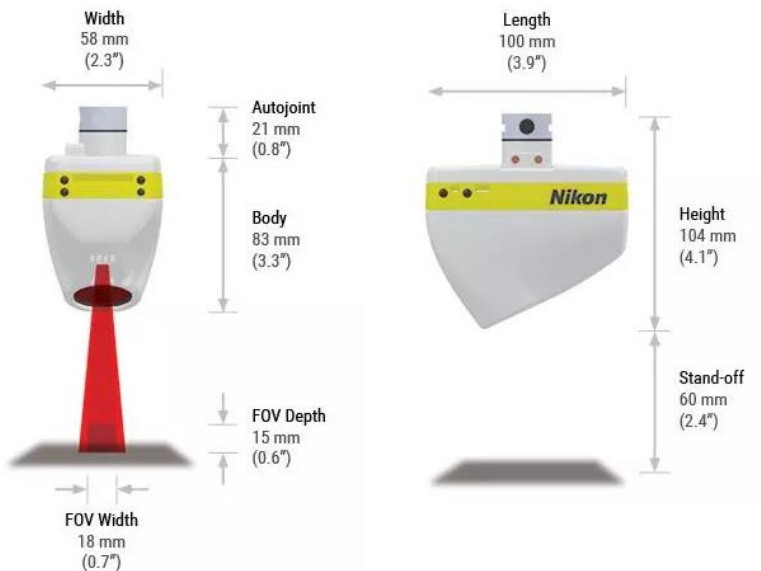


Figure 10. Dimensions and FOV of the Nikon LC15Dx (Nikon Metrology, 2017).

The CMM is a CMM 3COORD Hera 12.09.07 (Figure 11), in order to move the scanner onto a measuring table with an area of 500 x 360 mm. It is a moving bridge portal; the general scheme of its parts is

reported in Figures 12 and 13. Its measurement volume is given by the combination of the strokes in the three reference directions: 1200 mm in X-axis, 850 mm in Y-axis and 700 mm in Z-axis. The declared positioning maximum speed is about $750 \frac{mm}{s}$. Accuracy, according to specific standards, is $1.8 + \left(3.0 \times \frac{L}{1000}\right) \mu m$, in which L , expressed in mm, is the dimensional extension of the movement. Therefore, the range of accuracy, with the mentioned strokes, is about $2 \div 6 \mu m$.



Figure 11. CMM 3Coord Hera 12.09.07.

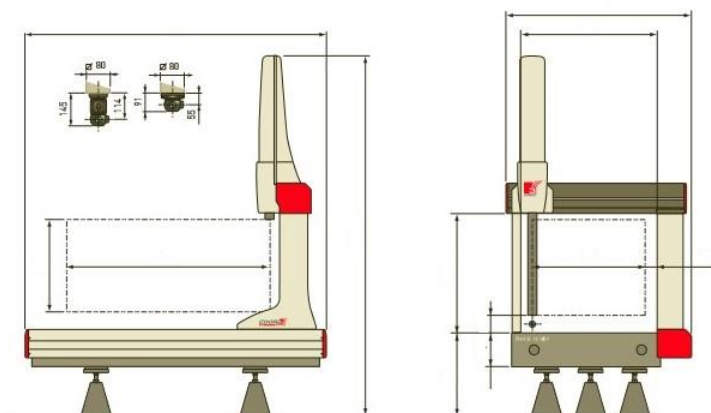


Figure 12. Scheme of the CMM 3Coord Hera 12.09.07.

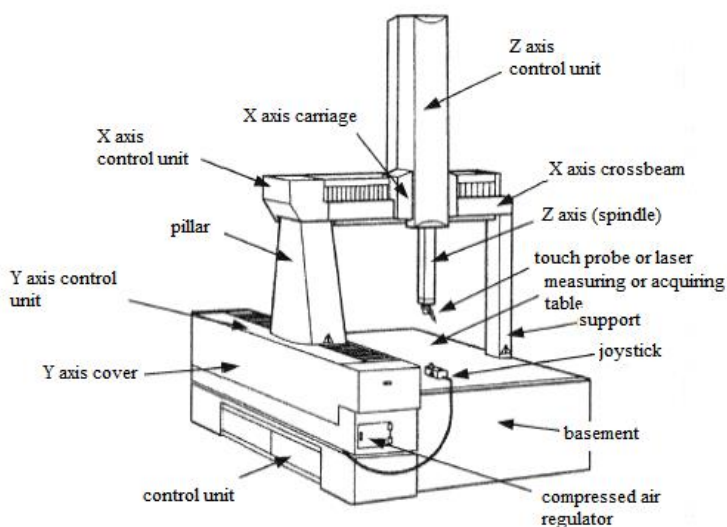


Figure 13. Scheme of principal elements of a moving bridge CMM.

This system affords a good balance between acquisition time and accuracy (Lee & Park, 2000), (Prieto, et al., 2002). These characteristics confirm the applicability of laser scanning for the tolerance inspection of plastic injection moulded components since, in the considered dimensional range (5÷250 mm), they, typically, have dimensional tolerance in the range of 0.05 ÷ 0.5 mm.

3. Acquisition strategy and set-up

An optimal scanning path plays a key role in accurate feature recognition and reduction of operational time. In fact, having a dense and complete point cloud with low noise is relevant for the accuracy of the measurement, while automatic and safe path definition are used to manage the acquisitions, especially in multi-component scanning sessions.

One of the main principles that must be firmly taken in mind while an RE inspection has to be done onto several samples is that one “real” component represents just an element in a distributed population, even considering the tolerance distribution of the scanned part. This causes frequently, in addition to the possibility of multi-component acquisitions, also the needing of multiple single part scans, obtaining an average data evaluation.

To obtain a reliable measurement campaign, orientation of pieces and their layout on the reference table must be optimised, not only in respect of the acquisition parameters but also considering that a large number of small size components must be evaluated and scanned together in each acquisition (typical scanned components have characteristic dimensions from 5 to 250 mm). Algorithms for laser scanner paths must also be defined according to the target of speed optimization, keeping in mind pieces orientations and obstacles, obstructions represented by components in terms of visibility and scanner safety. Scanning without path planning may affect completeness and accuracy of data (Xi & Shu, 1999), (Ding, et al., 2016).

The scanning session, considered as a macro-area of the whole process, is one of the most time-consuming parts (about 20% to 30% of the whole measurement and evaluation campaign of a component). Therefore, it is clear that a design and optimisation of this step is fair and convenient. In order to scan completely a part, it must be firstly positioned, according to different orientations, and then acquired.

Subsequently, acquisitions of different views must be aligned and merged.

Often, industrial RE procedures for quality control are executed without any computer assistance, leaving the choice of positioning and acquisition strategy to the experience of the operator. Specific commercial software (for example Focus or Rapidform) are used for registration and for feature recognition, with low possibilities of checking and control the algorithm settings.

In order to solve these issues, our research started by the development of a Guided User Interface (GUI), as reported in Figure 14, useful for the optimization of the orientations and of the acquisition views after the component has been suitably positioned on the table. In fact, it is proved that orientation and connected acquisition views are crucial for the subsequent optimization of the data treatment (Ali, et al., 2009). Position suitability is defined in terms of:

- *Position stability*. Evaluated in terms of a component's centroid, as derived by the nominal model STL. Its projection must be inside the support area interfaced to the acquiring table.
- *Visibility*. Evaluated as the percentage of exposed surface of the piece (visible area from the laser blade).
- *Handling during positioning*. Evaluates the ease of positioning on the table in the assigned area. This is relevant because the positioning has to be made, in the majority of cases, by operators for every component to be investigated, according to each view that must be scanned.

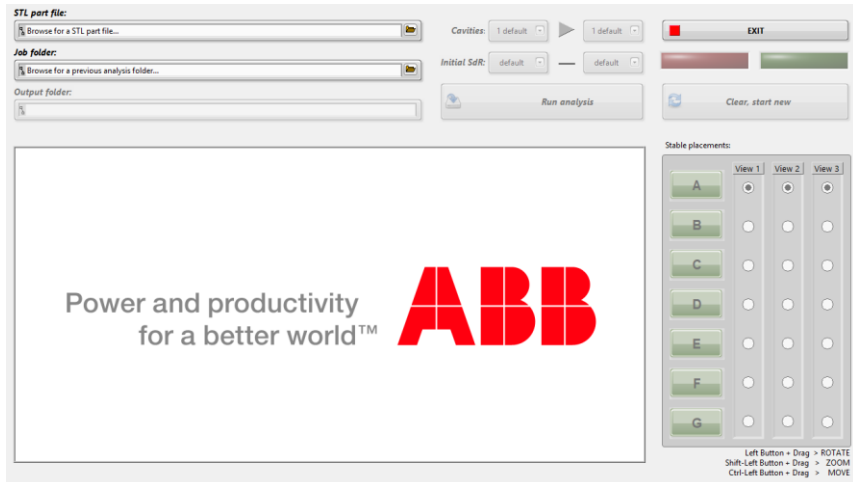


Figure 14. The developed GUI for acquisition set-up.

Through this GUI, the user can choose three positions from an ordered list of seven optimal solutions in terms of orientation (defined by a combination that maximises the above criteria). The developed routine , by default, chooses the 3 best positions (an example of three chosen positions is reported in Figure 15), in terms of balance stability, but the user can also modify the choice by selection, according other criteria, between the other proposed orientation. It is useful, especially in the case of components that are critical from an accessibility or a handling point of view (e.g. local details that reduce accessibility, or, in case of holes and pockets that could be partially acquired only in specific orientations).

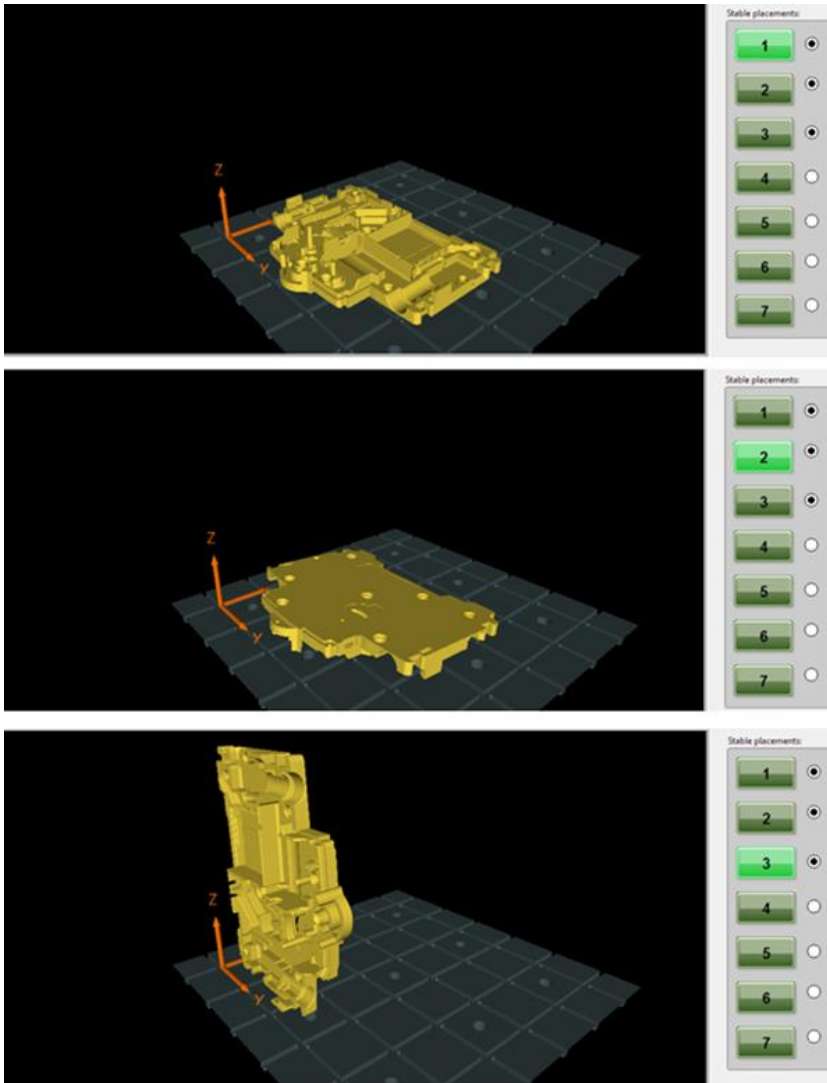


Figure 15. Example of the three optimal positions for a component.

Once three positions are defined and selected, they can be the input for the subsequent part of the process: procedures and algorithms, also integrated in the GUI, for defining the scanning views, that means finding the optimal angles and orientation of the laser scanner.

The choice of parameters for the scanning head (angles and height) depends on positioning and orientation of the piece. The developed

algorithms can automatically provide these values in order to maximise the number of acquirable points during the passage of the laser scanner. The first acquisition path will be the one that returns the maximum number of points, according to the first component position.

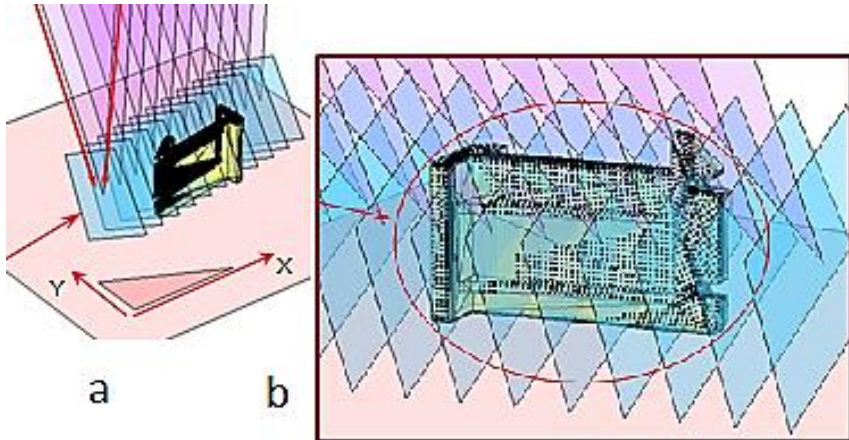


Figure 16. (a) Example of creation of paths (model of the component in yellow, acquirable zones in pointed black); (b) particular (different positions of the laser blade in cyan).

The plan of other runs is managed by maximising the number of points on the surface that have not yet been acquired. The iteration is stopped when the ongoing passage does not increase acquired points by, at least, 0.1%. At this stage, the definition of scan paths related to the first position of a piece is finished. Component position is then modified into the second position chosen. Its related paths are generated looking for maximum number of acquirable points besides that already included in paths of the first position. Scan paths of the third position are defined also to perform the “assembly match” of the clouds obtained in the previous scans. So that, the goal for path generation changes, searching points not acquired in any previous orientation and also those acquired in both scan paths of first and second position.

Other requirements and constraints for the developed algorithms of scan paths generation are:

- Exclusion of repetitions;

- Generation of codes and data driving CMM and laser scanner;
- Cleaning of points outside the component (for example, parts of the acquiring table can be scanned and they must be cut);
- Filtering (eventually) to reduce number of points, especially in wide planar zones.

Once the acquisition is made according to first, second and third positions chosen, the three obtained partial clouds must be roto-translated in order to have the same reference system. Then they are aligned and merged through a best-fit with the solid model of component (given as an IGES solid) guided by the information obtained in the “assembly match” scan paths of the third position. This merged cloud is the input for the RE post-processing and automatic recognition procedures, explained in Chapter 3. As said previously, normally, in standard procedures, this part can be very time consuming, but using the procedures and the developed GUI, the average consumed time may decrease of more than 50%.

Chapter 3 – RE post-processing for automatic recognition

1. *Problem Description*

In this chapter, the proposed algorithms for segmentation and feature recognition are described. They aim to develop an automatic partition of the point cloud, suitable to distinguish planar from curve surfaces, so that proper surface fitting and measurements can be carried out. In case of several replicated measures, as asked by multi-cavities inspection, automatic surface recognition may represent the most relevant aspect to speed up RE post-processing.

In the most general case, surface recognition is related to a proper segmentation of the points, distinguishing areas with different curvatures. This problem can be solved through different algorithms. Ordinarily, in the RE of mechanical components, gradient analysis is one of the most adopted solution (Attene, et al., 2006), (Shamir, 2008), especially in case of free-form shapes. Generally, it is applied on the tessellated surface, or on a suitable reduction obtained replacing each triangle with its centroid. Therefore, it is clear that the number of points, their density and distribution influence the accuracy of the analysis. To reduce computational time, point cloud filtering is one of the most adopted solution (Ali, et al., 2009), (Pauly, et al., 2002), (Moenning & Dodgson, 2003) but, in case of tolerance analysis and quality inspection (our aim), it may lead to a loss of data. Electromechanical components manufactured via injection moulding are characterised by planar and cylindrical surfaces with sharp angles, low thicknesses and many small ribs. In these cases, surface reconstruction of a filtered acquisition may not represent a good solution, if it must be used for tolerance inspection on a large number of samples. In fact, the risk of “smoothing” differences among the parts increases. Nevertheless, using adaptive filtering, making the segmentation and again resetting the filter can increase computational time without increasing information.

For these reasons, starting from the review works of (Shamir, 2008), we decide to work with a voxel-based approach, that localizes volumes according to a semantic significance (examples of this derive from the field of image analysis or computer vision). In the specific case of reverse engineering of mechanical parts, this segmentation is related to a problem of feature recognition, (Di Stefano, et al., 2004). The semantic significance, in this case, is a specific feature of the shape. Doing so, we can analyse the surface recognition problem according to a scale larger than the tessellated mesh, without applying preliminary filters, or classical segmentation through curvature (Attene, et al., 2006b). One of the advantages of the approach consists in avoiding mesh triangulation and point evaluation of local curvatures that are substituted with local surface reconstruction of the points inside voxels. Another peculiar point that has to be highlighted is the fact that the usage of voxel segmentation, in this way, make the amount of segmentation elements not directly dependent from the point density and distribution.

The voxel-based approach is based on a grid method similar to an octree grid derived from hierarchical space partitioning (Keller, et al., 2007) In this paper, they derive a multi-resolution mesh for complex surfaces from cloud of points. Usually, a voxel segmentation is used in acquisition of large environments in the architectural and civil engineering fields (Wang, et al., 2015), (Babahajiani, et al., 2016), or in free-form surfaces reconstructions after a MRI or CT acquisition in biomedical engineering (Dutailly, et al., 2009), (Akselrod-Ballin, et al., 2006). In our case, a 3D voxel structure is superimposed on the acquired cloud of points. It is defined through an iterative procedure that starts from a single parallelepiped. It encompasses acquired cloud completely, then, along each direction (x, y and z), it is recursively split into smaller volumes, generating a voxel structure, until no more points are included into an element or if the assigned limit of a voxel size is reached. The final structure made with the smallest size voxel represents the voxel structure of the partition (Figure 17).

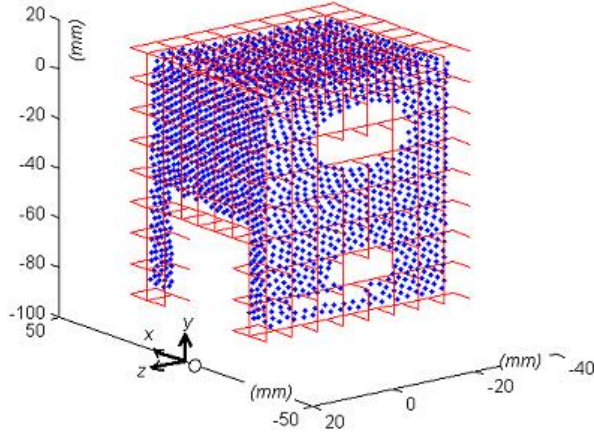


Figure 17. Example of voxel structure (red lines) encompassing a clouds of points.

2. Formulation

2.1 Voxel definition

According to the work of (Keller, et al., 2007), the first step of a voxel-based approach concerns with the definition of the voxel size that defines the resolution of the algorithm. It must be set according to the minimum component dimension interesting for the inspection. The creation of the structure starts from a single voxel (the bounding box of the whole cloud) and then, along each direction, it is recursively split into smaller voxels (every voxel is subdivided into 2, 4 or 8 smaller voxels at each iteration) until no more points are included or an imposed maximum number of subdivisions is reached. The maximum number of subdivisions determines the voxel length along the i^{th} direction, according to the equation:

$$Lenght_i = \frac{\max(P_i) - \min(P_i)}{k_i}, \quad i = x, y, z. \quad (3.1)$$

In order to reduce calculation efforts, k_i , for every direction, is recursively replaced up to reach L , M , N steps, respectively, according to numerical progressions, that are usually set as:

$$k_x = 2^r \quad r = 0, \dots, \log_2 L \quad (3.2)$$

$$k_y = 2^s \quad s = 0, \dots, \log_2 M \quad (3.3)$$

$$k_z = 2^t \quad t = 0, \dots, \log_2 N \quad (3.4)$$

where r, s, t are assumed to be the resolutions, respectively in x, y and z axes, of the algorithm, since they represent the maximum number of subdivisions reached along each direction. At every iterative step of the analysis, the voxel structure is managed as a matrix of $L \times M \times N$ elements associated to the values 1 or 0 (“true” or “false”) depending if they include points of the cloud or not. At the end of the computation, false state voxels are not considered so that the plot of true state voxels is able to represent a rough estimation of the component shape.

Figure 18 gives a schematic explanation of the procedure, assuming a 2D point distribution, along a curve. Assuming $r = s = 4$, to reach a 16×16 2D pixel structure, grey squares represent final pixels that are in “false state” ($V_{ij}=0$), the white ones that in “true state” ($V_{ij}=1$), since they encompass points. Red squares represent temporary pixels during the recursive splitting process (see equations 3.2 and 3.3). That ones with black dot lines inside represents pixels that are automatically set to 0 since no points are found inside, during the red-lines voxel preliminary evaluation.

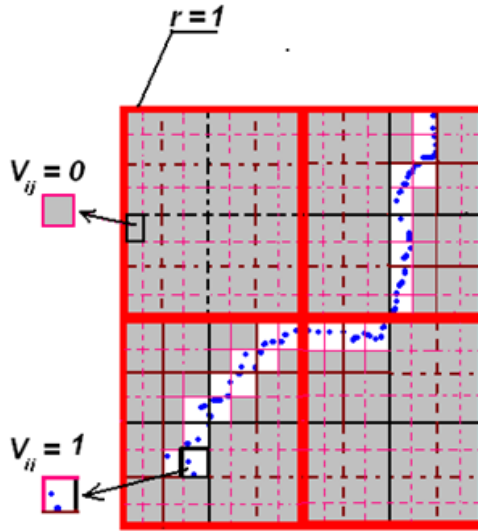


Figure 18. Structure of pixels: logical scheme for the assignment of V_{ij} .

Figure 19 shows an example of the role of the voxel length, highlighting how it is correlated to the resolution of the final shape. On the left of Figure 19, component has been divided assuming $r = s = t = 3$, obtaining 8 voxels in each dimension. Points included in each voxel, in this case, belongs generally to different features, due to the excessive voxel size. On the right of Figure 19, the same detail is described with resolution equal to $r = s = t = 5$, and the resulting 32 voxels for each direction can approximate the cloud more efficiently, due to the good relationship between voxel size and features dimensions. As a limit condition, extremely small lengths bring to one voxel per few points that means achieving something similar to a tessellation.

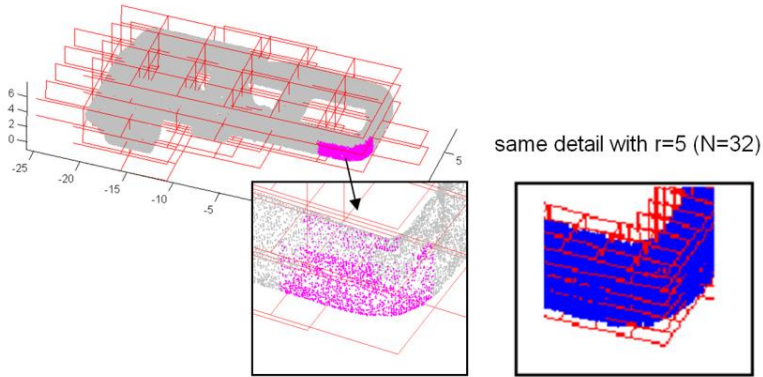


Figure 19. Effect related to a reduction of the resolution, $r=s=t$.

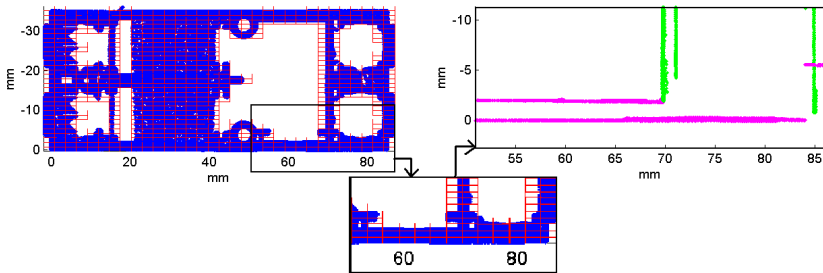


Figure 20. Plane partition for a box-shaped component with small wall thickness ($r=s=t=5$, $L=M=N=32$).

Figure 20 shows an example of voxel structure for a component with small thickness. Voxel length, in this case, is extremely important to distinguish the inner and the outer wall. This confirms the importance of a proper ratio between feature size and voxel lengths, as it will be discussed in Chapter 4.

The need of offsetting the voxel structure

Through many applications on parts from multicavities, a frequent problem of the voxel structure concerns with the possibility that some planar features could be in the boundary between two adjacent voxels. It is relevant in presence of experimental data with noise and in case of misalignments between component faces and the acquisition reference system. Although the noise may be attenuated and misalignments

avoided, this risk may be always present. In fact, it is not completely true that it may be driven only by randomness. It can be also due to the length of the voxel, $length_i$, in comparison with the smallest length of the component and its symmetry.

In order to solve this problem, the voxel structure is optimised through an offset vector, $\vec{\gamma}$. It enlarges the voxel structure, so that every planar nominal feature lies in the midpoint of its associated voxels. It means that, for each direction of the voxel structure, components of $\vec{\gamma}$ are found minimising the distances of the midpoints of the associated voxels from the CAD nominal quotes.

2.2 Local surface recognition via threshold analysis

Once the voxel discretisation is performed, local surface recognition starts through the computation of geometric descriptors. To avoid tessellation and curvature analysis, it has been based on the concept of threshold analysis. Threshold analysis is typically used in statistical modelling and also in RE (Shamir, 2008). In (Courtial & Vezzetti, 2008), a threshold to assess curvature of a RE model is derived from uncertainty of the acquisition. In our case, threshold analysis is performed on the fitting parameters associated to the points inside the voxels. Voxels in "true state" may be seen as a local approximation of the surface. Thus set of adjacent voxels related to the same surface must have similar fitting parameters, according to a threshold analysis.

Local surface recognition is carried out through best-fitting algorithms. Electromechanical parts made by injection moulding are predominantly feature-based shapes, thus plane inspection is the starting part of our segmentation. For this reason, voxels with planar surfaces are firstly detected, through threshold analysis of the fitting parameters. The threshold works on the variance of the point distances from the local plane fit in the voxel. Thanks to the accuracy of the acquisition (please, remember that our application is for tolerance), planar surfaces populate always the first bin of the variance distribution on the voxels. This can be assumed as a threshold to exclude all V_{ijk} , that are filled with points that

lay on curved surfaces. Figure 21(a) shows a typical occurrence histogram of the variance while Figure 21(b). gives an example of the results achieved through this threshold procedure.

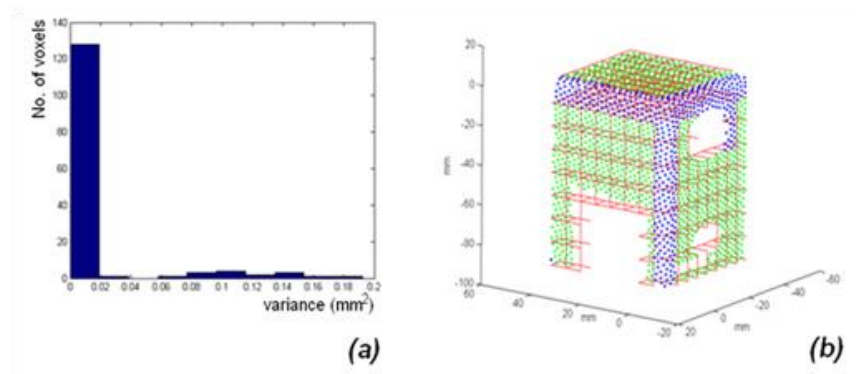


Figure 21. Plane partition: (a) occurrence histogram of the variance computed from the voxel's best-fit planes; (b) in green planar surfaces associated to the first bin of the histogram in Figure 20(a), points in blue example of small radii or non-planar region recognition.

Obviously, an accuracy problem must be faced for all the fitting parameters nearby the second bin of the histogram. This problem has been approached by an iterative threshold selection. In this case, the number of bins in the histogram are increased iteratively according to the derivative of the minimum variance of the population of voxels. When this value converges to a stable limit of saturation, the threshold is found. An explanatory example of the iterative threshold selection is reported in Figure 22, (Bici, et al., 2014b).

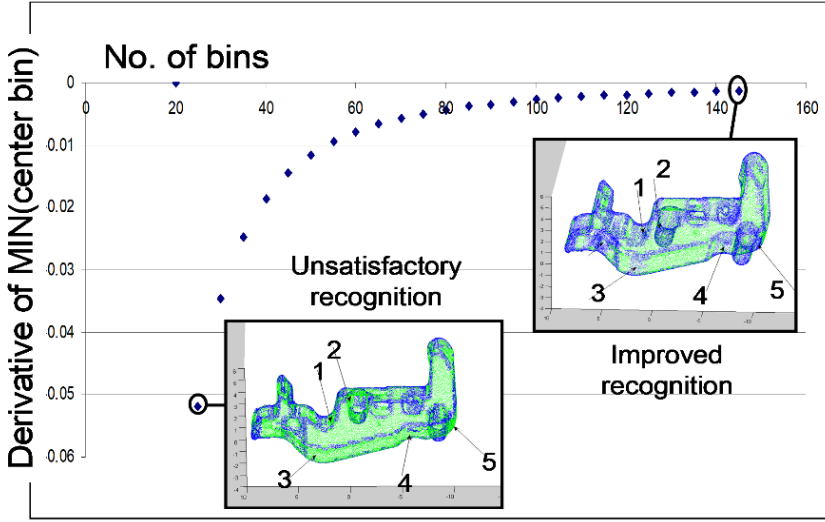


Figure 22. Iterative evaluation of variance threshold for planar voxels. Highlighted areas are discharged from planar segmentation through the derivative of the minimum bin value.

Local surface recognition is approached by fitting. Different fitting algorithms have been implemented, keeping in mind that they may be suitable for evaluating geometrical descriptors of the surfaces. In the first implementation, for each V_{ijk} in the ‘true’ state a local plane is fit by least square minimisation, made through *Single Value Decomposition* (SVD). In this case, the unknown geometrical descriptor parameters of the plane, vector \vec{x} , are found minimising the 2-norm of the over-determined linear system:

$$A\vec{x} = \mathbf{0} \quad (3.5)$$

A represents the points in the voxel, where the function to be fit is evaluated. According to the constraint:

$$\|\vec{x}\| = 1 \quad (3.6)$$

the solution is found as the right-singular vector of A , corresponding to the smallest singular value.

Voxels that do not present geometrical descriptor parameters inside the threshold are associated to “curved” local surfaces. They can be free-

form or cylindrical or boundary voxels that encompass edges of the part, with or without small chamfers or radii. In this case is necessary to use fitting algorithms to obtain an accurate surface reconstruction (Milroy, et al., 1996), (Curless & Levoy, 1996), (Azernikov, et al., 2003). In any case, finding their geometrical descriptors that means recognizing a specific type of surface, means assuming a specific equation to be fit.

2.3 Fitting of surfaces

In our case, curved surface have been post-processed according to two different strategies. The first strategy is related to a common practice in CMM inspection. As described in (Bici, et al., 2016), cylinders recognition can be reduced to circle fitting of sections. Circle fittings can be approached by geometric or algebraic fits. In the first case, the unknown parameters (position of the centre, C and radius, R) are found through an iterative regression process, for example Levenberg-Marquardt. Algebraic approaches like Taubin or Kasa, solve a system of linear equations (Kasa, 1976), (Taubin, 1991). Kasa is the fastest method that works with good results in case of complete circles but it loses accuracy in case of points along arcs with small diameters (Al-Sharadqah & Chernov, 2009). Regression approaches, like Levenberg-Marquardt, are strictly related to the adopted first-guess, moreover local minimum cannot be excluded. To avoid it, the developed application couples together Kasa algorithm and LM, referring to it as “LM(Kasa)”. The first one gives a rough estimation of the curved voxel surface that is used as first guess of the second algorithm. Figures from 23 to 26 show a comparison among the algorithms of Kasa, Taubin and LM(Kasa). More in details Figure 23 and 24 show the effects of scattered points, with a random distribution, δ , equal to (± 0.05 and ± 0.01) mm, considering a small radius ($R=3$ mm) on a small arc length. Kasa confirms its limits, while LM(Kasa) is comparable with Taubin.

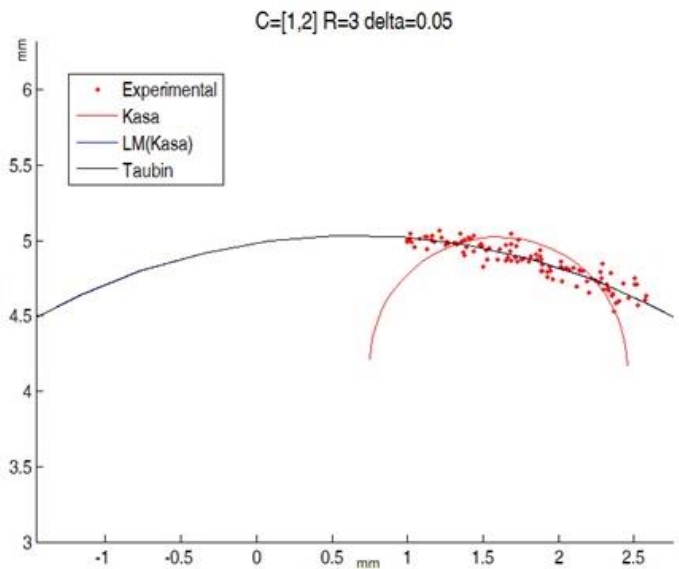


Figure 23. Comparison among Kasa, LM(Kasa), Taubin fitting a circular distribution of points, $C=[1;2]$, $R=3\text{mm}$, $\delta=0.05\text{mm}$, with small arc length.

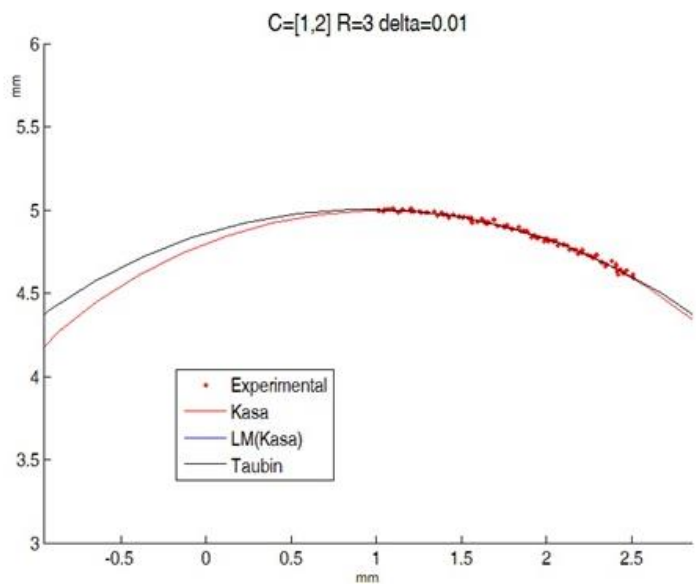


Figure 24. Comparison among Kasa, LM(Kasa), Taubin fitting a circular distribution of points, $C=[1;2]$, $R=3\text{mm}$, $\delta=0.01\text{mm}$, with small arc length.

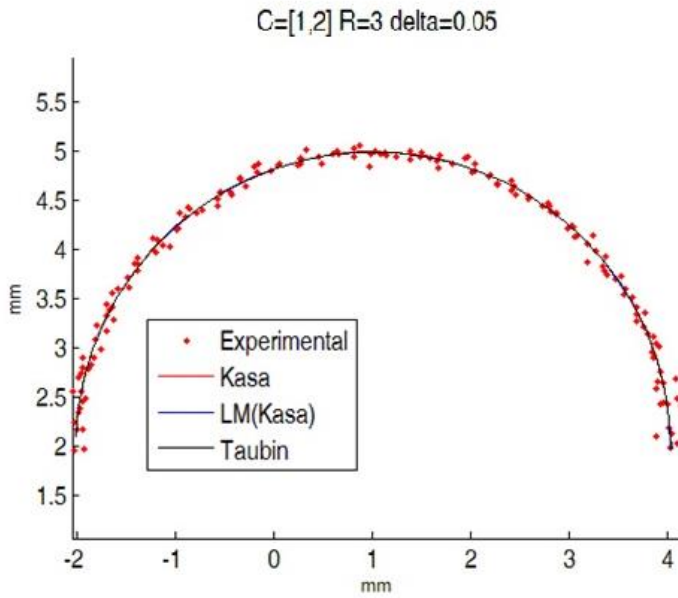


Figure 25. Comparison among Kasa, $LM(Kasa)$, Taubin fitting a circular distribution of points, $C=[1;2]$, $R=3mm$, $\delta=0.05mm$, with large arc length.

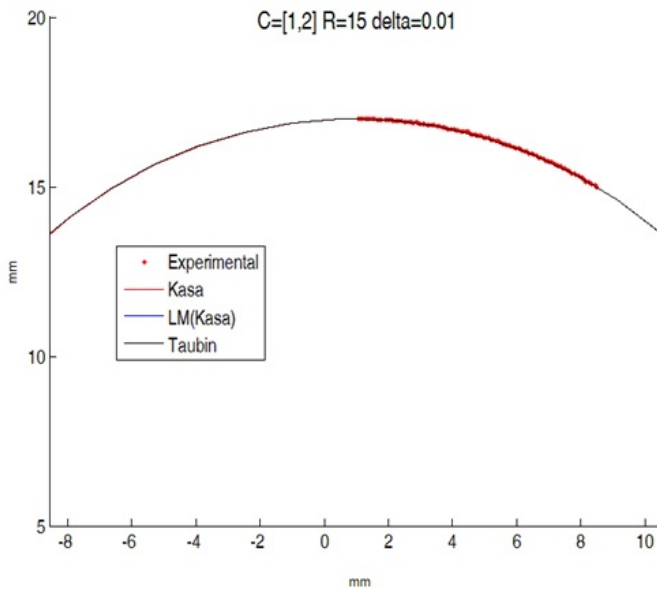


Figure 26. Comparison among Kasa, $LM(Kasa)$, Taubin fitting a circular distribution of points, $C=[1;2]$, $R=15mm$, $\delta=0.05mm$.

Figure 25 and 26 examine two other conditions. Figure 25 confirms the effect of the arc length on Kasa algorithm, while Figure 26 confirms that the adoption of greater radius improve Kasa precision. Through these LM(Kasa) is confirmed as a good competitor of Taubin algorithm.

Major problem related to LM(Kasa) approach is the necessity of finding proper projection directions, to find the circular sections. As it will be explained in section 3 of this Chapter, it can be associated to the concept of Intrinsic Reference System and to the hypothesis of having pins and holes with axes along this reference system.

To release cylinder fitting from Intrinsic Reference System, point projection may be avoided. Thus, a second fitting strategy has been investigated. It works with a Ransac-based algorithm that may help this goal, offering also a more generalized approach for all the kind of surfaces, also planes (Schnabel, et al., 2007), (Torr & Zisserman, 2000).

It is an iterative algorithm, to fit model parameters in case of data with noise. Ransac stands for Random Sample Consensus. It starts with a preliminary evaluation of the model on a minimal data set, taken randomly from the point cloud. After this, the remaining points are checked concerning their significance with the adopted thresholds (statistical confidence of the parameters, inlier maximum distance from the evaluated surface). If they are not significant, they are evaluated as “outliers”. The evolution is iterative until the confidence is reached.

Obviously, a proper model must be selected. In our case, to avoid the use of the Intrinsic Reference System, the first application of Ransac was made to fit cylinders through the points inside the curved voxels. In particular, we adopted the MLESAC (Maximum Likelihood Estimate Sample Consensus) algorithm, found in Matlab 2017, in the fitting function named “pcfitcylinder”. It starts from a sample of 6 points necessary to preliminary estimate the cylinder axis. Required thresholds are the maximum distance from the surface, to be an inlier point and the confidence (default 99%). Obviously, sometimes the algorithm may fail to evaluate an axis direction, thus a first guess must be provide. In

addition, a preliminary set-up of the proper thresholds for the maximum distance inlier-surface and confidence must be done. In the next paragraph, a preliminary study of this fitting strategy is provided, with the aim of understanding if it is suitable to improve our segmentation task.

2.4 Sensitivity analysis for Ransac parameters

To assess the required thresholds, a sensitivity analysis has been made and compared with a least-squares-error fit, interactively made in the shape workbench of CatiaV5.

Table 2 give the overview of the two set of points used for the investigation. Figure 27 and 28 show the data sets with distance analysis from the fitted surfaces.

	Point Cloud #1	Point Cloud #2
<i>No. of points</i>	2439	406
<i>Estimated radius (mm)</i>	0,9728	1.0103
<i>Axis direction (mm)</i>	[0.999, -0.007, -0.002]	[0.999, -0.360, -0.0165]
<i>Mean error (mm)</i>	0,0094	0.0055
<i>Standard dev. error (mm)</i>	0,0087	0.0033

Table 2. Fitting parameters found by CatiaV5R12.

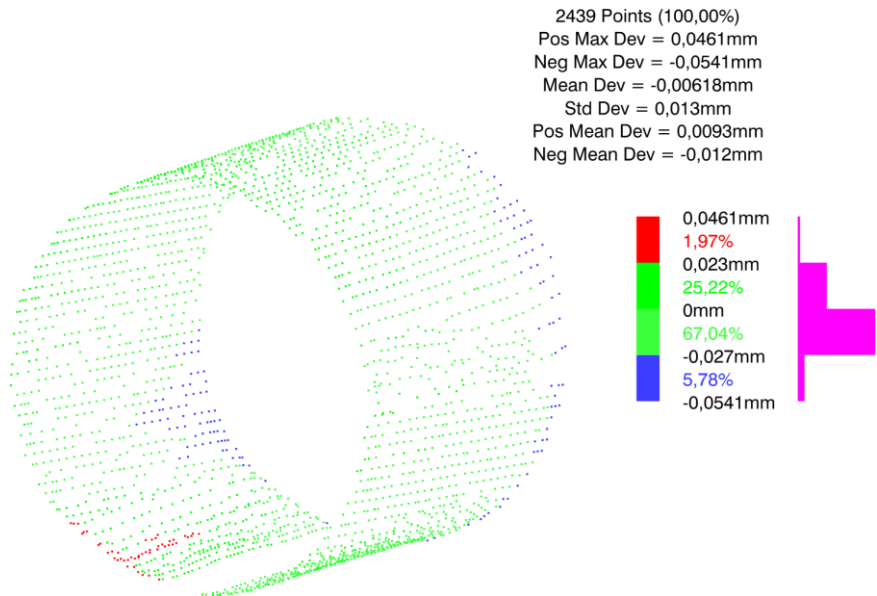


Figure 27. Point cloud #1: distance analysis from the cylinder fit made by CatiaV5R12.

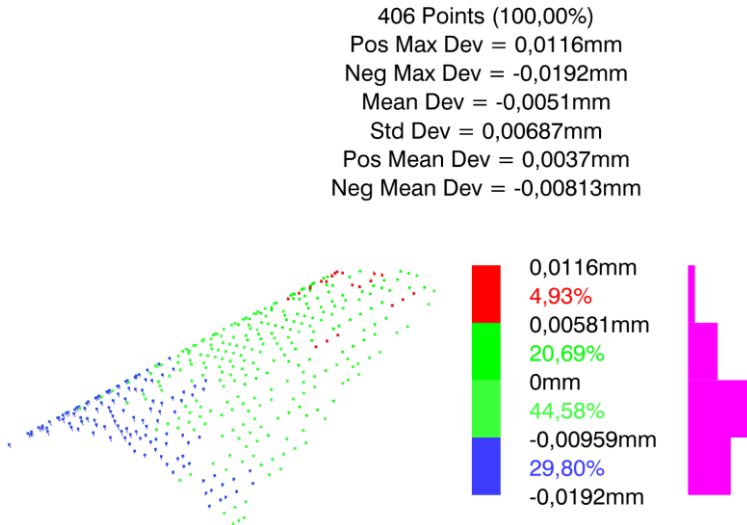


Figure 28. Point cloud #2: distance analysis from the cylinder fit made by CatiaV5R12.

Figure 29 shows a sensitivity analysis, according to the threshold that concerns with the maximum distance allowed to the inliers from the

evaluated surface. This parameter is correlated to the entity of "noise" present in the data to be fit. A reduction of this value makes more stringent the evaluation of the "inlier condition" assignable to the data points. To understand its effect, we have fit the two clouds of points, according to a vector of values, ranging from 0.0005 mm up to 0.06 mm with a step of 0.00025 mm. This vector represents the abscissa of the three plots in Figure 29⁶. The plot in the upper part of the figure, shows the fitting Mean Error according to the vector of maximum distance (in the plots it is named MaxDistance). Smaller values of MaxDistance decrease the Mean Error, and obviously the number of inlier points, used to fit the surfaces (see the lower plot of the figure). The plot in the middle represents the trend of the Radius of the cylinders, found changing MaxDistance. A stable trend can be seen nearby 0.97 mm, although an increasing interval of values, ranging from something less than 0.95 mm and something more than 1 mm. Obviously, this scattering is not suitable and consistent from a tolerance inspection point of view. It confirms the necessity of a rule to define the MaxDistance. For this reason, we decide to compare these results with that of CatiaV5R12 fit, investigating the MaxDistance range nearby the maximum deviation (0.0541 mm) found from Figure 27, the distance analysis. Doing so, we are assuming that small probability of noisy data may occur and all the points can be inserted in the MLESAC computation, similarly to what happens in the standard fit, made via CAD.

⁶ Confidence parameter set as default value, 99%

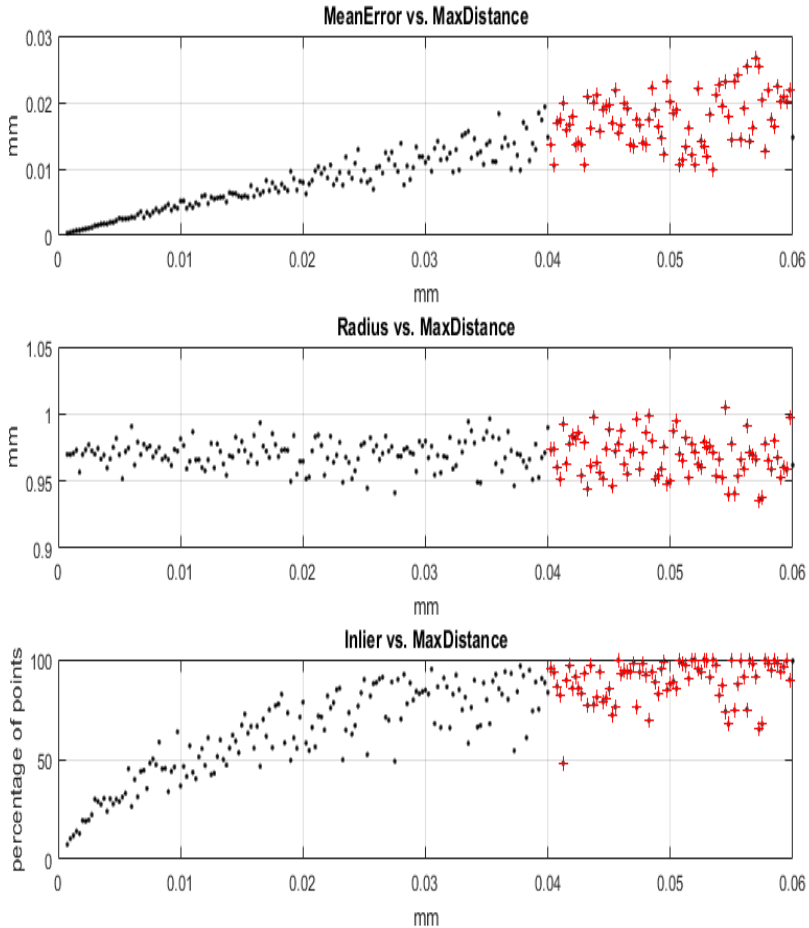


Figure 29. Point Cloud #1 - Sensitivity Analysis according to the input parameter related to the maximum distance of the inliers from the evaluated surface (MaxDistance). Upper plot: Mean Error of the fit; Middle plot: Radius of the fitting; Lower plot: percentage of inliers in the respect of the total number of points.

Red points in Figure 29 focus this reasoning, highlighting the results in a MaxDistance range equal to [0.04 - 0.06] mm:

- fitting error: 0.017 ± 0.0040 mm
- Radius: 0.9686 ± 0.0157 mm

Point Cloud #2 has been investigated to check the algorithm in the respect of a reduced arc length of the cylinder. Figure 30⁷ shows the related results. Trends of the three plots are comparable with that of Figure 29.

Red points are selected starting from the maximum deviation of Figure 28, that is equal to 0.0192 mm. In the MaxDistance range [0.015 - 0.025] mm :

- fitting error: 0.0053 ± 0.0017 mm
- Radius: 1.0117 ± 0.0644 mm

⁷ Confidence parameter set as default value, 99%

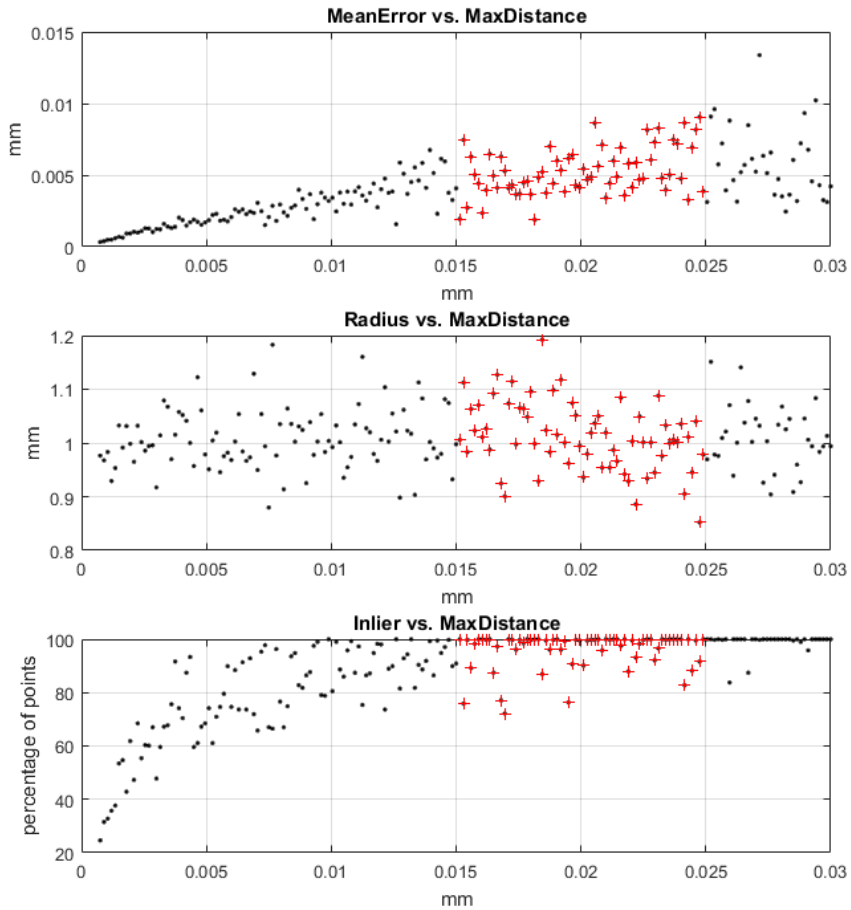


Figure 30. Point Cloud #2 - Sensitivity Analysis according to the input parameter related to the maximum distance of the inliers from the evaluated surface (*MaxDistance*). Upper plot: Mean Error of the fit; Middle plot: Radius of the fitting; Lower plot: percentage percentage of inliers in the respect of the total number of points.

2.5 Region growing

According to the threshold analysis, described in section 2.2 of this chapter, the voxel structure is partitioned in planar voxels and curved voxels that can be further recognised as cylindrical voxels or not. From this distinction, the global recognition of the component's planes or cylindrical surfaces may derive by means of a region-growing algorithm

that is able to aggregate together contiguous voxels that have similar geometric descriptors (normal direction and distance from the origin, in the case of planes; axis and radius, in case of cylinders). Region growing algorithms define clusters starting from “seeds” able to describe a feature. They aggregate elements into a region according to an imposed threshold (Lee, et al., 2003). Here, a hybrid region growing – hierarchical clustering procedure has been set up to find groups of voxels, V_{ijk} which respect a condition of adjacency, encompassing also local surfaces of equal geometric descriptors

In the case of planar voxels, the unit vectors associated to the normals of the best-fit planes inside the voxels, $(n_x \ n_y \ n_z)_{ijk}$, are verified to specific unit directions, $(a \ b \ c)$, for example the reference axes, by means of a threshold condition derived from the so-called L_2 orientation norm (Shamir, 2008):

$$L_2 = 1 - (n_x \ n_y \ n_z)_{ijk} \cdot (a \ b \ c)^T \leq \varepsilon \quad (3.7)$$

This threshold, from now on called ‘normal dot product threshold’, is verified for each pair of the voxel’s adjacency matrix, generated in order to consider physical connections between voxels. Then, this matrix is updated with a code about the effective plane direction of each pair. Through this new adjacency matrix, plane partition is then completed via hierarchical clustering starting from a seed value defined according to the specific directions analysed with eqn. (3.5). The specific direction, $(a \ b \ c)$, is taken from a set of unit normals, S , that is defined by means of an iterative procedure inserted inside the clustering phase, according to this reasoning. Since eq. (3.5) is checked recursively on each i, j, k when it is found always “false”, a new direction

$(a \ b \ c)_{\text{new in } S} = (n_x \ n_y \ n_z)_{ijk}$ is added to S if:

$$\begin{cases} 1 - (n_x \ n_y \ n_z)_{ijk} \cdot (a \ b \ c)_0^T > \varepsilon \\ \forall (a \ b \ c)_0 \in S \end{cases} \quad (3.8)$$

Doing so, at the end of this region growing – hierarchical clustering procedure, a plane clustering is done according to every significant directions of the acquired component that are found in S .

In the case of cylindrical voxels (or other curved surfaces that may be fit), the clusterization is made according to seeds found from other suitable descriptors. For example, in the case of cylinders we have adopted the radius, R , considering that the aggregation by means of the axes is taken into account also by the voxel connection. The adopted formula is:

$$DR_{ij} = 1 - \frac{abs(R_i - R_j)}{R_j} < \varepsilon; \quad \forall R_j \in S; \quad (3.9)$$

where ε_i stands for the threshold assigned to accept R_i as member of the cluster whose R_j is the seed. If eq. (3.7) is not verified for all the j^{th} elements inside the set of seeds (S), R_i becomes a new member of S . Doing so at the end of the region growing – hierarchical clustering procedure, cylinder clustering is done according to every significant radius R_j of the acquired component that are found in S .

To conclude the description of the proposed clusterization some examples are given in Figure 31, to help a clear understand of the expected output given by this part of the computation. On the right, it shows the clusterization according to three specific plane direction found in the component, as distinguished by different colours. On the left, the subdivision between planar and curved voxels is depicted in different colours (green points of planar voxels, blue in the other case).

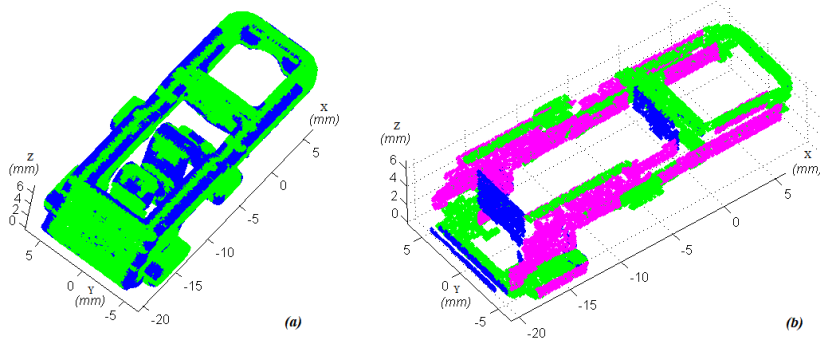


Figure 31. (a) Voxel detection with small radii or non-planar region (blue points); (b) Clusters found for planes perpendicular to the reference axes – (blue for x axis; magenta for y axis; green for z axis).

3. Workflows of implemented strategies

Result of clusterization is the global surface recognition, since for each cluster, through the position of the aggregated voxels, represented by their indices, single global surfaces are distinguished. Figure 32 summarizes the process according to the adoption of LM(Kasa) as cylinder fitting algorithm, as also preliminarily presented in (Bici, et al., 2014b). It summarises the proposed approach and their related methodologies, described in the previous sections through the same colours.

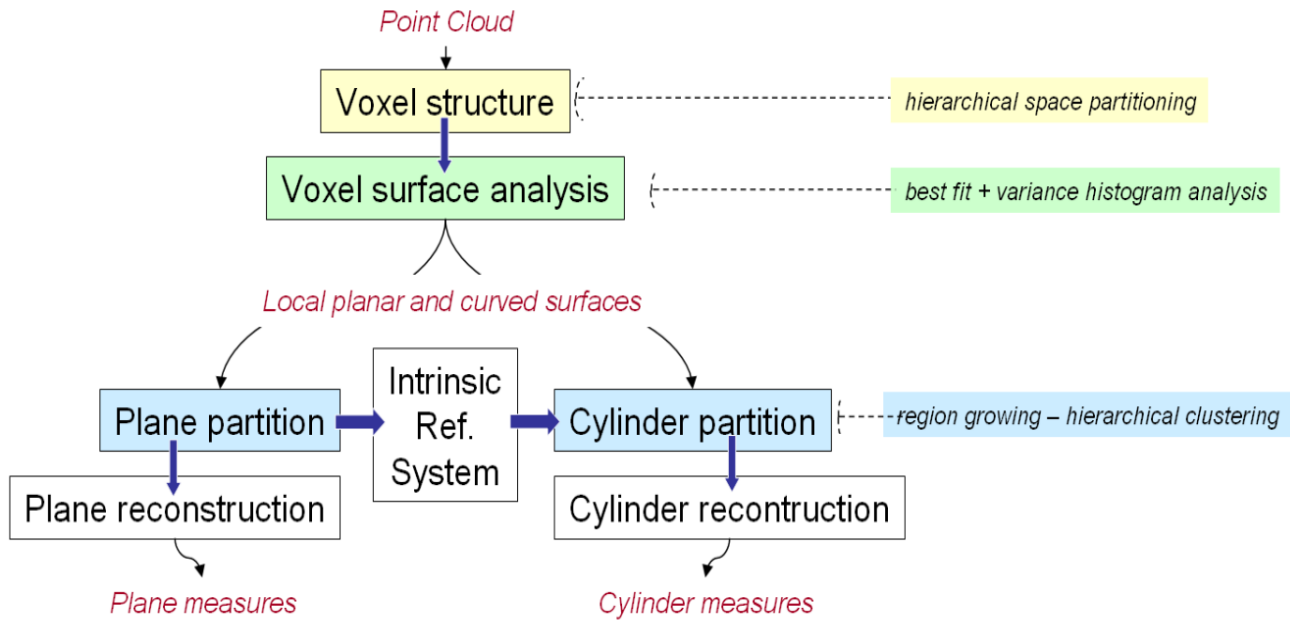


Figure 32. Logical workflow of the proposed approach and applied methodologies (on the right) using LM(Kasa) algorithm.

As already mentioned in section 2.3 of this Chapter, the LM(Kasa) asks for a preliminary definition of the direction of cylinder axes, while Ransac-based algorithms may ask for it only in critical cases, when the first guess set of points, fail to estimate the parameters. Assuming it may works in the most frequent cases, the procedure of Figure 32 becomes that of Figure 33, where no link is necessary between plane and cylindrical reconstruction.

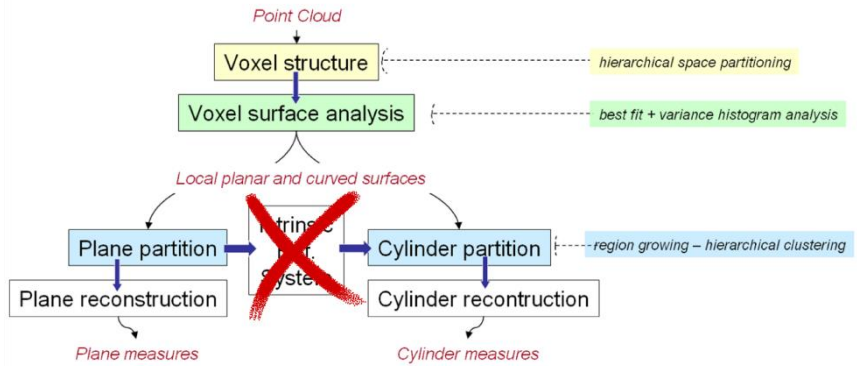


Figure 33. Logical workflow of the proposed approach and applied methodologies (on the right) using Ransac-based algorithm

So, to apply LM(Kasa) algorithm at least 3 reference directions must be found.

The segmentation procedure recognizes the planar faces of the components notwithstanding the orientation of the point cloud during the acquisition. It can be misaligned with effective principal directions of the component or with the axes system of the CAD model. From the point of view of the tolerance measurement, an appropriate alignment could be necessary to localize datum or specific sets of functional planes according to draft annotations. It becomes of utmost interest in case of automatic inspection. Often, it is made by fixtures during the acquisitions or can be derived by knowing the reference axes associated to the path planning of the acquisitions and multiple views, as described in Chapter2.

Starting from the voxel structure of the component the knowledge an Intrinsic Reference System (IRS) may be found, looking for the plane directions associated to the most populated sets of voxels. In case of electromechanical components, it may be considered a consistent reasoning since they are characterised by functional features on orthogonal planes or cylinders whose axes are parallel to the three principal directions of the component. Thus, it is clear that the most populated sets of voxels are the ones, which contain planar surfaces oriented along component's principal directions. From this, the IRS computation derives by assigning as first reference axis the planar direction of the most populated set of voxels. Then the other two axes are found between the two subsequent more populated sets of voxels that are mutually orthogonal. The soundness of this procedure has been tested on different components as reported in (Bici, et al., 2014b).

3.1 Overview of the implementation

From this workflow, the implementation scheme of the procedure can be described. It is being developed in MatlabR2012 and in the 2017 version. The “Voxel structure” step has been implemented using the parallel computation; region growing and hierarchical clustering have been approached via sparse matrices. Since the logical approach for Plane and Cylinder partition is based on the same methodologies, the adoption of distributed computation is investigating to perform hierarchical clustering of planes and cylinders at the same time, after the region growing of the planar voxels.

3.2 Usage of Parallel Computing

During the development of the whole procedure, one of the most evident issues, as every programmer knows well, is the computing time, or better its minimisation. By this point of view, some efforts have been spent to analyse what were the time bottlenecks in terms of algorithms and program functions. One of the most time expensive phases turned out to be the voxel structure creation. Its time lapse in several cases, can reach portions about the half of the total time spent for the entire calculation

needed in recognition phase, obviously, depending on the selected resolution.

Through MATLAB Parallel Computing⁸, it has been possible to divide the efforts into all the processors, or cores, available, trying to not bring large modification of the entire procedure, just adapting the developed serial functions, in order to have a direct comparison in terms of time saving.

For the considered part of routine, initially, the idea was a direct parallelisation of the calculation, but it was not a real possibility, because only independent operations can be directly parallelised. Instead, in our case, the iterative divisions, passing from one level of resolution to the successive, make operations dependent. So that, without the possibility of actions of direct parallelisation and avoiding the eventuality of a redesign of the entire algorithm, the only way to reach a parallelisation was to work on inputs. The solution of this issue has been the co-distribution of inputs for the execution, making each processor working onto a portion of the entire cloud, creating different portions of the voxel structure.

In brief, choosing a direction of the voxel structure, the developed algorithm divides the cloud along this direction, making a number of “slices” equal to the number n of working processors,. These slices are submitted as parallel jobs. The total size of the partial voxel structure per job, is then:

$\frac{L \times M \times N}{n}$; in which L, M, N are respectively the number of voxels for each direction and n is the number of working processors or cores.

Then, the algorithm can work as the original, taking care of the “reassembly” of data. An example of the division on a Dual core (2

⁸ *Parallel Computing is a type of computation in which many calculations, or the execution of processes, are carried out simultaneously. Large problems can often be divided into smaller ones, which can then be solved at the same time* (Almasi & Gottlieb, 1989).

processors), with the assigned slices of cloud and the derived voxel structure is reported in Figure 34.

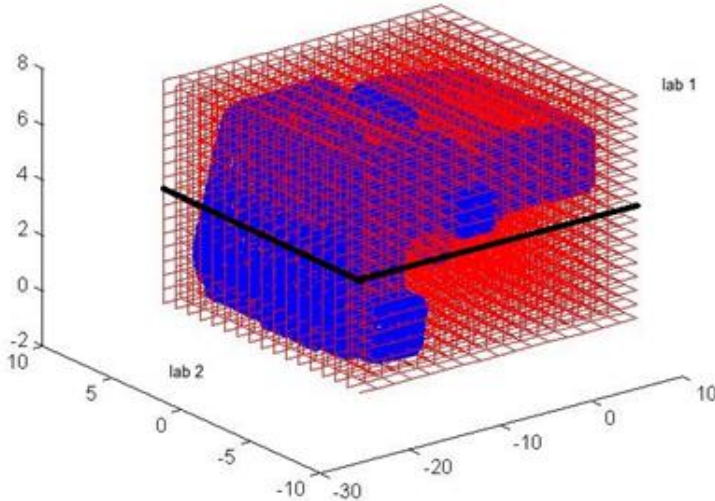


Figure 34. Voxel structure obtained after the parallelisation in two processors; the upper part has been assigned to the first worker, the bottom to the other.

The usage of parallelisation has made possible to reach high time savings, in particular for voxel structure with a high number of voxels in each direction. Results of tests on Din Rail Clip are reported in Table 3, using the same Quad core pc, in single, dual and quad core modality.

	Single core	Dual core	Quad core
16x16x16	23 s	23 s (-0%)	28 s (+ 21%)
32x32x32	128 s	109 s (- 15%)	51 s (- 60%)
64x64x64	1209 s	840 s (- 31%)	260 s (- 78%)

Table 3. Time savings with parallelisation for the generation of the voxel structure.

It is easy to see that savings increase with the number of voxels, arriving at more than the 70% in the quad core case with structures of 64 x 64 x 64. On the contrary, this procedure is inconvenient for low number of voxels, as in case of structure 16 x 16 x 16.

4. Discussion

This Chapter has been aimed to explain objectives and methods applied in the implementations. In each section, theory and related problems have been introduced without a deep discussion of the assessment and the improvement of accuracy and other specific implementation problems specifically linked to the final goal of tolerance inspection. This part is presented in the next Chapter, so it seems useful here a summary of the open issues to efficiently set-up the proposed strategies.

Concerning the voxel structure definition the most critical aspect is the selection of the number of final subdivisions. It means the selection of suitable k_L , k_M , k_N , to achieve the proper resolution to distinguish the surfaces that are interesting for the measures.

Threshold analysis to define the first bin related to planar voxels is conveniently improved by the iterative evaluation of variance threshold. Nevertheless, some problems may arise due to an underestimated number of bins taken as the first guess for the iterative threshold. Consequently, the first bin, also at the end of the iteration may not represent only planar voxels, but also cylindrical. This can happen when the most populated bin is not the first one, as it will explain in the case of axial symmetrical parts with large radius.

Concerning surface recognition major research topics are: (a) cylinder of curved surface local fitting and (b) threshold to define seeds for the region growing - hierarchical clustering algorithm. In the first case the two strategies, described in section 3, derive with specific pros and cons in terms of computational time and accuracy of the surface recognition and of the measure. In particular further investigations are required about

the reliability of the computation of Intrinsic Reference System, for the first strategy, and about the fitting exception of the Ransac-based algorithm, (namely the cases where an initial axis orientation must be supplied), for the second one.

Chapter 4 – Set-up and evaluation of the algorithms

1. *Materials and methods*

The implementation of the algorithms and their evaluation has been made through test cases and sensitivity analysis. These test-cases have been taken from different fields, not only from the injection moulding production of electromechanical parts, since they have to present requirements suitable to stress the algorithms by sensitivity analysis. We can highlight the following test cases:

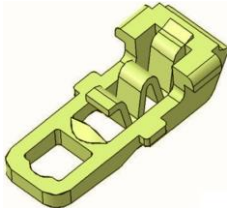

<p><u>Din Rail Clip</u> for setting-up the algorithm of the voxel structure and of plane recognition</p> <p><i>No. of points = 60,607</i></p>	
<p><u>Flange for Aeronautical Applications</u> for validating voxel structure and plane surface recognition and for setting up cylindrical surface recognition</p> <p><i>No. of points = 479,780</i></p>	

Table 4. Test cases used for procedure development.

The Din Rail Clip is made in Polyoxymethylene (POM), also known as Acetal (see Annex 1), a plastic material with an excellent fatigue resistance in relation to its low cost. Nominal maximum size dimensions are 30.5 x 13.8 x 7.4 mm and, despite the colour in CAD model of the figure, in the actual practice, due to European legislation, its default colour is black. Fortunately, this reduces the risk of reflection during laser

scanning, giving point cloud of high quality. More than one sample has been acquired obtaining, after multiple view alignment, point clouds of more than 60×10^3 points. The principal part of the clip is the spring placed in its internal part, and it is the cause of the material choice. It works in mechanical coupling with the breaker base and it has to have a high level of elasticity in order to guarantee the sliding but, at the same time, it has to be sufficiently rigid, ensuring the locking. From the industrial point of view, since this component is inserted in an assembly, many dimensional tolerances are of interest, thus, considering that no particular thin walls are present, it has been used to preliminary test voxel structure definition and planar surface recognition (in section 2 and 3).

The Flange for Aeronautical Applications is not an injection moulded part, but it has been selected to stress the algorithms in the respect of larger shapes and curvatures, ($\Phi 208 \times 30$ mm), with details in a wide range of lengths. It is a component of a Boeing product, obtained through a β -forging process starting from Ti6Al4V Titanium Alloy powders, that is being studied by Centro Sviluppo Materiali (CSM). This powder material is suited for manufacturing near net shape forged components since it has been demonstrated that it is possible to manufacture by powder-metallurgy samples that are mechanically equivalent to those from commercial extruded bar (Testani & Tului, 2012), (Testani, et al., 2013). Tolerance qualification from of this process is of outmost interest and demonstrating the feasibility of an automatic procedure can be a preliminary step of the experimental plan necessary to reach this goal. To avoid reflections, the surface has been white-mat painted. Characteristic lengths are $208 \times 208 \times 30$ mm, after multiple view alignment, point clouds of 479,780 points is obtained.

2. Voxel structure and local surface recognition

2.1 Din Rail Clip

The first input parameter of the proposed approach is the number of voxels, which divides the point cloud. If voxel discretisation becomes coarse, a low resolution is obtained and many details are lost, so that the

effective planes of the component are not recognised. On the contrary, small voxel length may reduce the number of points inside the voxel, reducing benefits in terms of precision and computational efforts. Table 5 shows, for the Din Rail Clip, a quantitative evaluation of the voxel structures associated to different zoom ratios (r, s, t) according to the equations 3.1, 3.2, 3.3 of Chapter 3.

	Constant zoom ratio ($r=s=t$)		Multiple zoom ratios ($2^r, 2^s, 2^t$)	
	$k_x \times k_y \times k_z$			
<i>No. of $V_{ijk} = 1$</i>	16x16x16 (=35%)	32x32x32 (=18%)	32x16x8 (=35%)	64x32x16 (=16%)
<i>V_{ijk} length (mm)</i>	1.9x0.9x0.5	1.0x0.4x0.25	1.0x0.9x1.0	0.5x0.4x0.5
<i>V_{ijk} with less than 3 points</i>	24	734	21	358
<i>Average No. of points per V_{ijk}</i>	43	10	44	11

Table 5. Din Rail Clip: Voxel structure characteristics in function of the zoom ratios (r, s, t).

Figure 35 shows the frequency of voxels (in percentage) in relation with the number of point per voxels.

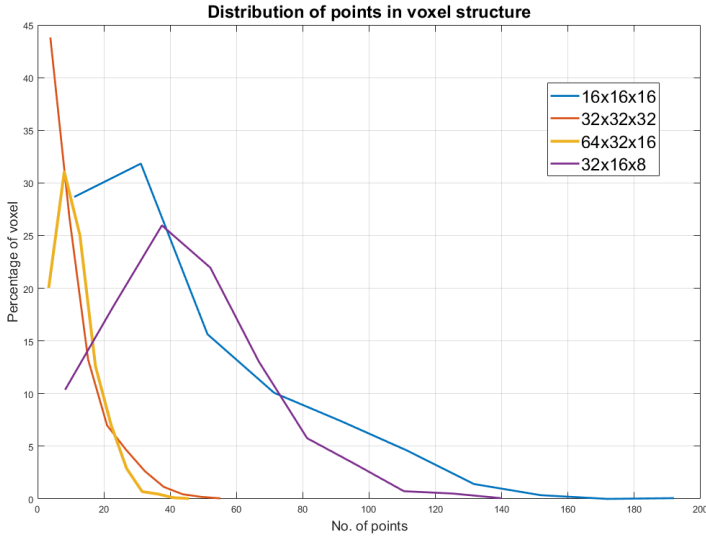


Figure 35. Din Rail Clip: Frequency of voxels (in %) with a specific No. of points.

Voxel structures of 16x16x16 and 32x16x8 have similar characteristics in terms of:

- number of $V_{ijk} = 1$, that is about 35% of the whole possible voxels;
- average number of points per voxels, about 40 points;
- number of not significant V_{ijk} , with less than 3 points, (20 voxels to be discarded).

Similar results are obtained for the two remaining voxel structures, with a reduced number of full voxels (18%) and number of points, naturally depending by the higher number of elements of subdivision. It is confirmed by Figure 36 that shows, in the case of 16x16x16 and 32x16x8 voxel structures, a rather uniform distribution of points per voxel. Uniformity may be seen as a rational distribution of the computational resource and of the surface information per voxel (40 points against 10 points as average numbers per voxel, and 35% of $V_{ijk} = 1$ against about 15% in the case of 32x32x32 or 64x32x16).

The predominance of multiple zoom ratios in the respect of the constant one, assuming equal performances of significant V_{ijk} is shown during the segmentation process. Figure 36(a) shows the cloud of points segmented in planar and curved voxels starting from the 16x16x16 voxel structure. The arrows highlight critical areas where the local planar surface recognition fails due to a wrong voxel subdivision, Figure 36(b).

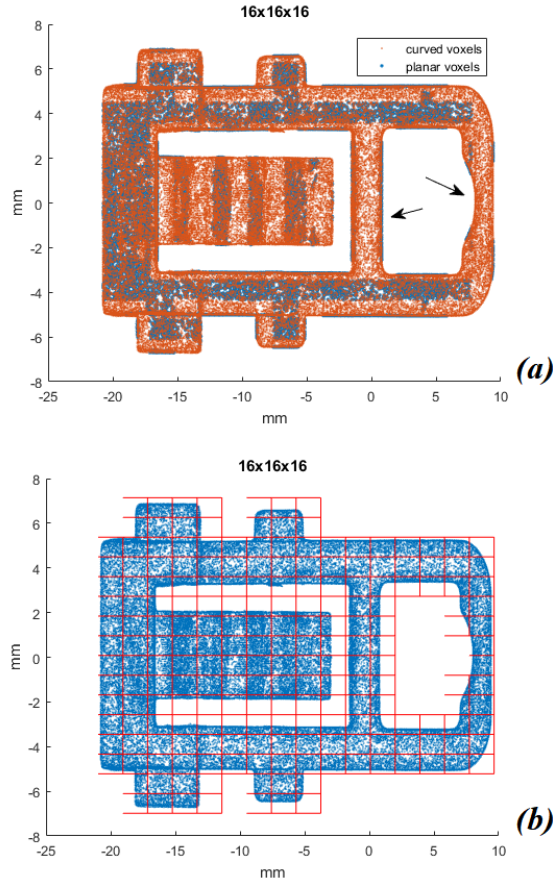


Figure 36. Din Rail Clip: 16x16x16 (a) Local surface segmentation (blue points are planar, mustard are curved); (b) Voxel Structure.

Figure 37 represents the same views assuming a 32x16x8 voxel structure. In this case, the enhanced resolution along the axis with 32 voxels allows detecting planar surfaces also nearby the arrows of Figure 36(a).

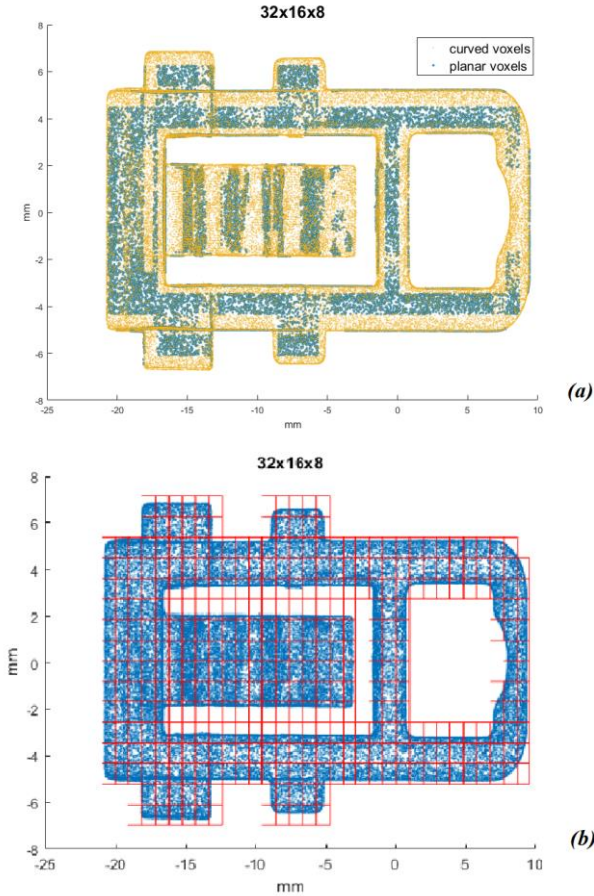


Figure 37. Din Rail Clip: 32x16x8 (a) Local surface segmentation (blue points are planar, mustard are curved); (b) Voxel Structure.

Concerning the segmentation process, the effect of the voxel structures can be seen in terms of surface recognition, which means number of planar directions found significant according to section 2.5 of Chapter 3. Table 6 quantifies this result.

Voxel structures with high numbers of $V_{ijk} = 1$ (namely 16x16x16 and 32x16x8) has a minor number of recognised directions, extremely consistent among them. The other cases (32x32x32 and 64x32x16) has more directions and many of them are defined by a very small % of voxels (less than 1%), as described in Table 7 for the case of 32x32x32.

	Constant zoom ratio ($r=s=t$)		Multiple zoom ratios ($2^r, 2^s, 2^t$)	
	$k_x \times k_y \times k_z$	16x16x16	32x32x32	32x16x8
<i>Directions found</i>	12	29	11	32
<i>Final clusters</i>	10	17	8	22

Table 6. Din Rail Clip: number of planar directions after segmentation in function of the zoom ratios (r, s, t).

nx	ny	nz	% of voxels
0.0007	1.0000	0.0017	28.7
0.9994	-0.0024	-0.0339	15.7
0.0085	-0.0028	1.0000	13.6
0.9755	-0.0024	-0.2198	12.8
0.8161	-0.0014	-0.5780	11.1
0.9437	-0.0034	0.3309	9.4
-0.4293	-0.0037	0.9032	2.0
0.7745	0.0051	0.6326	1.4
0.4831	-0.0038	0.8756	1.4
-0.2538	0.0472	0.9661	1.0
0.9934	-0.0058	0.1146	0.7
-0.6205	0.0054	0.7842	0.7
0.9505	0.3102	-0.0162	0.6
0.9578	-0.2817	-0.0578	0.5
0.7706	-0.6373	-0.0004	0.2
0.7576	0.6526	0.0139	0.2
0.0239	-0.3148	0.9489	0.2

Table 7. Din Rail Clip: Final directions recognised via hierarchical clustering and region-growing algorithms ($L_2=0.01$)

Figure 38 shows a graphical comparison among the directions changing from 16x16x16 to 32x32x32. Directions with similar cosines

are always that ones with highest % of voxels (Figure 38(b)). In our opinion, this may confirm the consistency of the hierarchical clustering and region-growing algorithms, highlighting also the major disadvantage of voxel structures with few points per voxels.

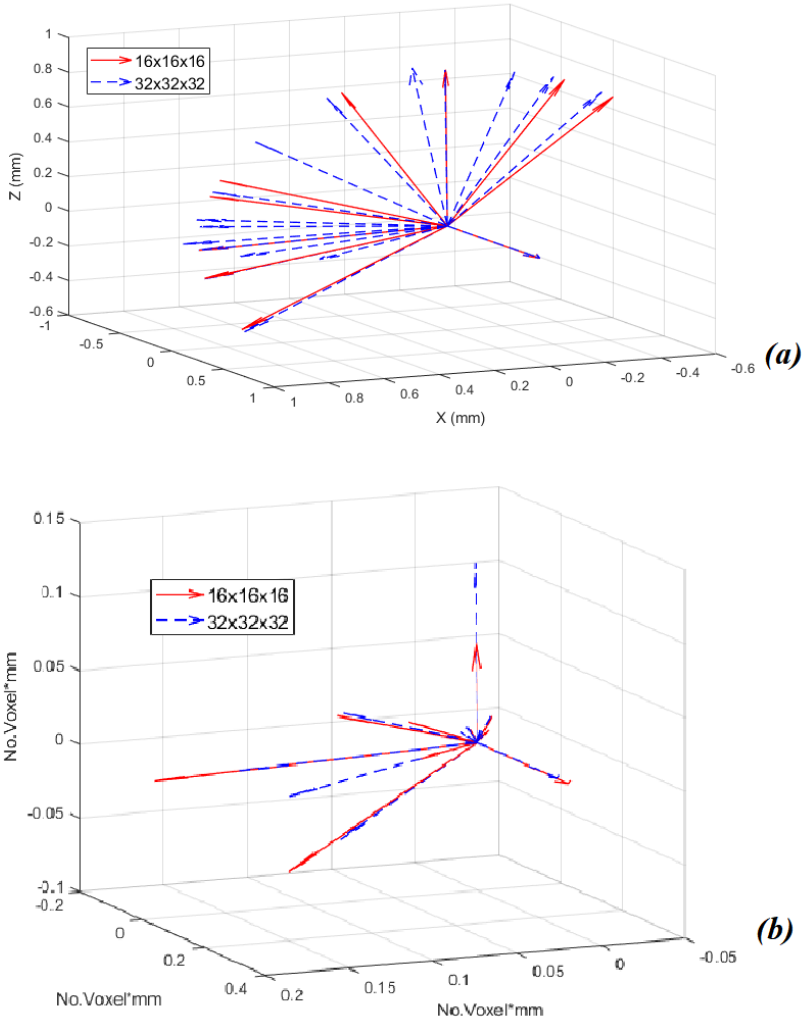


Figure 38. Din Rail Clip: comparison among 16x16x16 and 32x32x32 - (a) cosines of the recognised directions; (b) cosines weighted with % of correspondent voxels.

In fact, more dense of voxels, like $32 \times 32 \times 32$ or $64 \times 32 \times 16$, with a lower number of points per voxels may reduce the accuracy of segmentation since local curved surfaces may be erroneously approximated as plane (Figure 39).

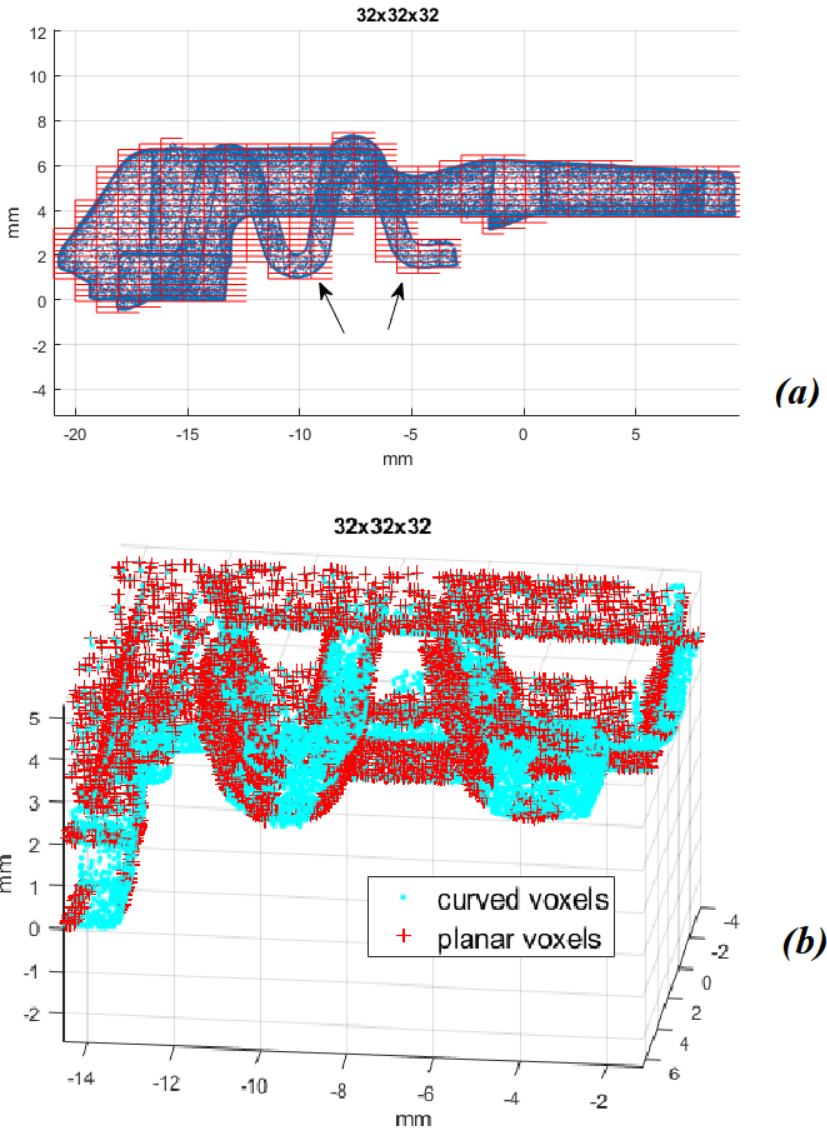


Figure 39. Din Rail Clip: $32 \times 32 \times 32$ (a) Voxel Structure; (b) Detail of the local surface segmentation (red marks are planar, cyan are curved).

The reduction of points inside the voxels increases the risk of erroneous partition of curved surfaces in planar. Figure 40 concludes this analysis, showing the final clusters associated to each direction (one per type of marker) related to the 32x16x8 voxel structure.

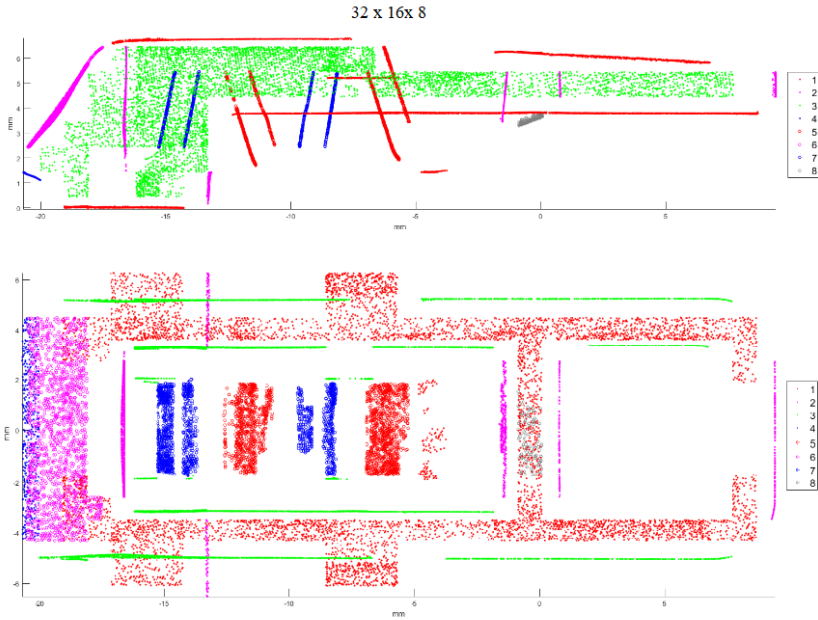


Figure 40. Din Rail Clip: 32x16x8 final clusters.

2.2 Flange for Aeronautical Applications

The complexity of this part (wide range of lengths of its features, from 230 to 10 mm) and its large curvature, represent a relevant case to stress the procedure. For the sake of clarity, elaborations and figures are here referred to a 90° sector of the clouds, remembering that for transferring the results to the whole shape, voxel data in terms of k_L , k_M , k_N must be assumed to be double. Table 8 shows the results related to different voxel structures.

	Constant zoom ratio ($r=s=t$)	Multiple zoom ratios ($2^r, 2^s, 2^t$)		
$k_x \times k_y \times k_z$	16x16x16	32x32x8	32x32x16	64x64x16
<i>No. of $V_{ijk} = 1$</i>	984 (24%)	2091 (=26%)	2884 (=18%)	8374 (13%)
<i>V_{ijk} length (mm)</i>	6.5x.6x1.9	3.2x3.2x3.7	3.2x3.2x1.9	1.6*16*1.8
<i>V_{ijk} with less than 3 points</i>	10	31	99	1206
<i>Average No. of points per V_{ijk}</i>	125	59	43	15

Table 8. Flange for Aeronautical Application: Voxel structure characteristics in function of the zoom ratios (r, s, t); data are referred to a 90° section of the whole cloud.

The axial-symmetry of the part determines that planar voxels should be always related to z-direction that has the minor length. For this reason, not uniform V_{ijk} lengths have been investigated with voxel structures of resolution: 16x6x16 and 32x32x16. In the other two cases, a rather cubic subdivision is achieved. Figures from 41 to 44 shows the associated voxel structures. As highlighted by the arrows, difficulties will occur to capture the planar surface in the upper part of the flange. It is due to the presence of no more than two voxels superimposed on that planar surface. During the segmentation, they will be left apart from the planar voxel set, since they contain both the upper surface and the lateral one. Only 64x64x16 is suitable to partially capture that plane, with at least 3 voxels along the radius of the flange.

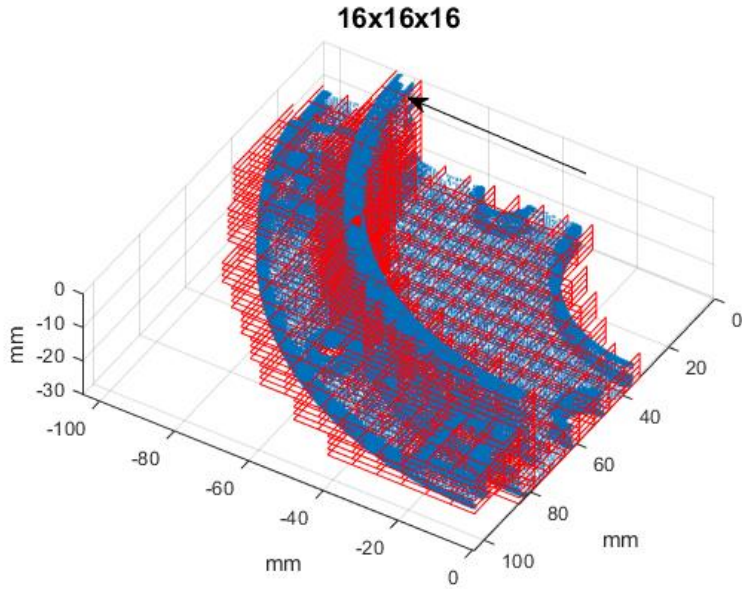


Figure 41. Flange for Aeronautical Application: Voxel structure with 16x16x16 resolution.

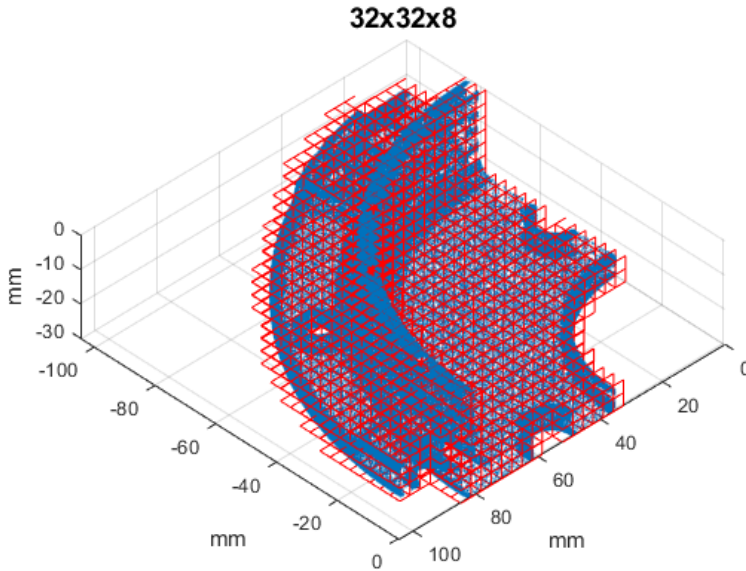


Figure 42. Flange for Aeronautical Application: Voxel structure with 32x32x8 resolution.

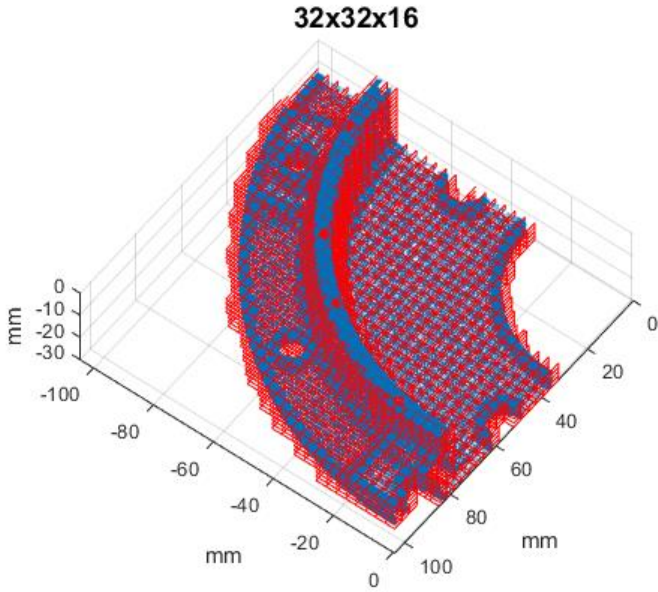


Figure 43. Flange for Aeronautical Application: Voxel structure with 32x32x16 resolution.

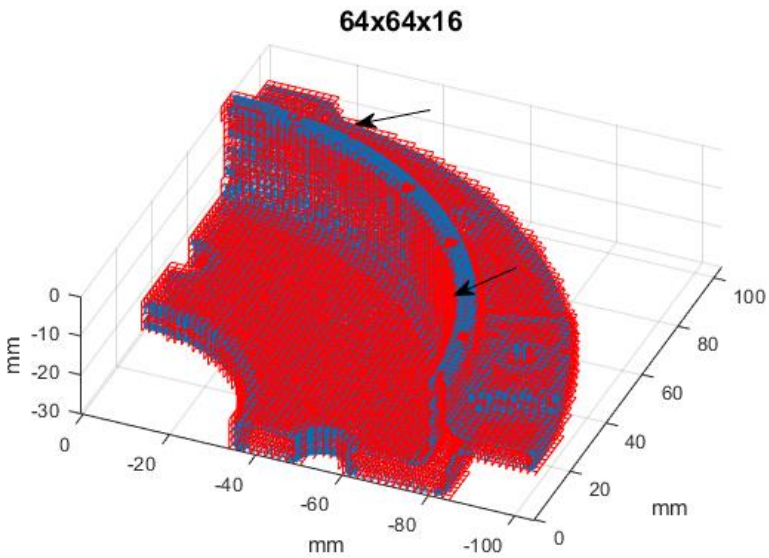


Figure 44. Flange for Aeronautical Application: Voxel structure with 64x64x16 resolution.

Figure 45 shows the occurrence of points per voxels changing the voxel structures. 64x64x16 confirms its capability of a more uniform number of points per voxels, but unfortunately increasing the resolutions the percentage of $V_{ijk}=1$ does not increase relevantly.

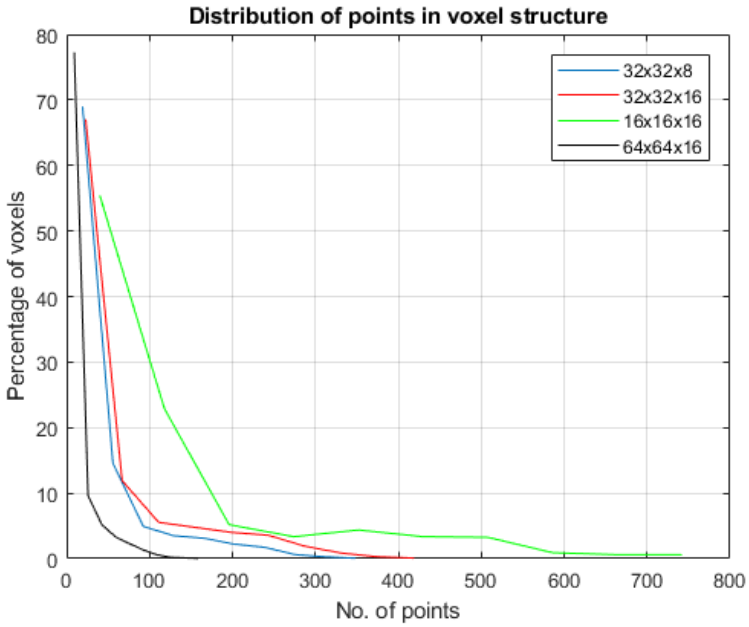


Figure 45. Flange for Aeronautical Application: Frequency of voxels (in %) with a specific No. of points.

Concerning the planar and curved voxel subdivision, every voxel structure, except the 16x16x16, can recognise the small holes as curved voxels, although in larger diameters, accuracy problems are present, as shown for example in Figure 46 (red points are in planar voxels, grey in curved ones, arrows in blue highlight the problem). This figure is related to the voxel structure 32x32x16, the other structures have similar problems, with slight difference in percentage of involved voxels.

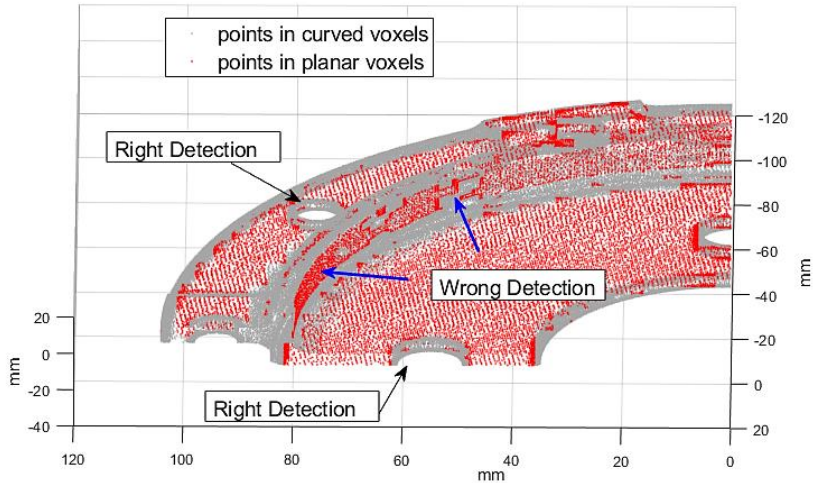


Figure 46. Flange for Aeronautical Application - voxel structure 32x32x16. Points in planar (red) and curved (grey) voxels

In this case, an improvement can be obtained by changing the first guess for the number of bins of the iterative threshold that is applied to the variance, for distinguishing planar and curved voxels. Figure 47 shows these voxel's values taken in a transversal section of the flange (every single cell of the colour map represents a voxel). It aims to demonstrate that standard deviations of points, from the local best fitting plane, in case of cylindrical surfaces, are at the upper value of the range in the respect of the effective local planes, which is at the lower. Thus if the variance threshold found iteratively starts from a number of bins that includes in the first one both cylinders and planes, on the average they will be confused.

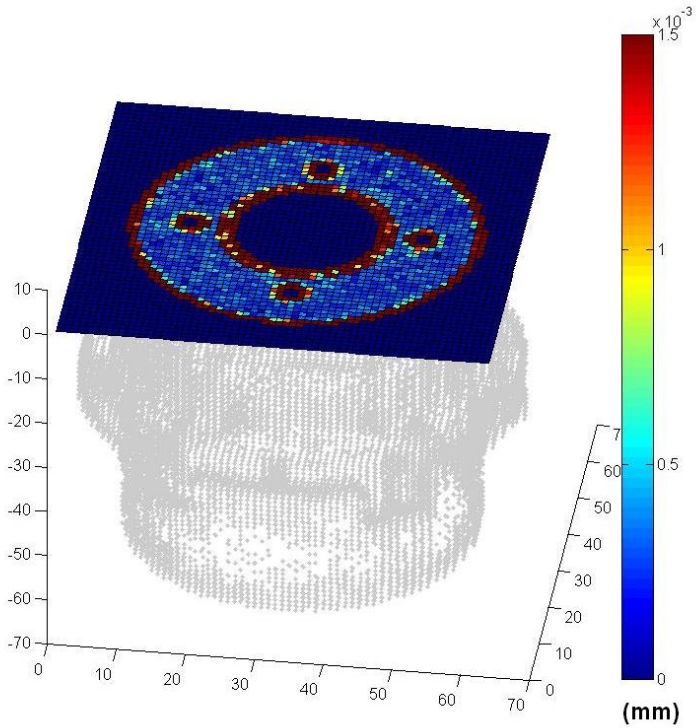


Figure 47. Voxel standard deviation in a transversal section of the acquisition.

Figure 48 shows this aspect, increasing the number of bins of one order of magnitude. Clusters near the bottom of the component are not present increasing the number of bins.

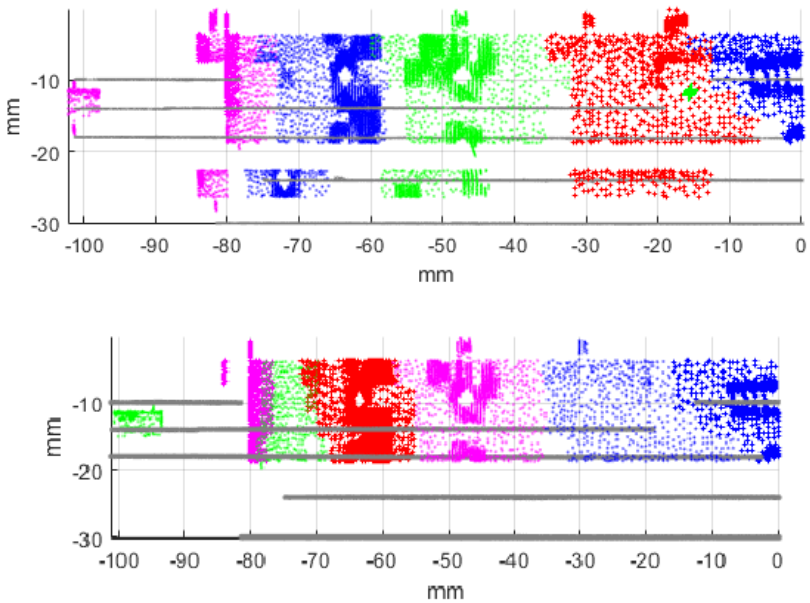


Figure 48. Flange for Aeronautical Application - voxel structure 32x32x16. Final clusters aggregated from the planar direction found, according to the change of the increasing number of first bin for threshold analysis

Concerning the application of region growing – hierarchical clustering, the comparison according to different voxels structure in this case gives equal results. Recognised directions are that associated to the different colours of Figure 48.

3. *Threshold for surface recognition*

Surface recognition accuracy is related to the:

- Fitting model variance for assessing the local surface feature (plane or cylindrical);
- L_2 orientation norm for region growing - hierarchical clustering (see section 2.5 of Chapter 3, in particular, equation 3.7).

The effects of the first one have been discussed in the previous section, highlighting that:

- coarse voxel structures may exclude planar voxels since they may include points of different surfaces;
- voxels with cylindrical surfaces with large radii may be erroneously interpreted as planar if the first guess for the histogram of the variance, used in the threshold analysis, is not well defined.

The $L2$ orientation norm is applied during the clustering procedure to evaluate if: (a) the local best fitting plane associated to a generic V_{ijk} is parallel to the neighbouring ones; (b) it is oriented as the set of directions $(a\ b\ c)$ relevant for describing the component faces. It works on the dot product of the directional cosines of the plane fitting in two connected voxels.

For the Din Rail Clip, Figure 49 shows the variation of the number of clusters that has been obtained changing threshold values in the range $[0.001, 0.50]$, to search planes perpendicular to the three axes of the reference system (O, x, y, z) .

Figure 49(a) is related to all the computed clusters for each reference direction. Figure 49(b) considers only clusters with more than 4 voxels inside. Comparing these graphs it emerges that the cluster variations are quite similar changing the threshold value and that some clusters made of less than 4 voxels are always present along each directions. Decreasing the threshold, obviously, also sloping planes are evaluated coherent with the reference axis, so the number of clusters increases with the angle allowed through the dot product threshold.

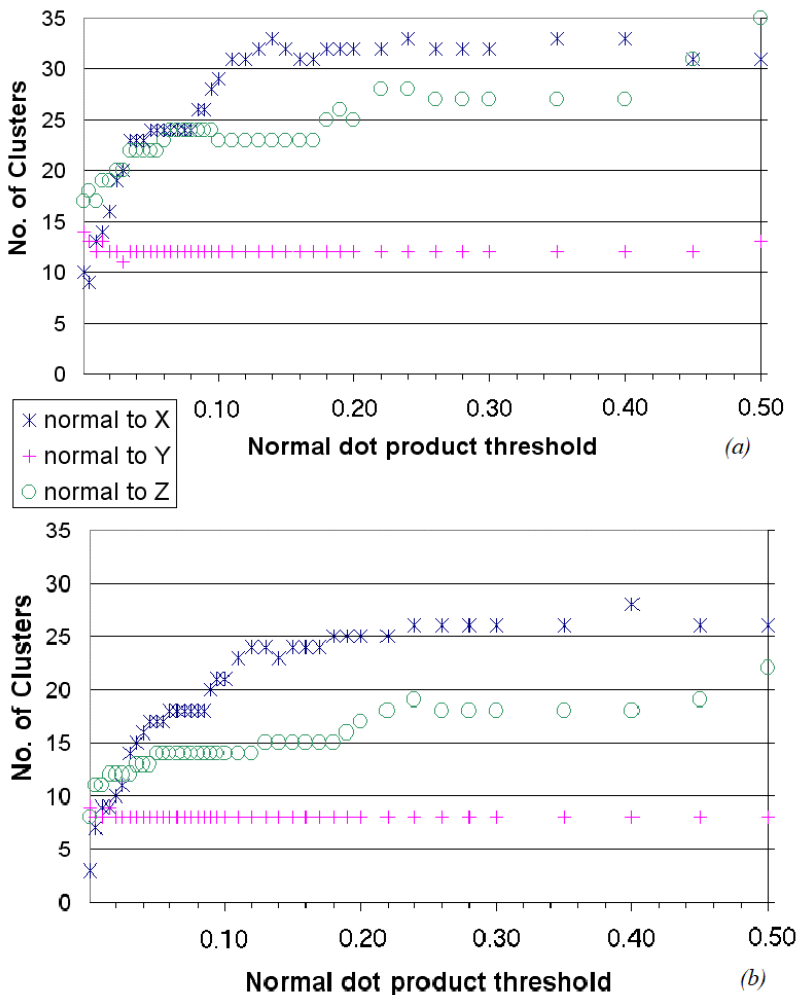


Figure 49. Din Rail Clip: Voxel Structure 32x32x32 - Sensitivity analysis on the normal dot product threshold: (a) no. of clusters normal to reference axis; (b) no. of clusters normal to reference axis, excluding clusters made of less than 4 voxels

In the case of the Flange for aeronautical application, the L_2 orientation norm can be useful to improve the accuracy of the large radius detection. In fact, decreasing its value may reduce the number of adjacent voxels around the circle that are clustered together, leaving only narrow bands of clusters along the axis (Figure 50). Unfortunately, if the voxel structure is not dense enough, increasing L_2 norm obviously may increase

the risk of reducing plane recognition in small regions, as it happens in the upper part of the flange (Figure 51).

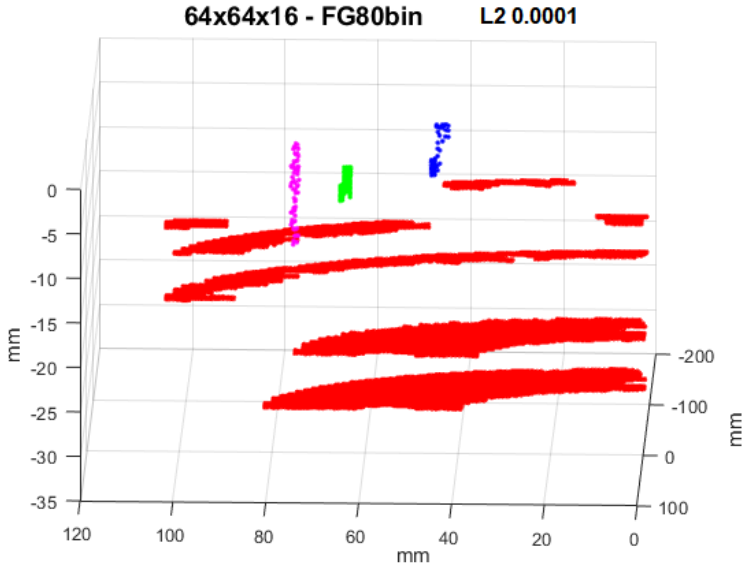


Figure 50. Plane recognition with $L_2=0.0001$ for Flange.

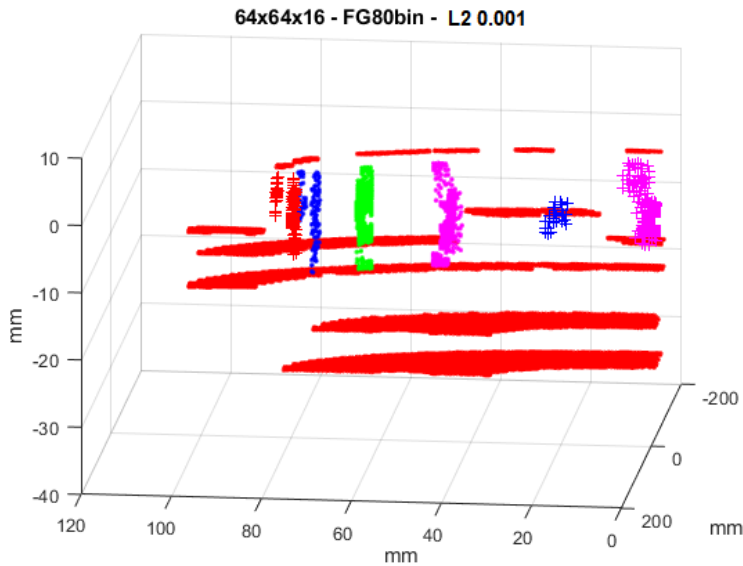


Figure 51. Plane recognition with $L_2=0.001$ for Flange.

3.1 Threshold transferability

An interesting issue concerns with transferability of the thresholds from one case to another. In our opinion, it should be said “from a category of components” to another. In particular, this is true for components, axial symmetrical or not, with at least one length one order greater than the others. In fact, applying the same flange optimal thresholds (first-guess number of bin=100 and $L_2=0.0001$) to the din rail clip will be more stringent, as shown in Figure 52(b) in comparison with Figure 52(a), that shows the clustered directions for the optimal voxel structure in its own optimal thresholds (see section 1.1). Figure 52(c) shows the results moving only the first-guess number of bins, showing a general similar behaviour to Figure 52(a).

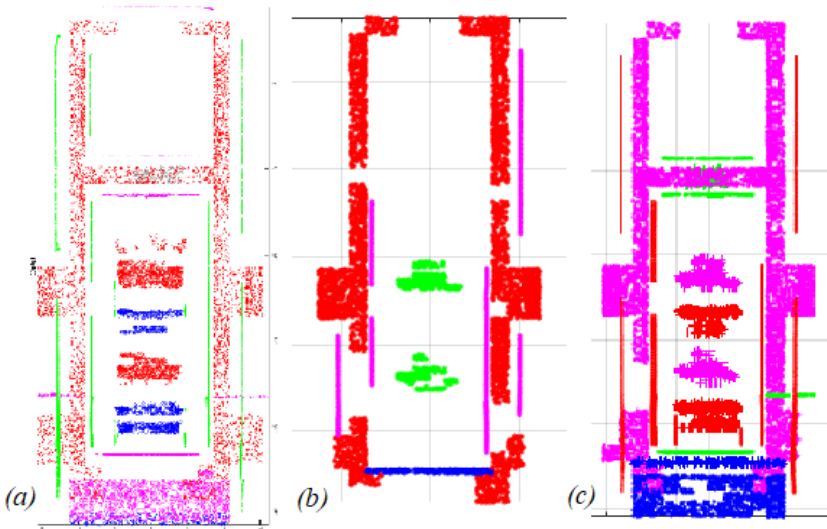


Figure 52. Transferability of the thresholds: (a) first-guess no. bin = 20, $L_2 = 0.0001$; (b) first guess no. bin = 100, $L_2 = 0.0001$; (c) first guess no. bin = 100, $L_2 = 0.0001$

In terms of final directions, assuming L_2 equal to the one chosen for the flange produces a reduction of clusters from 8 to 4. The reason of this behaviour can be due to a more scatter data on that faces, thus more acquisition noise or less points, which is possible considering that those faces are in the inner part of component (Figure 52(c)).

4. Fitting for cylinders and curved surfaces

4.1 Intrinsic Reference System and LM(Kasa) algorithm

For tolerance inspection, geometrical descriptors of the surfaces are of the utmost importance. Through the variance threshold analysis, voxels with local curved surfaces are recognized, so that cylindrical fitting may be used to find them. As discussed in the previous chapter, two approaches are investigated to fit cylinders. One is based on the computation of the circular sections through Levenberg-Marquardt minimization using Kasa algorithm as first-guess, LM(Kasa). The second applies the MLESAC formulation.

LM(Kasa) asks for a preliminary knowledge of the axes directions, MLESAC does not, with some exceptions due to the fitting data quality. For LM(Kasa), a component Intrinsic Reference System (IRS) is defined, through a specific elaboration of the most populated planar clusters that are derived from the voxel structure.

From the test case point of view, the IRS has been always found, in case of the Din Rail Clip, it is oriented as the xyz of the cloud; in case of the Flange for Aeronautical Application, it has the x-axis coincident with the central axis of the component (Figures 53 and 54).

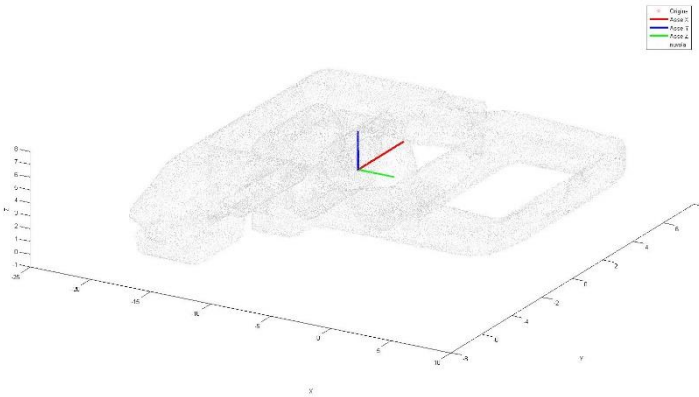


Figure 53. The found IRS for Din Rail Clip.

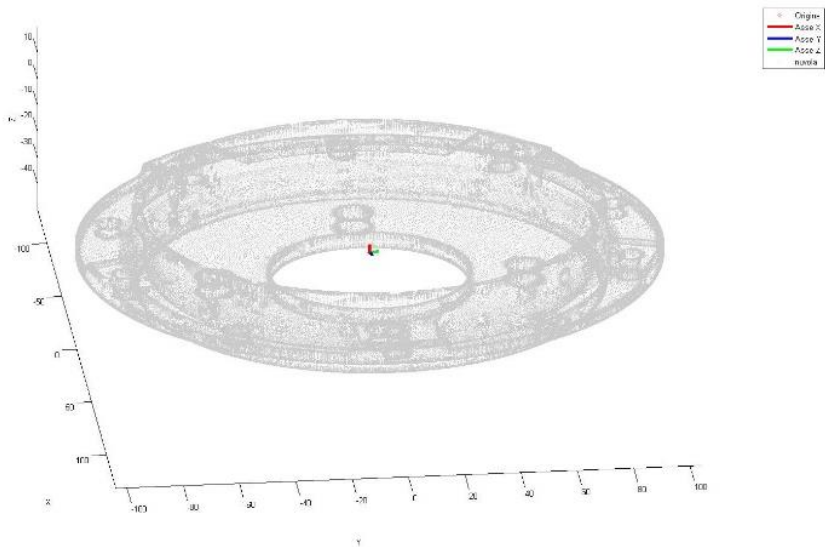


Figure 54. The found IRS for Flange (the x-axis of the recognised IRS is the central axis of the flange).

LM(Kasa) assumes that axes directions of the cylinders are oriented as the x-axis of the IRS. This assumption is consistent with the hypothesis of inspecting components by means of datum references equivalent to the IRS. Figure 55 shows the map of the voxel's osculating radii of the sections with smaller holes, confirming a good resolution of the proposed method. It has been found assuming a voxel structure of 64x64x16. Considering the 4 smaller holes, in the left part of Figure 55, the voxel evaluation found radii averaged values nearby 6 mm, while the 8 holes on the right are between 4 and 5 mm (see Blueprint in Figure 56).

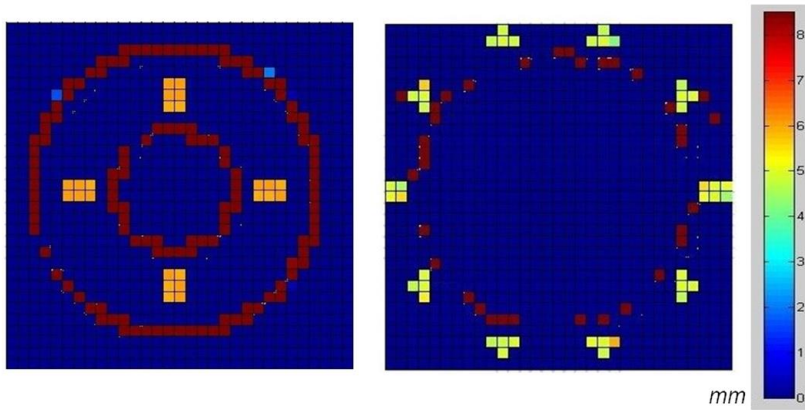


Figure 55. Flange for Aeronautical Application: LM(Kasa) evaluation of the radii associated to non-planar voxels.

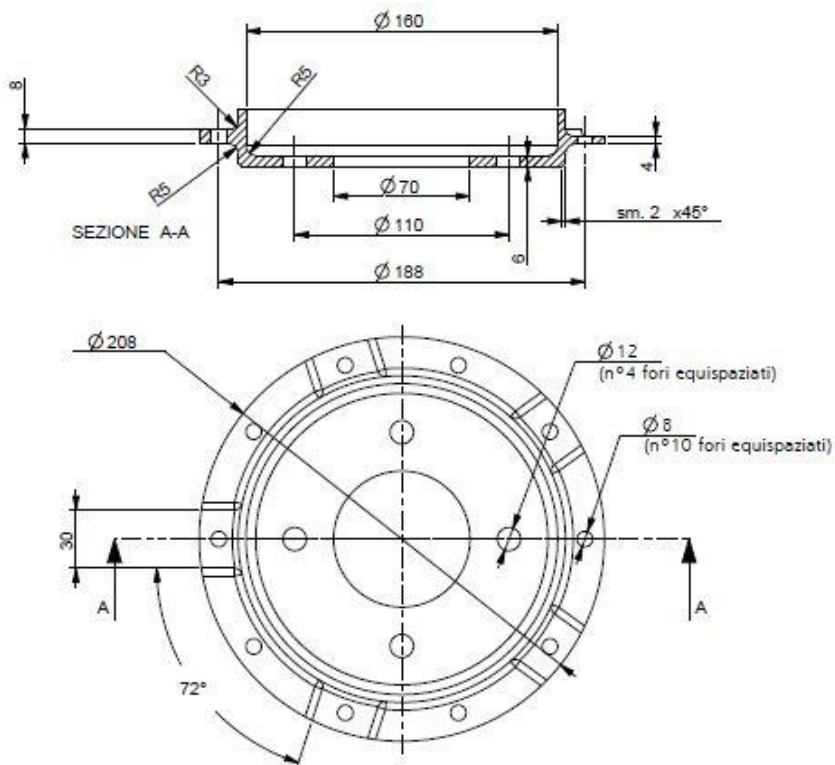


Figure 56. Flange for Aeronautical Application: particular of the blueprint of the component.

A preliminary validation of the voxel's osculating radius algorithm has been made comparing the voxel evaluation with surface reconstructions made in CATIA V5. In Figure 57, this reconstruction referred to the section of the left part of Figure 55 is shown.

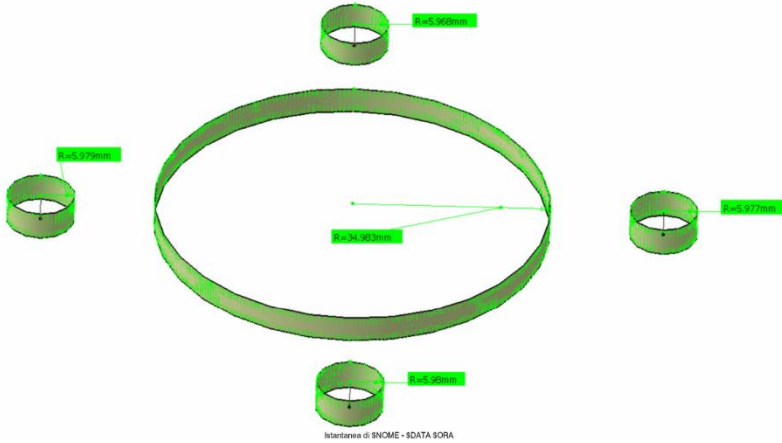


Figure 57. Validation of the surface reconstruction via CATIA V5.

The inner cylinder has a radius equal to 34.98 mm. Radii of the 4x12 mm holes are included in the range (5.97, 5.98) mm. All of them reveal - 0.02 mm of tolerance from the nominal values and good predictable ability of the osculating radius algorithm.

4.2 MLESAC algorithm

The Ransac-based fitting does not require a preliminary definition of the cylinder axis, although in some case of poor data (less than 6 points, the number necessary to find a first-guess axis), it may ask for. Other case of fitting error may occur when data are found to be not suitable to be inliers. It is a function of maximum distance and confidence that are Ransac input parameters. Assuming a constant confidence value (99% - default value), Table 9 shows the number of curved voxels that are found without cylinder fitting, changing voxel lengths (thus resolution of the voxel structure).

Resolution	V_{ijk} length (mm)	% of curved V_{ijk} that fail MLESAC
16x16x16	6.5x.6x1.9	1.50%
32x32x16	3.2x3.2x1.9	8.40%
64x64x16	1.6*16*1.8	35.80%

Table 9. Percentage of curved voxels that fail to find MLESAC solution – Maximum distance set to 0.1 mm, confidence=99%.

Changing the Maximum Distance according to 0.01 mm and 10 mm, no significant variation are found. In addition, changes of confidence do not gave significant variation. Therefore, curved without fitting parameters, in this case study, are due mainly to a low number of points in the voxels. To confirm that curved voxels without fit are mainly due to a low number of points inside, Figure 58 shows in red such points, for the case of the 32x32x16 voxel structure. Figure 59, for the same structure, shows the final segmentation in cylindrical and planar voxels, before applying the variance threshold analysis in the cylindrical voxels. It means that some cylindrical voxels may be rejected since many of their points are not well-fit.

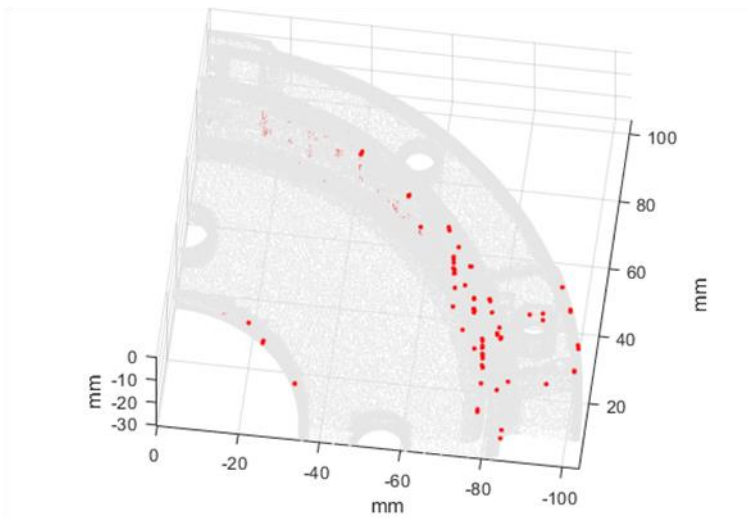


Figure 58. in red, points in voxels that fails the MLESAC fit due to less than 6 points in the voxels; (Voxel structure 32x32x16, Max Distance=0.01 mm).

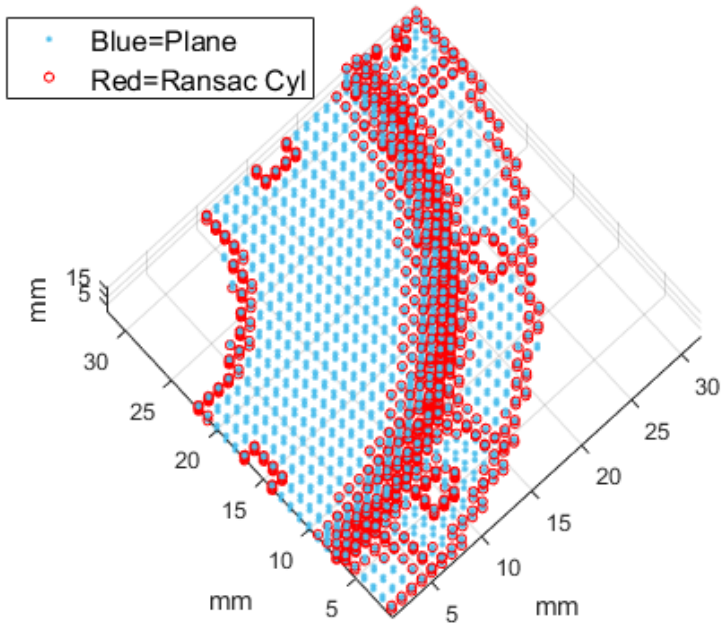


Figure 59. Final voxel partition in Cylindrical and Planar local surfaces (Voxel structure 32x32x16, Max Distance=0.01 mm).

Index of the suitability of the MLESAC fit in the voxel may be the variance of distance errors among points in the cylindrical voxels and fit radius. Figure 60 shows the high scatter founds in terms of mean of the distance errors from the fit radius, in the voxels.

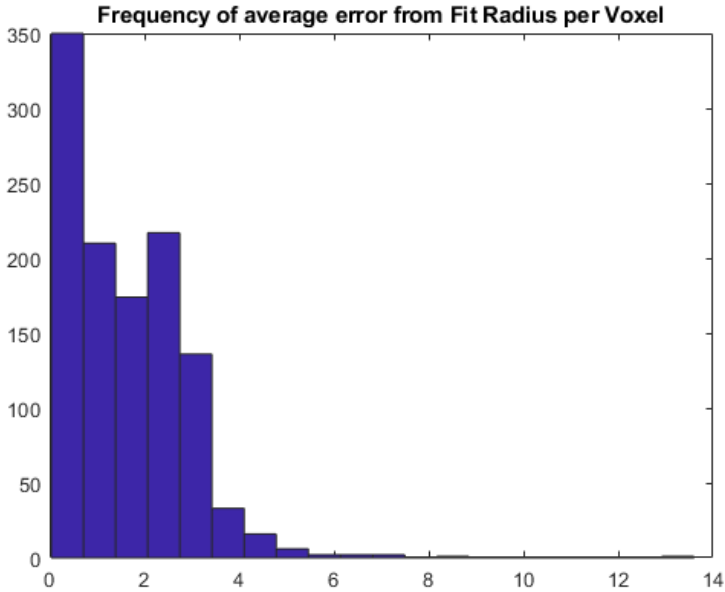


Figure 60. Frequency distribution of the occurrence of the mean of the distance errors from the fit radius.

Unfortunately, it is due to a bad evaluation of the radius and related axes in case of large curvature. Figure 61 shows the fit radius values in three sections where a threshold to the mean of the error distances equal to 3 mm, has been adopted. Large curvatures are not fit suitably, so their radii are scattered in the respect of the nominal values, resulting smaller than the expected values: 35 mm, in Figure 61(a), and 35 mm and 80 mm, in figure 61(b).

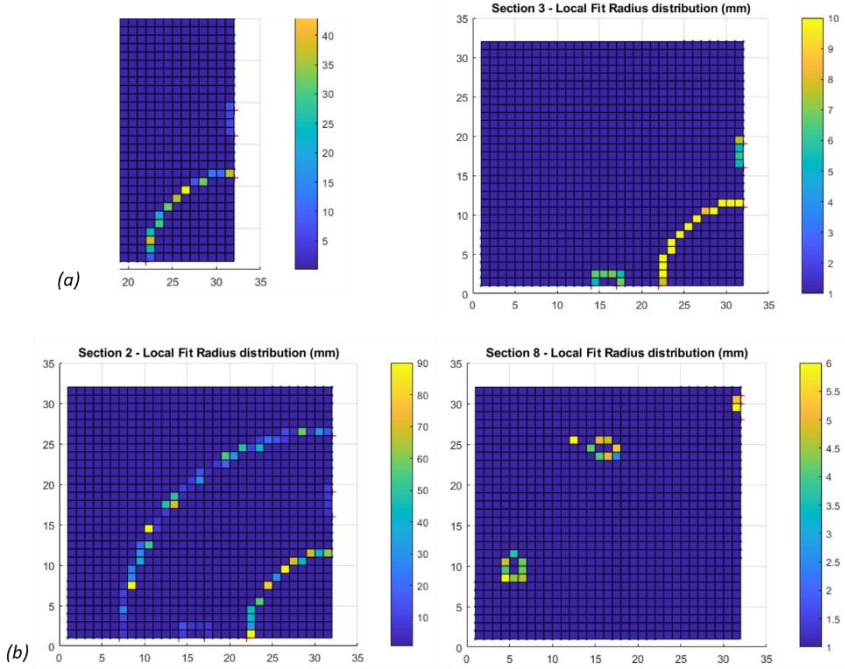


Figure 61. Fit radius distribution: (a) in section 3 of the 16 voxel subdivision along the z -axis; (b) in section 2 (on the left) and section 8 (on the right).

Imposing the axis direction as an input parameter for MLESAC, results change as follow:

1. an higher number of curved voxels failed to fit a cylinder, up to 60%;
2. a significant threshold can be found (Figure 62);
3. Radius of large curvature are improved (see for example Figure 63 in comparison with Figure 61(b))

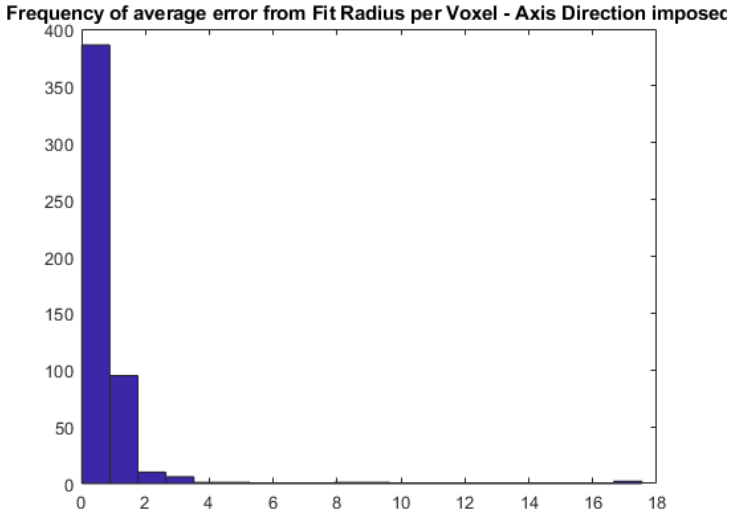


Figure 62. Frequency distribution of the occurrence of the mean of the distance errors from the fit radius – axis direction imposed in MLESAC.

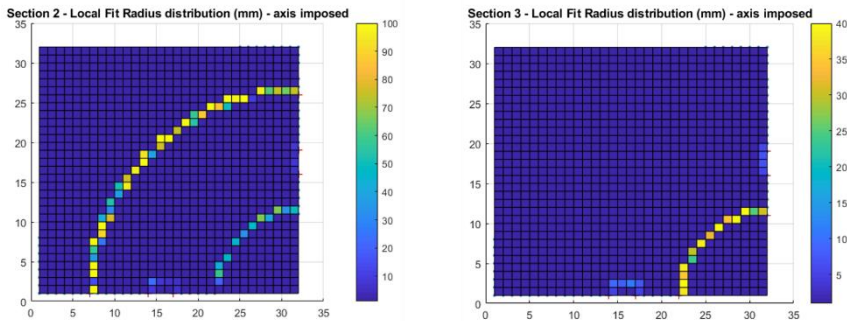


Figure 63. Fit radius distribution in section 2 (on the left) and section 3 (on the right).

5. Discussion

In this Chapter, the proposed algorithms and their variants have been shown in relation to test cases, significant for the major goals of the works: local surface distinction between planar and curved surfaces, clusterization of global planes and cylinders.

Voxel structures have been studied for each of them in terms of capability of describing the surface features of the component, achieving

the maximum allowable area for each of them. Thresholds for local planar voxels, namely the first bin of the variance histogram, has been studied, finding remarkable exception for axial symmetrical with low height/radius ratio (Flange for Aeronautical Applications). Nevertheless, the more stringent threshold can be also applied to the other case study with minor discrepancy (Din Rail Clip). In this case, small voxels approximate the large curvature wrongly, thus, some error in the definition of planar voxels may occur. Making more stringent the L2 orientation norm may release the problem.

Concerning the fitting algorithms for the cylindrical surface, LM(Kasa) shows good results despite the fact that asks for a preliminary knowledge of the cylinder axis directions. It can be solved by the IRS but, some approximation can be made. MLESAC may avoid this request, not in totality of cases, but more problems arise to find a proper threshold for affirming that the voxel is cylindrical with any doubt. It is due to problems about finding large curvature cylinders through points on a small arc length, when no axis direction is given as first-guess. This makes the fit model highly scattered also among contiguous curved voxels, ruining the region growing – hierarchical clustering of large radius areas. Imposing a first-guess direction, many curved voxels are not fit (60%), but radius evaluation highly improves.

Concluding, concerning cylindrical fitting, MLESAC cannot overcome the problems of LM(Kasa), that results more reliable for large curvature cylinders through points on a small arc length.

Chapter 5 –Measure and data management

This chapter outlines the measure extraction problems, focusing two points of views: (a) inspection protocol set-up and management; and (b) theoretical problems related to tolerance evaluation.

1. *Inspection data management*

1.1 *Inspection workflow and automation*

In order to be competitive and to not lose slices of market, in the last decades, the majority of companies decided to approach Computer Aided technologies, CAx, and principles like Concurrent Engineering. This means, generally, just a technological translation of issues, and only in some cases, an improvement in product/process development (Gabbia, 2016b). It is possible for each of the phases of lifecycle, to highlight some recent (or, often, historical) questions, that make CAx critical. Starting from the *Design*, in addition to the obvious necessity of realisation of functionalities for a piece, the extreme usage of CAD systems conduct to two main problems: storage of data and files and the actualisation of old versions of documents. Then, in *Production*, can happen that 3D-CAM models not contain enough information, making skilled CNC operators too fundamental for success. In addition, *FMEA* approaches (Failure Mode Effect Analysis) may cause enormous efforts in order to prevent errors from the design phase instead of high expensive corrections.

In *Measuring* and *Quality Control*, very often, controls are made without any focused help by technologies, due to the difficulties in CAT&I (Computer Aided Tolerancing & Inspection) implementation, causing possible errors in transcription and difficulties in versions management. In this phase, it is also complex to have a good comprehension of results, storing them in order to obtain an evaluation of components and the possibility of redesign through the information feedback. What results clear through this digression is the fact that having

all the possible information at the first stage and during the whole cycle becomes fundamental. Due to this, new standards, like ISO 16792:2015 (ISO16792, 2015), have the aim of integration of requirements and data for production and by quality checks into the CAD model, following PMI (Product and Manufacturing Information) concepts.

Passing to the research we are dealing, generally, in the applications of RE as inspection tools, the most common workflow is related to CMM and laser acquisitions and involves the steps in Figure 64. It can be regarded as a general CMM measurement protocol that is enriched with CAD capabilities, like data management and automatic extraction of tolerance specification and solid model reference (Campana & Germani, 2008), (Germani, et al., 2010).

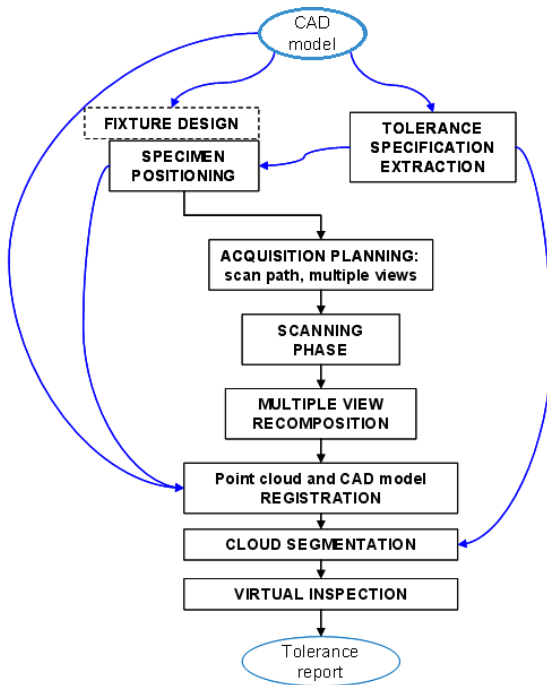


Figure 64. Steps of common workflow related to CMM acquisitions.

There are three main critical points, which become often the bottlenecks of such implementation:

- registration of the point cloud with the CAD model that may ask for expensive fixtures or interactive procedure for applying ICP algorithms;
- accuracy of the multiple view recomposition;
- efficiency of the segmentation algorithms.

Each of these points often requires manual interactions between CAD model and reverse engineering software, causing time (and sometimes information) loss.

In case of inspections on a large number of electromechanical plastic specimens, as it happens during die set-up in our analysis, these interactions must be avoided and generally, no specific fixtures are used except a reference table. So, point cloud and CAD model registration becomes less relevant. In addition, the results of the inspection often require the report of many dimensional tolerances, better described as standard 2D technical drawing or datasheet instead of a deviation distribution on a solid model.

It is clear to understand what are causes of researches, like this one, on *ad-hoc* procedures in order to by-pass the registration phase through an inspection independent from the CAD model (except for the extraction of the tolerance specification). This leads to a simplified workflow, shown in Figure 65, where the point cloud and CAD model registration is replaced with the cloud segmentation. This workflow, passing through the extraction of tolerance specification, avoids the registration phase, using part type recognition to obtain the necessary references used.

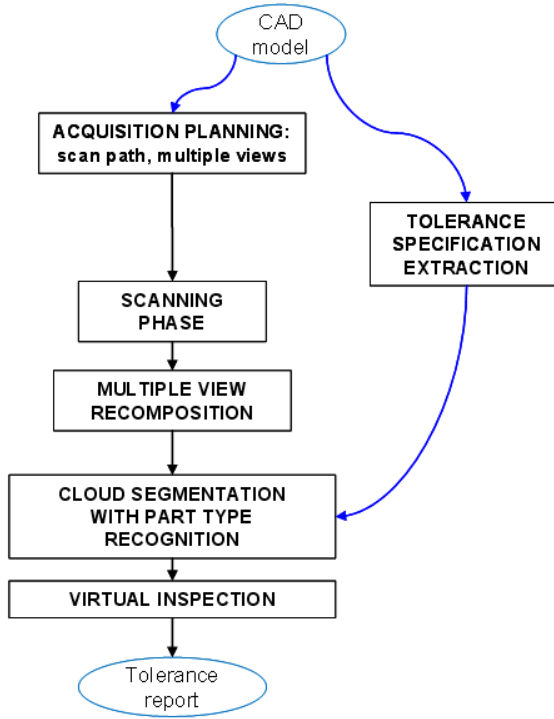


Figure 65. Workflow based on part-type recognition.

Although part type recognition is far from the aim of this work, voxel-based segmentation can be suitable to reach this goal by applying image analysis techniques derived from artificial vision algorithms. In fact, voxel structure is similar to a slicing of the part and boundary analysis may be suitable to analyse protrusion like summarised in Figure 66 (Bici, et al., 2014).

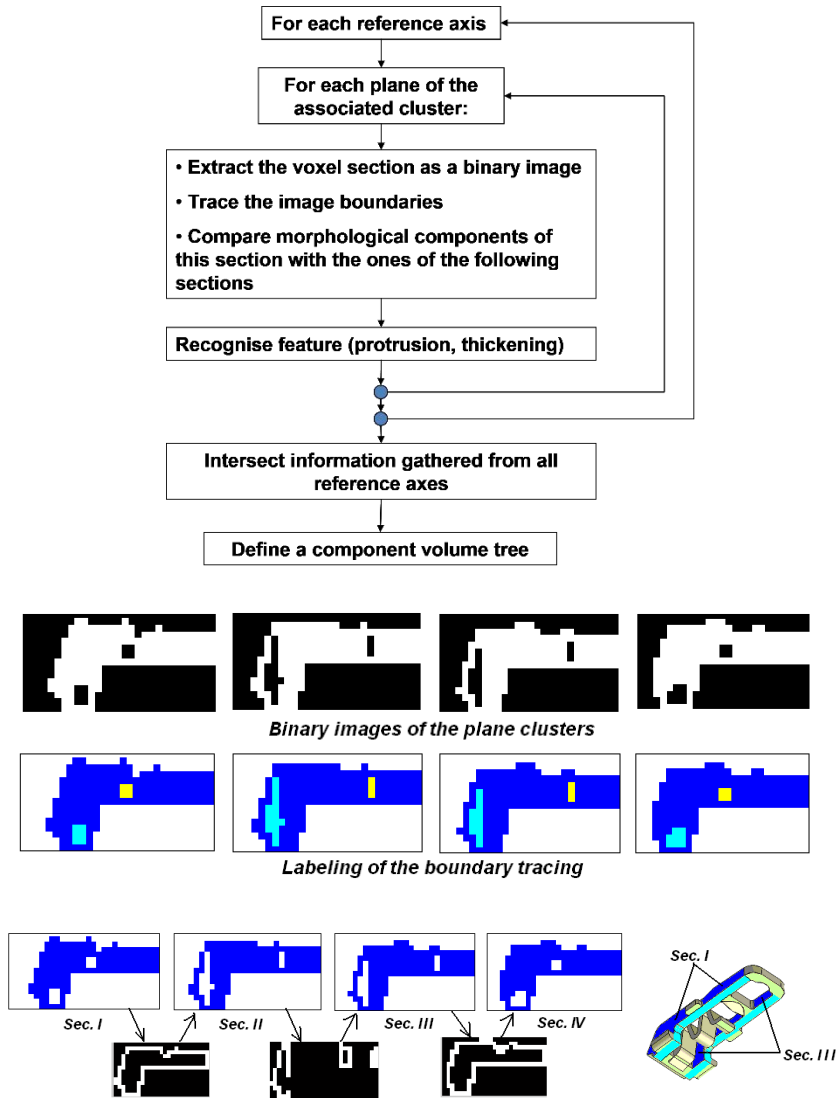


Figure 66. Example of automatic part type recognition: logical workflow and example of binarisation and boundary tracing of four plane sections.

1.2 PDM

To achieve benefits from the automatic inspection via RE, a full integration of the inspection protocol into the PDM must be provided. According to this requirement, a Product Data Management (PDM) tool must be defined with the aim of:

- comparing interesting measurements with the nominal quotes derived from CAD model;
- reporting both detailed and “at a glance” overview of the measurement protocol results;
- aiding data analysis to decide which component’s feature or length must be re-analysed or modified in terms of a cavity’s die set-up or component’s design.

Figure 67 summarises the optimization strategy for the integrated product-process of an injection moulded component, on the upper part; and the PDM steps implemented to aid this strategy, on the lower part.

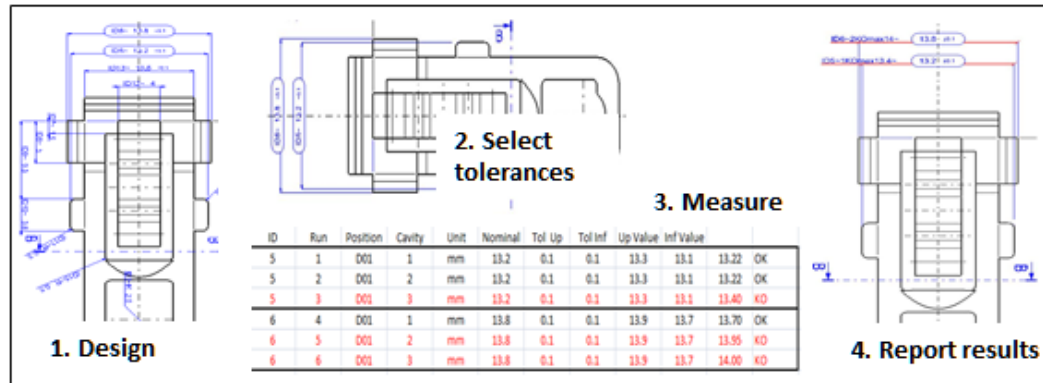
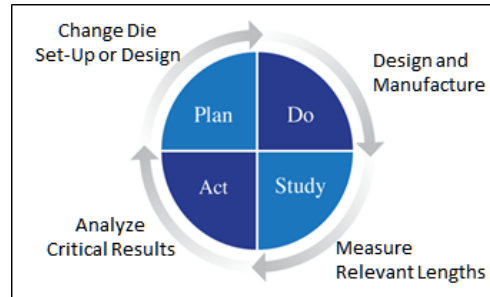


Figure 67. Product-process integrated optimization of injection moulded parts: strategy (on the upper part); PIDM steps to support it (on the lower part).

Detailed data are given by listed results numbered according to a drawing that through colour and flags may give a visual overview of the results:

- red = not accepted tolerance with related number of cavities and mean value
- green = accepted tolerance with related number of cavities
- orange = further decision necessary.

2. Standards and practice to assess the measures

In order to obtain such a PDM, the measurement phase assumes a key role, in relation to tolerance data obtained by the nominal CAD. Tolerances and their accurate expression on draft is one of the main issues, also for standardization organizations. From the born of ISO/TR 14638 and ISO/TC213 for *Dimensional and Geometrical product specification and verification*, coincident with the advent of GPS (Geometrical Product Specifications) and its matrix (Figure 68), arriving to the latest standard ISO 14638:2015 (ISO14638, 2015), one of the main principles about tolerances is the fact that tolerances, expressed in the drafts, represents the functional limit for the piece. In other words, the tolerance must take into account all the useful information for component in terms of manufacturing and usage, expressing a value that is a limit between the good functioning and no functioning zones. Tolerancing is the connection between specification and verification (Figure 68), giving the possibility of an exact (as much as possible) conformance evaluation.

	Chain links						
	A	B	C	D	E	F	G
	Symbols and indications	Feature requirements	Feature properties	Conformance and non-conformance	Measurement	Measurement equipment	Calibrations
Size							
Distance							
Form							
Orientation							
Location							
Run-out	<i>Specification</i>				<i>Verification</i>		
Profile surface texture							
Areal surface texture							
Surface imperfections							

Conformance

Figure 68. ISO GPS standard matrix model, (ISO14638, 2015).

In ISO 14638:2015, one of the most important issue is the principle of independence, which can be summarised in the assessment that every single type of tolerance expressed on a quote must be considered independently from the others.

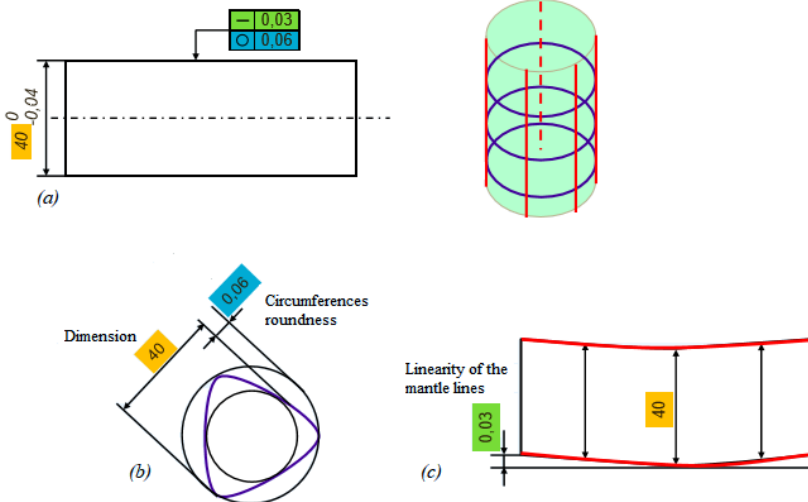


Figure 69. The independence principle.

In Figure 69, the independence principle is explained, managing dimension roundness and linearity tolerances in separated ways.

Another important issue to take in mind is the fact that, although very accurate, our measurement through laser CMM system is digital, composed of acquisitions of discrete single points. So that, diametric measurement, like the one reported in Figure 70, cannot be considered as correct before managing them with segmentation and best-fit.

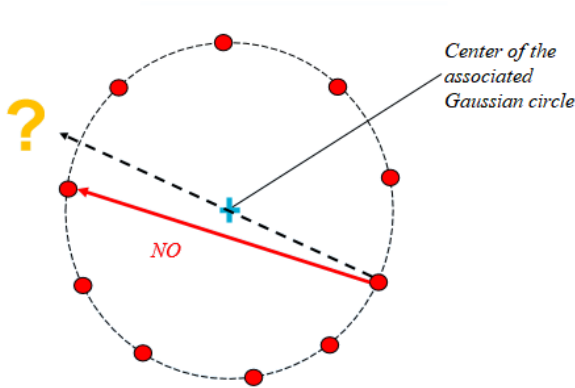


Figure 70. Measurement by discrete points.

For our research, we decided to take into account these issues through the development of the different methods of measurement that we called Gauge, Min-Max Range and 10-90 Percentile, as explained in next section.

2.1 Proposed approaches

For measure extraction in inspection via RE, industrial procedure is usually based on distance analysis cloud-CAD after registration. Replication on multicavities may be addressed via macro definitions, but sampling points on each surface for statistical measure is not so used. Starting from the clusterization made as described in Chapter 3 and 4, for measurements between two planes, each distance between couples of faces in the same orientation is computed. Doing so, no registration with CAD model is required, automating the repeatability of the dimensioning measures in comparison with other samples of the same component, since measures are referred to intrinsic directions of the component, as found by clusters and eventually the IRS.

To take in account all the possible differences with the nominal value, maintaining the possibility of recognition of different causes of deviation by the datum, we developed three different algorithms of measurement, summarised in Figure 71:

1. Gauge simulation;
2. Min-Max Range;
3. Percentile Analysis.

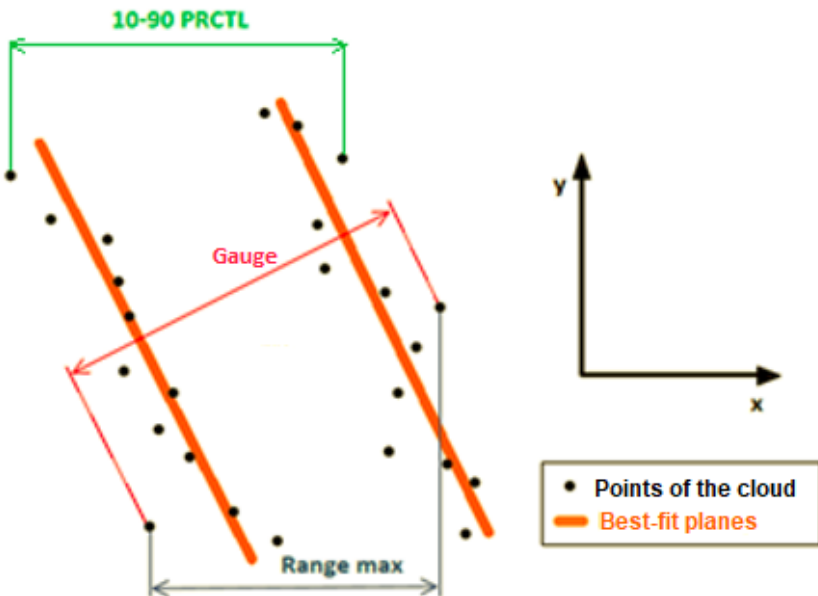


Figure 71. Graphical visualisation of maximum measures done through three different methods.

They have been developed bearing in mind that, in comparison with other standard measurement systems, the high number of points, belonging to each face, may increase the capability of inspection, using statistical consideration on distances of points from their related best-fit plane.

Gauge simulation extracts and measures couples of points, selecting, along the normal direction to the planes, minimum, maximum and

average values. With the Gauge, distances are considered, in normal direction to faces, random sampling couples of points. As the number of points belonging to each face can be different, the minimum number is considered, sampling an equal number in the other face to obtain couples. Among all the obtained random distances, as said, minimum, maximum and average values are selected by the algorithm for the visualisation in a developed GUI. The Min-Max Range calculates the distance between faces centroids (calculated using the entire population of points involved), reporting it together with minimum and maximum distances found adding distances of the two couple of the most outer and inner points of the cases. 10-90 Percentile analysis outputs a deeper overview of the distance distribution, computing the average distance as the distance between the median position (obtained by best fitting planes) of each face and the maximum and minimum values as percentile distances (10% or 90%). This allows refining measures, cutting off outliers or couples of points that are not statistical relevant. Last two methods are processed along the considered principal direction. It is important to remember that could be present an error of orientation angle, caused by thresholds, between the normal direction of faces and the principal direction whom they are referred. In order to control geometrical tolerances, values for planarity are reported in terms of frequency occurrence of the distance between points of each face of the considered couple and their related best-fit plane. A GUI has been developed to show to the operator results obtained by every method for each measure. Examples of measures and GUI report are shown in Figure 72 and 73.

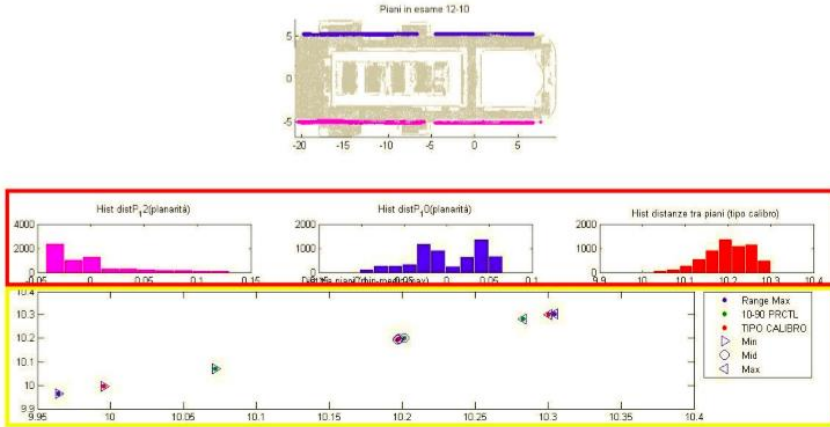


Figure 72. Example of measurement GUI for Din Rail Clip. In the red box, for planarity evaluation, distances histogram from best-fit planes are reported; in the yellow box, the coupled measures with the three proposed methods (minimum, average and maximum values for each).

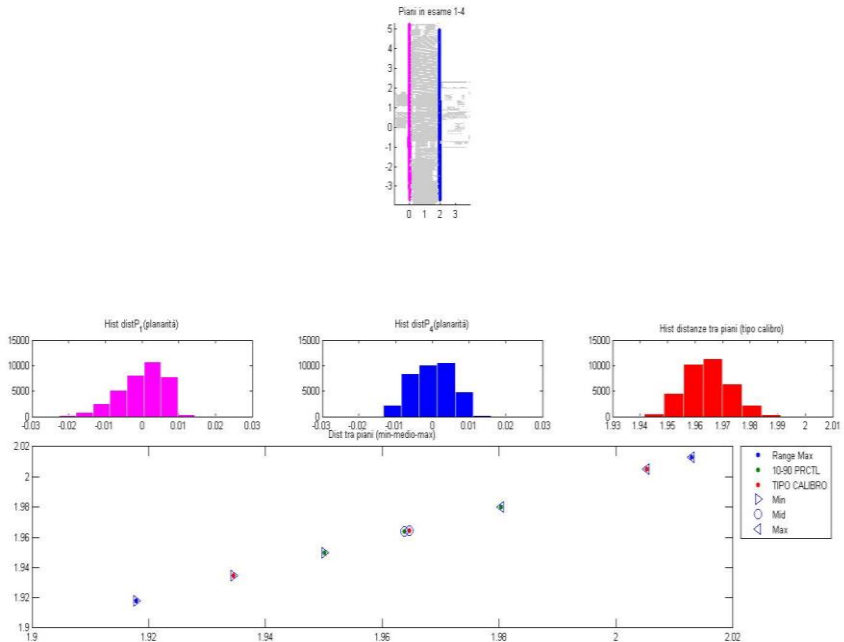


Figure 73. Example of the measurement GUI for Latching Lever.

Similar reasoning can be made for cylindrical surfaces both in terms of distances from its fit surface or computed axis, and reciprocal axis orientation and distances.

3. *Summary of the expected errors*

From the error chain point of view, the absence of the CAD-cloud registration and of the manual interaction should result as a benefit. Leaving as a further next investigation the quantitative assessment of the error of each step, Table 10 summarises the source of approximations to understand the goodness of the approach.

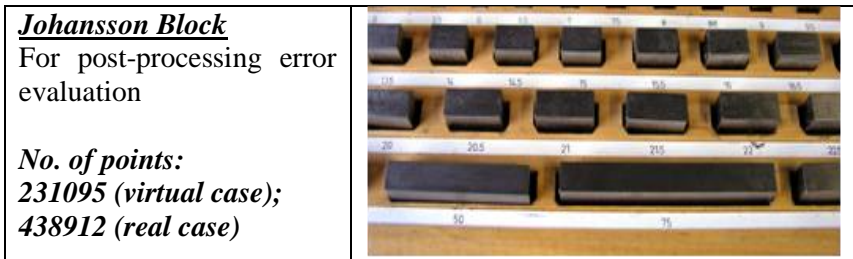
Proposed approach	General workflow
Error of acquisition, split into error of the laser and error of the CMM movement	
Error of multiple view reconstruction	
IRS recognition or datum positioning	Registration with CAD
Fitting error of global surface (<i>NOT MANDATORY</i>)	Fitting error of global surface for distance analysis

Table 10. Sources of possible errors.

In our approach, global surfaces may not be fit for measurement purpose, since the segmentation aims only to recognise the points to be measured. Thus, fitting may be done optionally, or in very specific cases, as that related to cylinder axis.

3.1 Post-processing a Johansson block

To confirm both the error of the acquisition procedure and the irrelevance of the segmentation post-processing on the final error, we made a virtual Johansson block point cloud, obtaining a measurement, through the developed algorithms, not influenced by the acquisition system. Then, we used a real Johansson block (nominal dimensions of 10 x 25 x 2 mm has been used, in which 2 mm is the nominal thickness) of the same dimensions and thickness to evaluate the magnitude of the error introduced by the system.



Johansson or gauge blocks are parallelepipeds in stainless steel. Through the usage of Catia V5, the virtual block has been created with dimensions of 10 x 25 x 2 mm, the same nominal dimension of the analysed real block, and successively a “nominal” point cloud has been generated from the block.

Number of points of the cloud	Fixed number of voxels	Elapsed time
231095	32	11'
	16	3'
	8	1'30"

Table 11. Computation time of virtual Johansson block for different number of fixed voxels.

Analysing the virtual cloud, with fixed number of voxel equal to 32,16 and 8 for each dimension (computation time is reported in Table 11), with every method used, the average value for the nominal thickness is 2.000 mm, without any sensible variation, consequently, it is possible to affirm the correctness of the developed algorithms. In addition, in every case, the number of identified planar features is equal to six, obviously the faces of the parallelepiped. So that, we can assert that the error introduced by the measurement procedure in clouds is not significant for our scope.

Therefore, the analysis can be focused on the real blocks. In order to avoid errors due to registration of multiple views, only one view of the real block has been acquired.

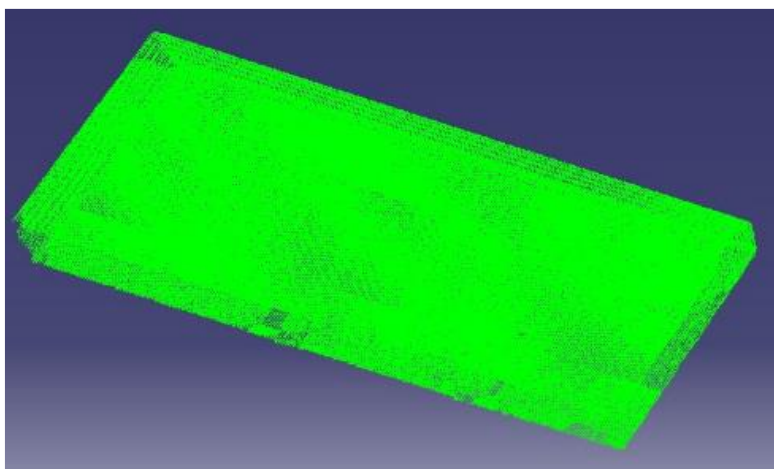


Figure 74. Johansson block point cloud.

No issues connected to noise have been found, except the fact that a mat spray (a white developer for porosity checks) has been used to avoid reflection. It is declared to be able to deposit on the layer piece between 0.05 and 0.1 mm, so the presence of two layers (one for each plane on our measurement) could have influenced results. In order to have more data to compare, several measurement, using a Palmer, have been done. Thickness measurement has been replied nine times on different areas of the block. In every replication, the same value has been found: 2.001 mm. This involves that, comparing Palmer measurement with the nominal dimension, can be noticed an error of 0.05%. The measurement through

the GUI procedure described in Section 2.1 of this Chapter, has been summarised in Table 12.

Number of voxels	Method 1 Range Max	Method 2 10-90 percent.	Method 3 Gauge
32	1.959 mm	1.909 mm	1.960 mm
16	2.013 mm	2.010 mm	2.013 mm
8	2.031 mm	2.030 mm	2.031 mm

Table 12. Obtained thickness values (in mm) for the three methods.

The three methods are quite similar in correspondence of the same voxel structure. Nevertheless, different results are found among them. Considering that the virtual block does not show significant variations among methods, discrepancy from the palmer measurements may be due to spray thickness, not uniformly deposited, and the huge difference of the number of points used in the measurement made by RE.

4. Discussion

In this Chapter, some considerations about the whole inspection workflow have been made. In particular, a PDM oriented to multicavities has been proposed and three methods to approach the plane tolerance inspection have been set. To evaluate the possible benefit of the workflow, not only in terms of inspection speed, some considerations and preliminary tests about errors have been made, using virtual and real component, a Johansson block.

Virtual block revealed good agreement between measured plane distance and nominal, with errors less than 0.001 mm. It is a preliminary confirmation that, with adequate number of points per voxels, IRS and surface clusterization without fitting may not introduce errors in the post-processing. Concerning the real acquisition of the block, Palmer measurements may be not comparable with the RE elaboration, not being

able to capture mat spray thickness (layer removal during Palmer measurement is quite easy), or shape deviations due to wear and bad storing conditions of the block.

Chapter 6 - Case studies

Pieces studied in this research are components belonging to electromechanical assemblies for circuit-breaker and electrical plants, realised by ABB (one example of these assemblies is reported in Figure 75). Selected pieces, from the huge production of the company, are those which characteristics can well be implemented into the developed routine, in order to obtain reliable results and to test all the algorithms. In fact, there are pieces for which the usage of the procedure could be not really useful due to their features limited or huge dimensions, that cannot be acquired and processed accurately.

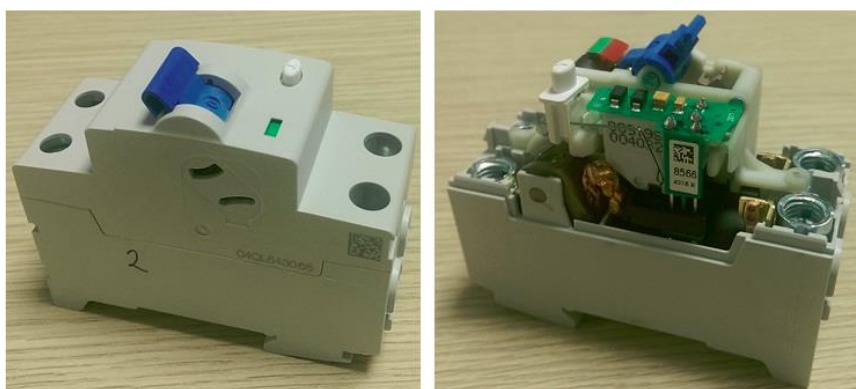


Figure 75. Example of an electromechanical assembly produced by ABB (with and without the cover).

We developed this stage with a dual aim:

1. Evaluate the algorithms robustness with different components taken from industrial cases (we used components like Cover and Test Button);
2. Focus the proposed algorithms in the general framework of the industrial application. It means analysis of multicavities, managing acquisition planning and giving information about measurement data management (we used components like Latching Lever and Handle).

1. Presentation of the case studies

In Table 13, the used test cases are reported, giving preliminary information about their dimensions, materials and colours.

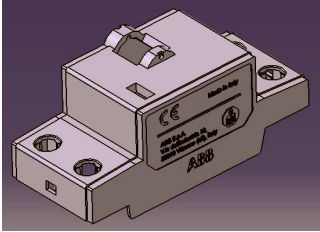
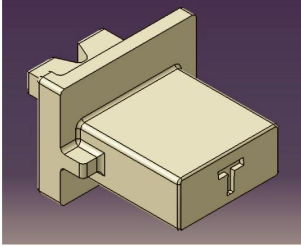
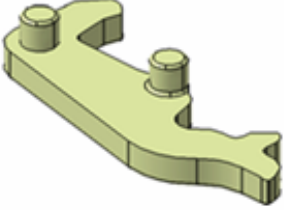

<p><u>Cover</u> Nominal dimensions = $85 \times 35 \times 37.4 \text{ mm}$ No. of cavities = 1 Material: Polyamide Colour: Light Grey</p>	
<p><u>Test button</u> Nominal dimensions = $8 \times 10.8 \times 13.4 \text{ mm}$ No. of cavities = 1 Material: Polyamide Colour: White</p>	
<p><u>Latching Lever</u> Nominal dimensions = $20 \times 10 \times 4 \text{ mm}$ No. of cavities = 4 Material: PPS Colour: Light Brown or Black</p>	
<p><u>Handle</u> Nominal dimensions = $22.5 \times 15 \times 16.5 \text{ mm}$ No. of cavities = 8 Material: polycarbonate (charged with fibers) Colour: Black</p>	

Table 13. Used case studies.

1.1 Cover

This piece, reported in Figure 76, is realised in polyamide and its maximum nominal dimensions are 85 x 35 x 37.4 mm.

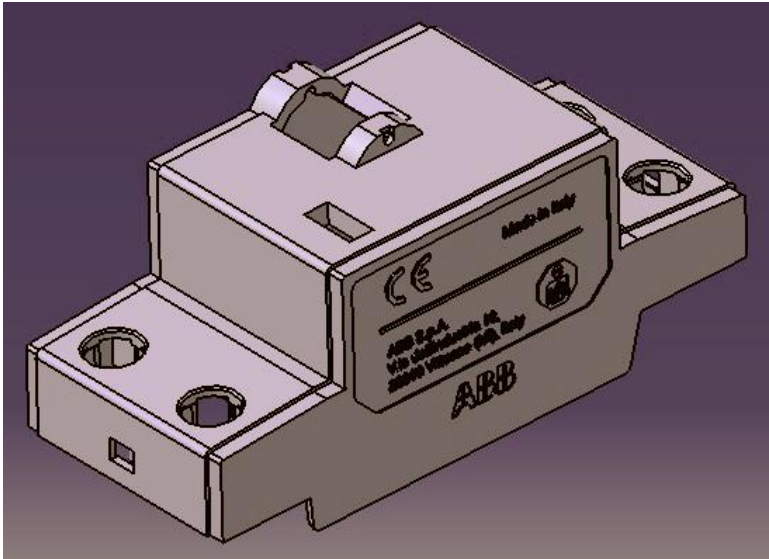


Figure 76. Cover (Code: 04237696 Cover 2P 35 MMQ RCCB MIRAD).

Its role is the connection with the breaker's base and the protection of all the internal components. The material and its finishing are chosen taking in mind that the component must be interfaced to the final user, for this reason, also the colour is subject to regulation norm, and it is established that it is light grey.

We use this case study to report data for the acquisition set-up, and, mostly, for evaluation of the measurement stage and data, using a component of large dimensions and processing a “heavy” cloud in terms of number of points.

Starting from the choices for set up the acquisition, the CAD model of the piece, in STL format, is submitted to the developed related GUI. These algorithms returns three suggested orientations and the positioning for the acquisition, related to the number of considered cavities. The elapsed time of this procedure was 35 minutes. This value is elevated, in

relation to other pieces and it maybe depends from the presence of the embossed logo and codes that increases the surfaces to be processed, in addition to all the internal particulars existent. Even if it is out of the main goals of this thesis, we found that a calibrated defeaturing in the CAD model, before the creation of the STL format, could help in terms of elapsed time.

Number of cavities and clouds	1
Dimensions	85 x 35 x 37.4 mm
Number of views (suggested/possible)	3 of 4
Elapsed time for acquisition set-up (GUI)	35'

Table 14. Characteristics and input data of the Cover for the acquisition set up.

In this case, only one cavity has been analysed. The acquisition GUI returned 4 possible orientations (as explained in Chapter 2), and we selected the 3 reported in Figures 77, 78, 79.

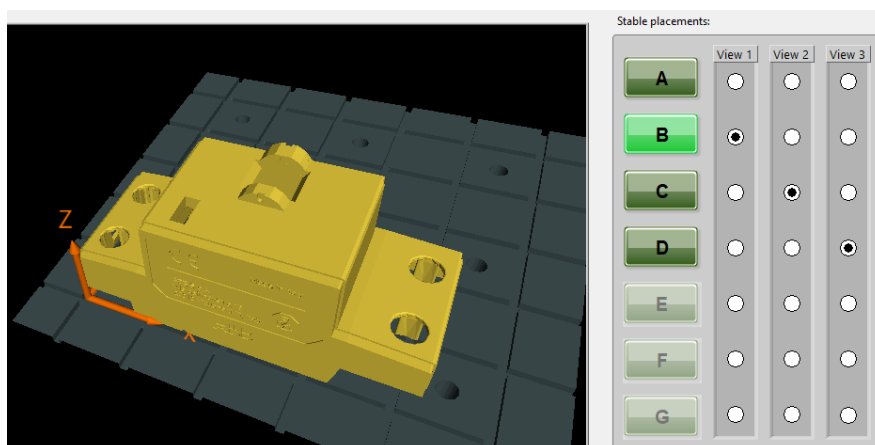


Figure 77. First selected orientation for Cover.

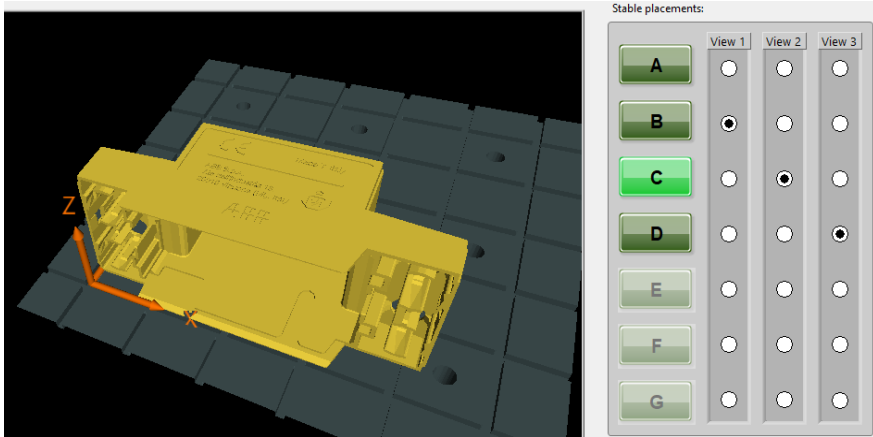


Figure 78. Second selected orientation for Cover.

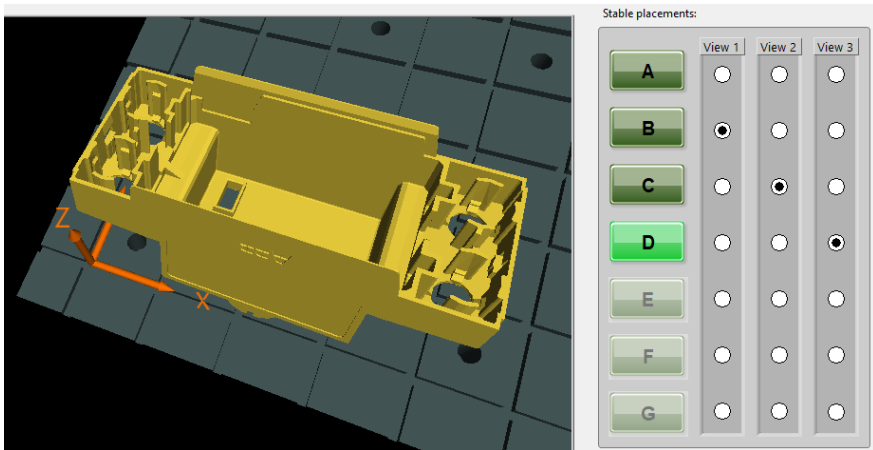


Figure 79. Third selected orientation for Cover.

The not selected orientation is reported in Figure 80. As it can be easily seen, it is quite similar to the second chosen one (Figure 78).

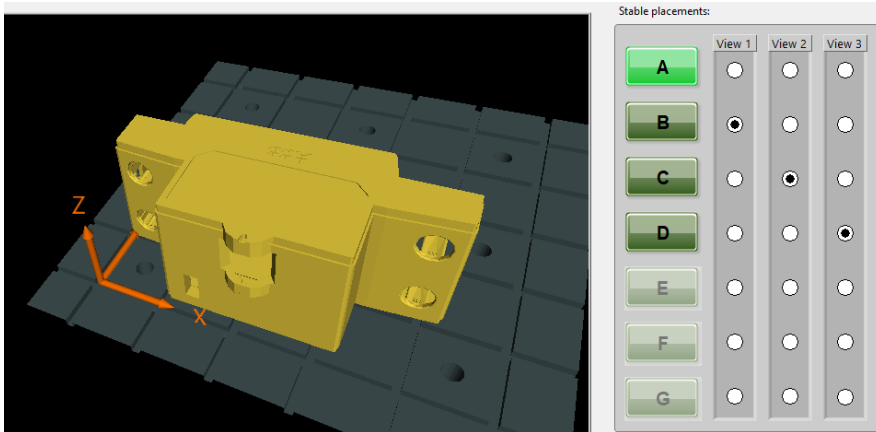


Figure 80. The unselected orientation given by the GUI for Cover.

The suggested positioning, due to the mono-cavity, in this case is not considered.

Through the dedicated algorithms, laser paths and orientations have been generated, and the acquisition returned a cloud with a huge amount of points, 4507331, because of the high number of feature in the internal part and the large total dimensions in relation to the resolution of the laser scanner in terms of point spacing (22 μm , as reported in Chapter 1).

The chosen resolution of the voxels structure to be superimposed has been 32x32x32, as reported in Figure 81. This choice could seem not adapt compared to the high number of points and to the dimensions. Nevertheless, in this phase the target is to obtain an accurate segmentation of the external surfaces, which are wide planar or cylindrical.

32x32x32 Voxel Structure

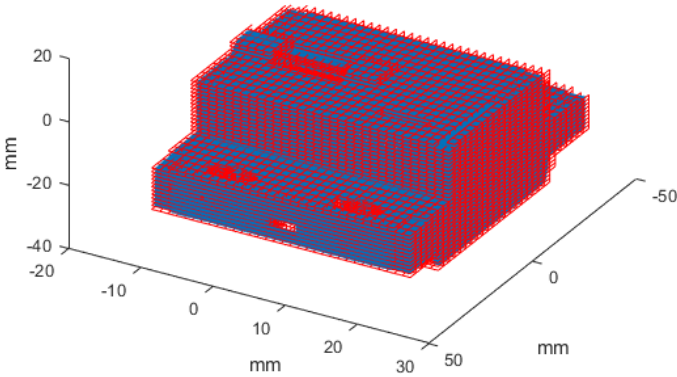


Figure 81. 32x32x32 Voxel structure superimposed on Cover point cloud.

Due to this voxel structure, obtained data can be reported in Table 15.

$k_x \times k_y \times k_z$	32x32x32
% of $V_{ijk} = 1$	23%
V_{ijk} length (mm)	2.69x1.12x1.18
Average No. of points per V_{ijk}	596
Clusters of plane orientation	6
%Curved $V_{ijk} = 0$ after thresholds	11%

Table 15. Data obtained through the segmentation procedure for Cover.

We want to focus the attention on the fact that this cloud is more than 30 times greater than other clouds usually processed by the developed algorithms. Obviously, using a usual zoom ratio ($r, s, t = 5$), also the average number of points per V_{ijk} results enormous. However, the segmentation procedure resulted able to find, in this configuration, only six direction. Among them, the most populated by voxels resulted to be the three approximating the principal directions of the component.

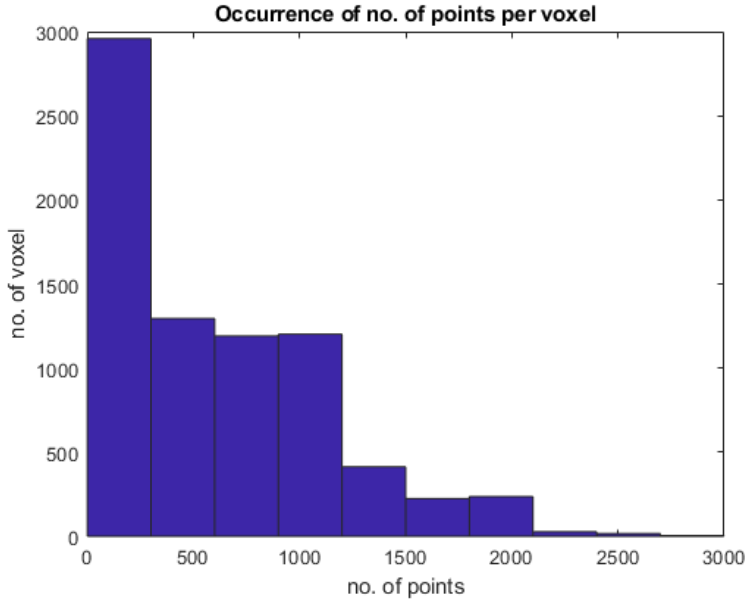


Figure 82. Occurrence of number of points per voxel for Cover with the superimposed 32x32x32 structure.

From the occurrence histogram (Figure 82), the general trend is confirmed (as seen in Chapter 4), with a concentration in the first bin and a flat trend for the other three or four bins, however numbers both in terms of number of voxel and of points are greater.

Obtained plane orientations are reported in Figure 83.

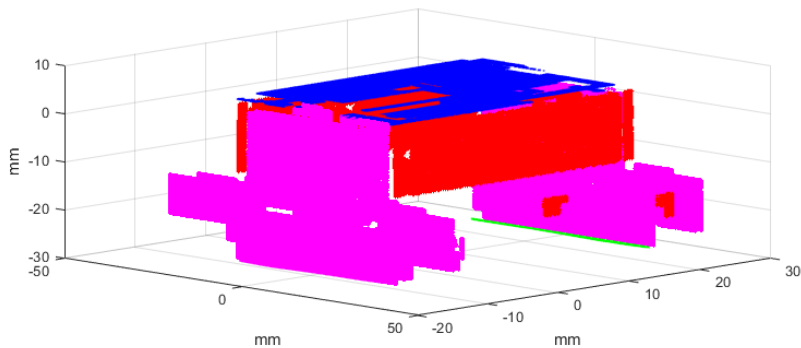


Figure 83. Plane direction sets for Cover.

As it is easy to understand, this procedure is valid for the outer surfaces of the component. In order to obtain a correct segmentation of the internal features, one possible solution could be to design an adaptive voxel structure that can set automatically the voxels lengths in relation to the local distribution of points. This will be the main future target in this research.

Nowadays to solve the problem, the possibility is to split the cloud into fractions that are more easily processable. One example of this has been developed with the application of MLESAC in a half of the Cover point cloud (Figure 84). The result is detections the two main cylindrical features in the lower part. The procedure was applied without the use of the first guess in input for the direction, demonstrating the loss of accuracy that, in cases like this, affects those algorithms.

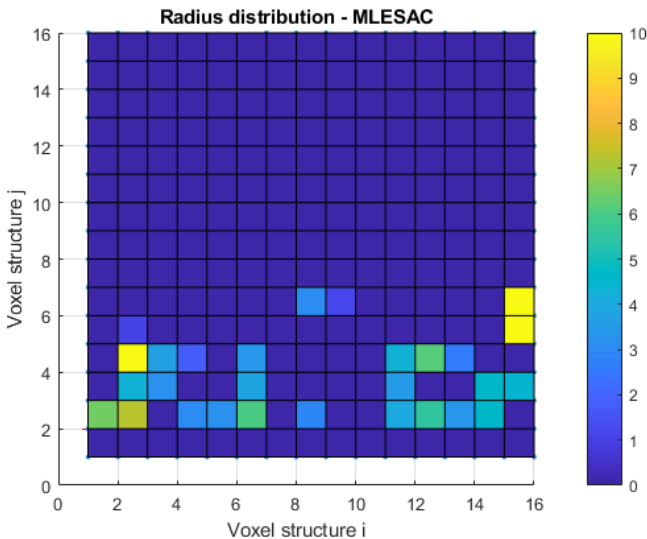


Figure 84. The application of MLESAC in the divided cloud of Cover.

1.2 Test Button

This component, shown in Figure 85, is made in polyamide, a plastic material with high values of resistance and non-flammable. The cost of polyamide is, generally, higher than polyoxymethylene (material used in

cases like Din Rail Clip), due to the possibility of obtaining a more accurate finishing, characteristic that becomes fundamental in pieces used like interfaces with users as the button. Nominal maximum dimensions of the button are 8 x 10.8 x 13.4 mm.

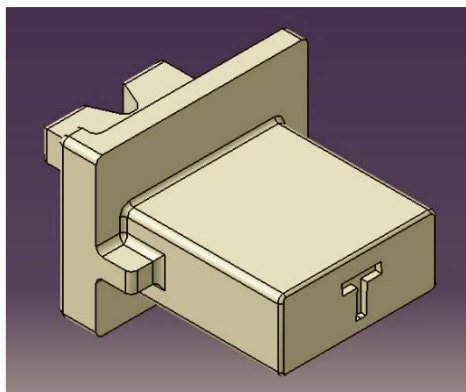


Figure 85. Test Button (Code: 04237756 Test Button RCBO MIRAD).

It is placed near a breaker handle, it is used to close the internal circuit, verifying the correct functioning. As all the pieces visible from the outside of the breaker, it has a standard colour, white for the acquired case. The button is effectively the slider of a prismatic joint, and it has only one degree of freedom, the axial movement. It is in contact with a torsion spring. After having the breaker connected and the handle armed, through the press of the test button, it is possible to make a rotation of the spring causing the closing of the secondary circuit with the primary one. This produces a short circuit, simulating a problem in the plant. Through this procedure, the correct functioning of the breaker can be verified. As it can be easily understood, the correctness and the respect of tolerances in a piece like the test button can be fundamental for the entire plant.

The aims of analysing this component are to report obtained data for the acquisition set-up, and, especially, evaluate measurement stage and data. The acquisition set-up algorithms returned three suggested orientation (reported in Figures 86, 87, 88), due to the single cavity considered, the positioning given by the algorithm is not essential. In this

case, the elapsed time, 2', was really short because of the simplicity of the component, in terms of features.

Number of cavities and clouds	1
Dimensions	8 x 10.8 x 13.4 mm
Number of views (suggested/possible)	3 of 7
Elapsed time for acquisition set-up (GUI)	2'

Table 16. Characteristics and input data of the Test Button for the acquisition set up.

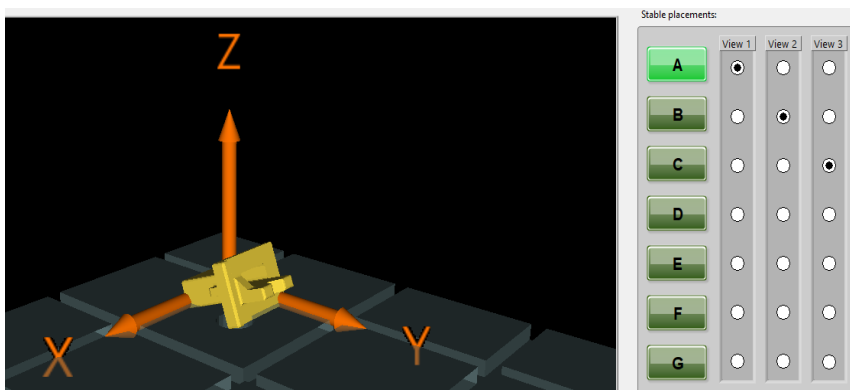


Figure 86. First selected orientation for Test Button.

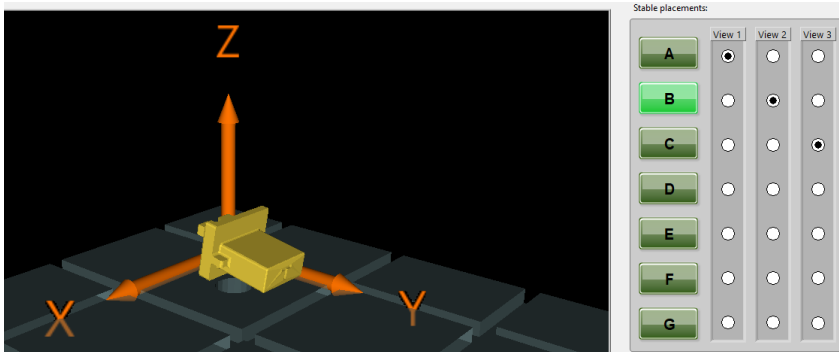


Figure 87. Second selected orientation for Test Button.

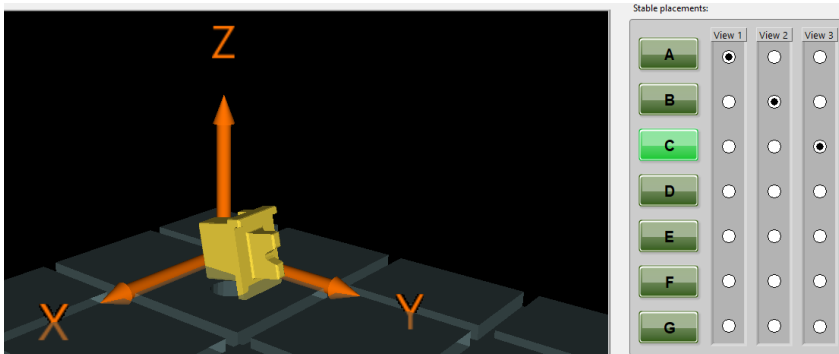


Figure 88. Third selected orientation for Test Button.

The four not selected orientations are reported in Figure 89; they results similar or less stable than the selected ones, which were suggested by the algorithm.

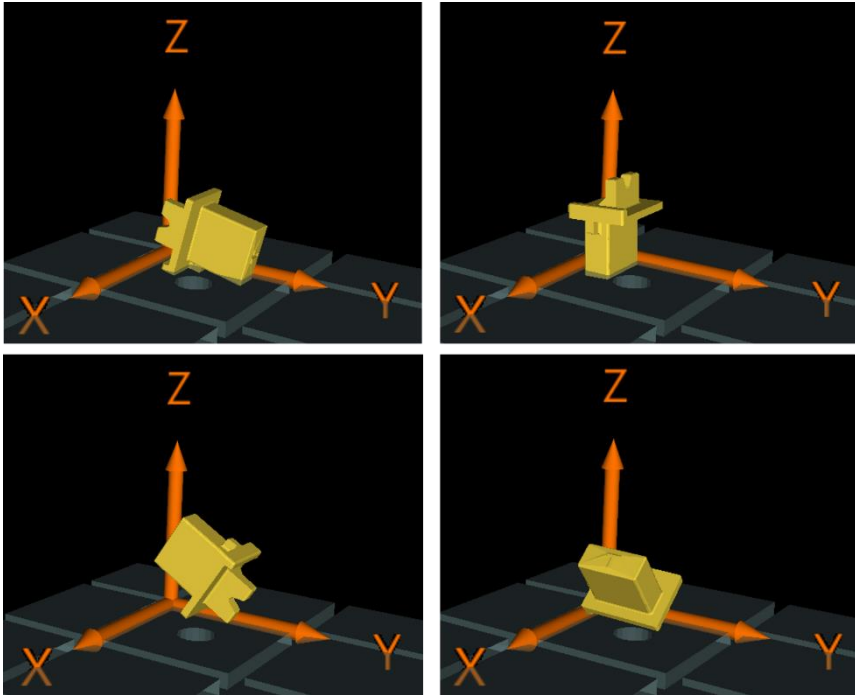


Figure 89. The four unselected orientations given by the GUI for Test Button.

In this case, due to the fact that the acquisition was executed on one single cavity, the positioning on the acquiring table is not significant. The GUI have created all the paths to submit to the acquisition software (Focus) and the scans have been done.

After the registration and recombination of partial clouds, the total point cloud has been determined (Figure 90). It has composed of 188449 points.

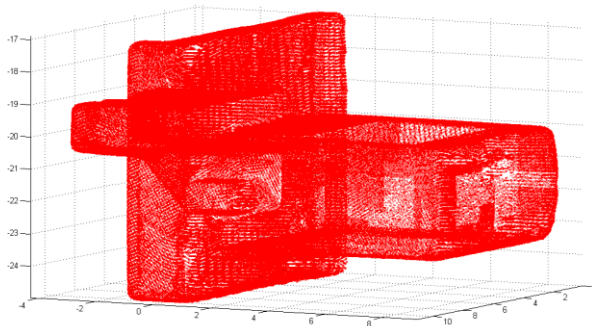


Figure 90. The obtained point cloud for the considered sample of Test Button.

Then, in order to reach a correct segmentation some attempts have been done, looking particularly to obtain reliable results for the wide planes that have to guarantee the correct function of the slider. So that, due to reasoning similar to those exemplified in section 2 of Chapter 4, we obtained two voxel structures. The structures, $32 \times 32 \times 32$ and $32 \times 64 \times 16$, have the same number of voxel but different distributions. Data obtained by the superimposition of these structures to the cloud are reported in Table 17.

$k_x \times k_y \times k_z$	$32 \times 32 \times 32$	$32 \times 64 \times 16$
% of $V_{ijk} = 1$	13	15
V_{ijk} length (mm)	$0.36 \times 0.44 \times 0.26$	$0.36 \times 0.22 \times 0.52$
%Planar $V_{ijk} = 0$ after thresholds	7	31
Average No. of points per V_{ijk}	43	59
Clusters of plane orientation	3	5
%Curved $V_{ijk} = 0$ after thresholds	6	50

Table 17. Comparison between the two considered voxel structures for Test Button.

From data, although there are similar percentages of $V_{ijk} = 1$, the (32x64x16) structure can highlight two directions more than the (32 x 32 x 32) structure, having, however a slightly worse distribution of points inside voxels. In fact, looking at Figure 91, the number of voxels of the first bin is higher for the (32x32x32), which have also a distribution of occurrences less flat than the other structure. Final clusters obtained for both the analysed structures are reported in Figure 92. The presence in (32x64x16) of two more directions is not significant because these directions are limited in terms of composing voxels and they represent not planar features like the portion of edge represented in red in the right side of Figure 92. We can assume the 32x32x32 structure as the better resolution for this component, maintaining the aim of analysis the wide planar features present on the component, postponing higher zoom ratio to more accurate research, focused on less extended features.

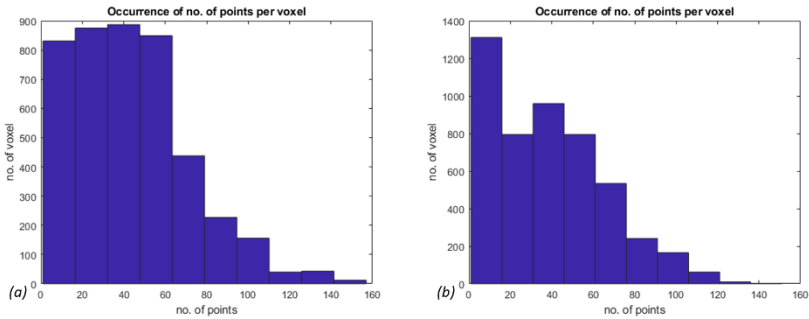


Figure 91. Occurrences of number of points per voxel: (a) 32x32x32; (b) 32x64x16.

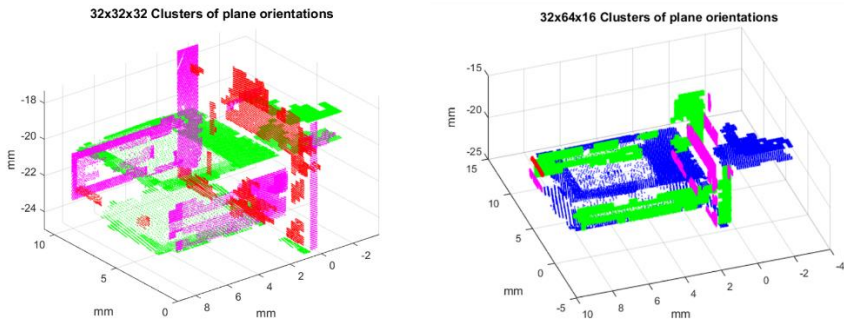


Figure 92. Plane orientations; 32x32x32 voxels (on the left) and 32x64x16 (on the right).

The procedure has been continued with the cylinder recognition. As shown in Figure 93, the main cylindrical feature, by drawing prescriptions, is the one on the right with a radius of 0.5 mm. Looking at voxels found cylindrical by MLESAC (Figure 94(a)), through the imposition of Z axis as input data, we found correspondence in terms of values (Figure 94(b)). Threshold values on the mean of the error distance points-axis have been set equal to 0.1 mm. This confirms the MLESAC good capability of small radii recognition, making it a correct choice in term of algorithms for pieces of characteristics similar to this case.

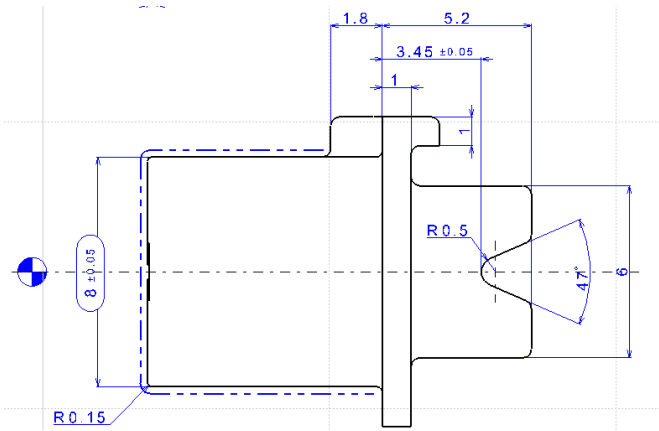


Figure 93. Example of nominal measure.

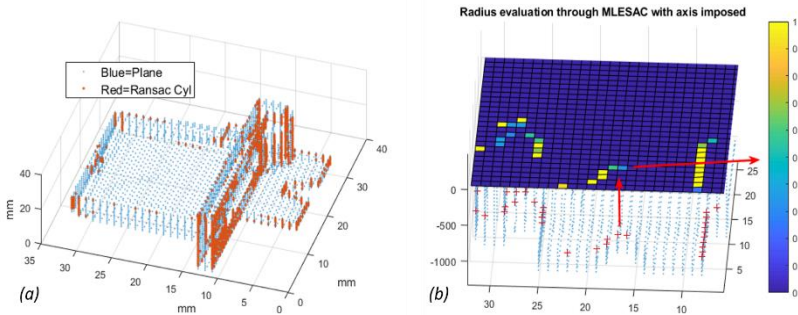


Figure 94. 32x32x32 Cylindrical voxels through MLESAC: (a) partition; (b) Radius evaluation.

1.3 Latching Lever

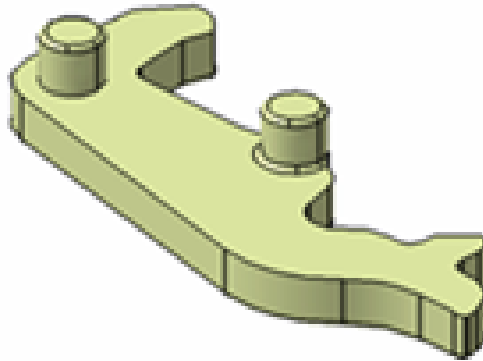


Figure 95. Latching Lever (Code: 04235556 Latching Lever RCBO).

The Latching Lever is used in assemblies of electromechanical switches of electric panels. The part is made of polyphenylene sulfide (PPS), through an industrial process of plastic injection moulding. Due to its installation and use, the compliance of the nominal values of prescribed dimensions and tolerances is fundamental, mostly in the areas of cylindrical pins, which allow the final housing and functioning in the assembly. Characteristic lengths are about 20x10x4 mm, more than one sample has been acquired obtaining, after multiple view alignment, point clouds of over 60000 points.

We use this case study to report data for the acquisition set-up, and to evaluate performances of LM(Kasa), giving also an example of results obtainable through the use of MLESAC with the same direction input.

Through the acquisition set-up algorithms, we found three orientations, reported in Figures 96, 97, 98, chosen in a set of seven proposals, maximising orientation stability and the accessibility by the scanner.

Number of cavities and clouds	4
Dimensions	20x10x4 mm
Number of views (suggested/possible)	3 of 7
Elapsed time for acquisition set-up (GUI)	1' 30"

Table 18. Characteristics and input data of the Latching Lever for the acquisition set up.

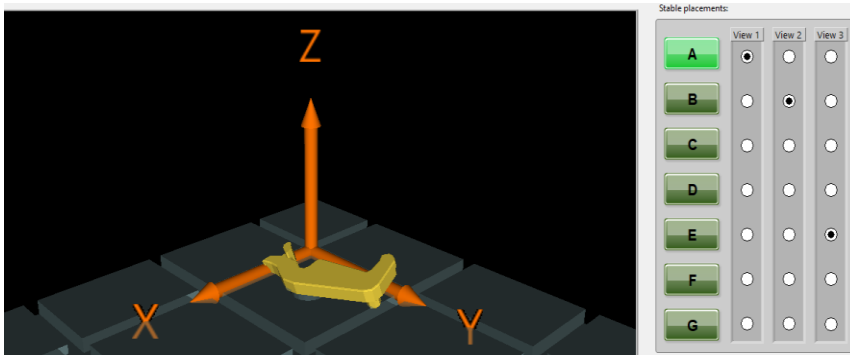


Figure 96. First selected orientation for Latching Lever.

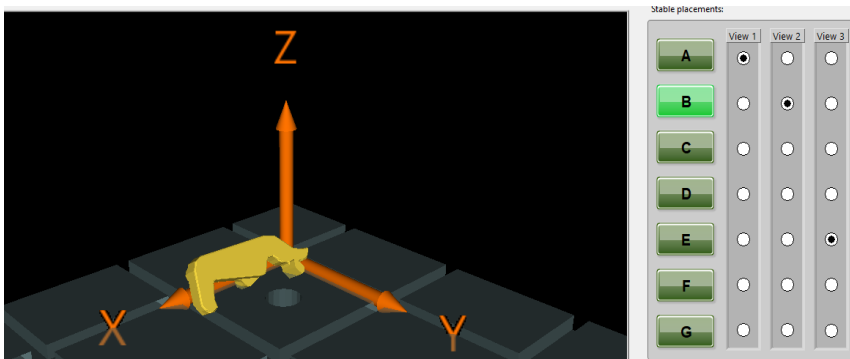


Figure 97. Second selected orientation for Latching Lever.

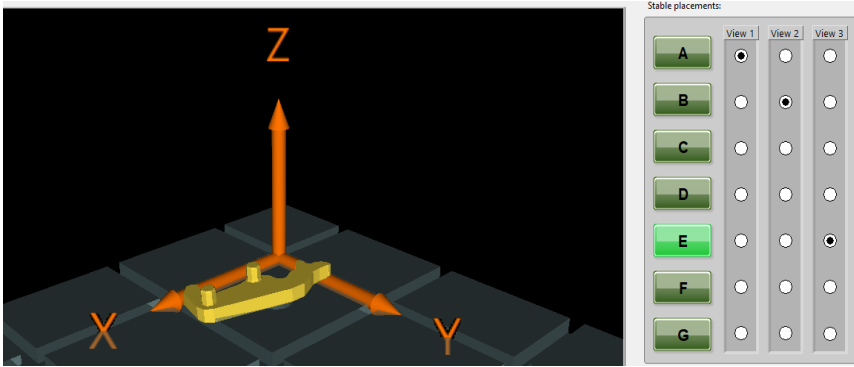


Figure 98. Third selected orientation for Latching Lever

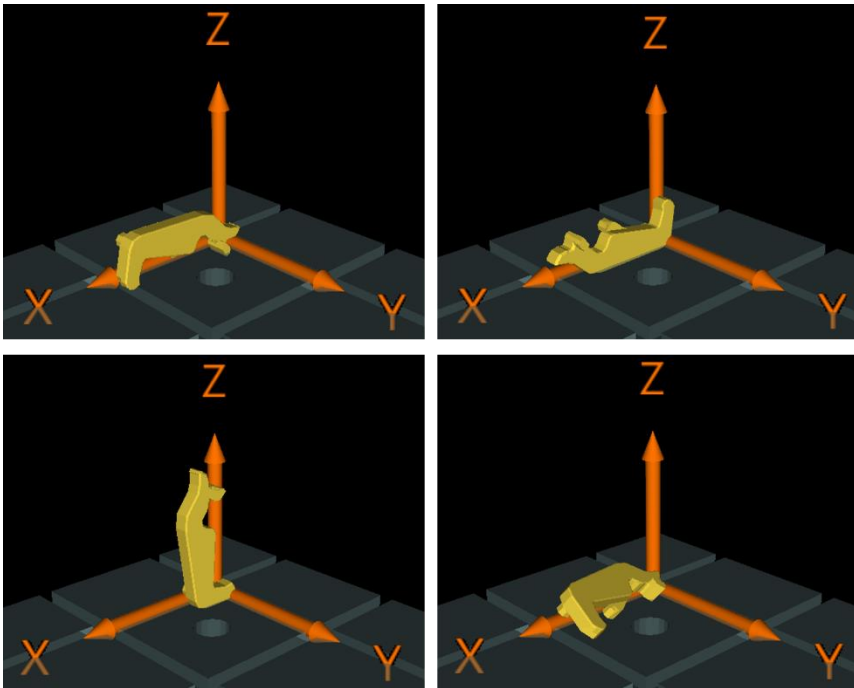


Figure 99. The four unselected orientations given by the GUI for Latching Lever.

To evaluate the usefulness of the algorithm to cluster planar and cylindrical surfaces, we select an equally-spaced voxel structure made of 32x32x32, obtaining data reported in Table 19.

$k_x \times k_y \times k_z$	32x32x32
% of $V_{ijk} = 1$	13
V_{ijk} length (mm)	0.17x0.64x0.31
%Planar $V_{ijk} = 0$ after thresholds	9
Average No. of points per V_{ijk}	21
Clusters of plane orientation	3
%Curved $V_{ijk} = 0$ after thresholds	46

Table 19. Data obtained through the segmentation procedure for Latching Lever.

Through the iterative threshold, 1689 planar voxels are found from the 3077 previously defined as “true-state” voxels. Figure 100(a) shows the voxel structure, in red, superimposed to the point cloud, in blue; Figure 100(b) distinguishes points of planar and curved voxels through colours, green and blue respectively.

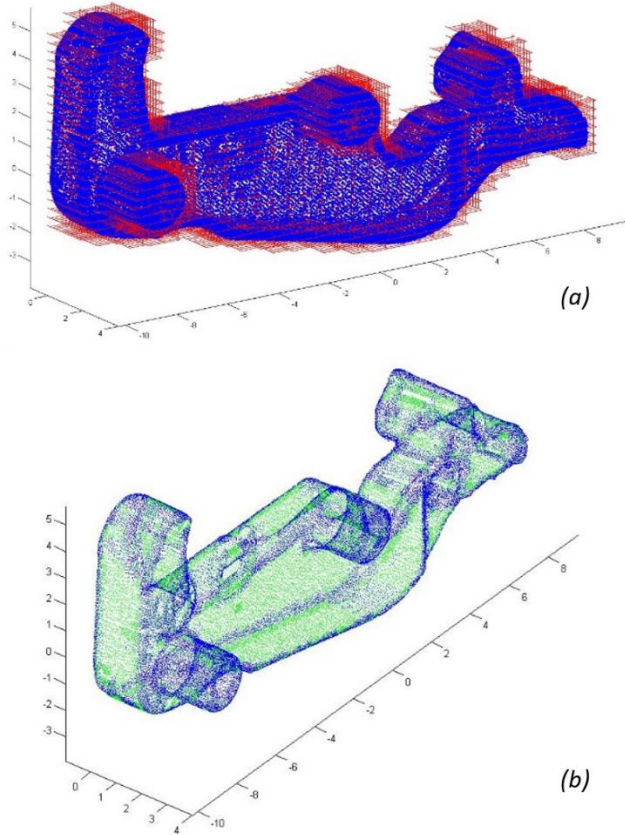


Figure 100. Latching Lever: (a) 32x32x32 voxel structure; (b) local surface recognition planar features in green, curved features in blue.

Local planar voxels are then clustered to recognize the component's planar faces via the hierarchical clustering and region-growing algorithm. Through a L2 norm threshold, the local planar voxels are divided in sets in which planes are recognized as parallel. In the considered case, the L2 norm threshold admits an error of 1% between planes coefficients.

Then, we have found the sets of parallel planes, and we must consider connections between voxels, to cluster together component's faces. From the planar voxel clusterization, the IRS of Figure 101 can be found. As already mentioned, generically, in the pieces usually scanned, the cylindrical features appear to have axis directed according to one of these

three directions. This remains true in the considered lever, since IRS x-axis is the direction of many cylinders present in the component.

From the segmentation point of view, the cylindrical analysis in this case is successfully made also by LM(Kasa). The circumferences are local approximation of the points in the curved voxels, after their projection on the IRS.

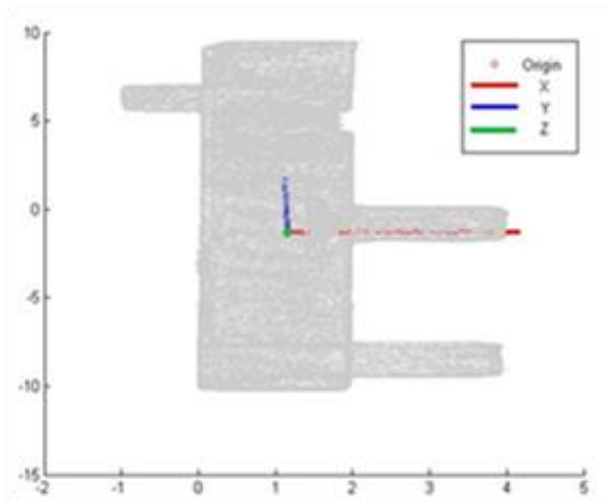


Figure 101. Lateral view of the Latching Lever with its IRS.

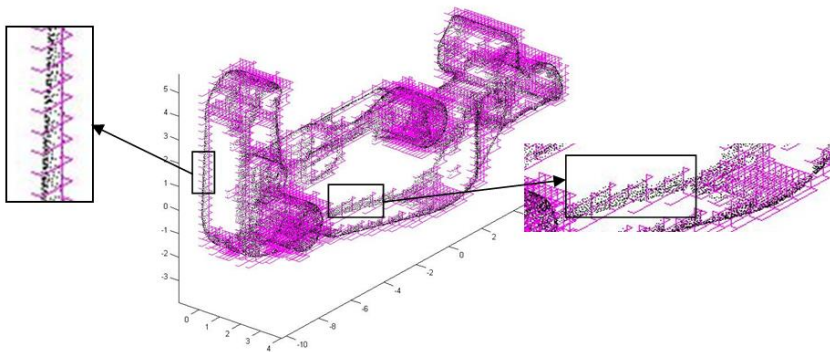


Figure 102. Curved voxels recognized in the Lever before cylinder recognition.

Then, only one of the three circumferences for each voxel is selected, it is the one having the minimum value of variance of the distances from the circumference of the best-fit resulting from the calculation in each

voxel. Analogously to the planar case, we must impose a threshold on the values of variance, to distinguish truly cylindrical voxels from the others.

The algorithms for the automatic selection of the threshold, as previously described, are now reapplied, for the cylindrical case, three times, once for each principal direction. We start from the same values of first guess of the planar case (20 bins). Results are shown in Table 20. The first row reports the values of the first guess of the algorithm for the automatic threshold, the second row reports the optimal number of bins obtained, in the third row, there are the values of the calculated threshold, in the fourth, the recognized curved voxels without the iterative computation and in the latest, the number of the recognized cylindrical voxels with the iterative computation.

<i>Directions</i>	Direction X	Direction Y	Direction Z	Total
<i>Initial number of bins</i>	20	20	20	
<i>Final number of bins (optimal)</i>	55	48	48	
<i>Variance Threshold (mm²)</i>	3,42*10 ⁻⁶	6,91*10 ⁻⁶	5,45*10 ⁻⁶	
<i>Final number of cylindrical voxels</i>	793	262	333	1388
<i>Initial number of curved voxels</i>	569	62	82	713

Table 20. Automatic selection of variance threshold for finding cylindrical voxels.

After the cluster recognition, cylinder reconstruction and measurement must follow according to the required inspection protocol. To give a preliminary evaluation of the soundness of the proposed approach, cylinders A, B and C of Figure 103 have been compared with interactive post-processing made by Catia. In this case, Cylinder A has an effective value of R=0.974 mm, we also obtained R=0.972 mm (for

Cylinder B) and $R=0.999$ mm (for Cylinder C). Standard deviation of the fittings are always less than 0.012 mm. Through the proposed algorithm, the radii of the single clusters are: 0.974 mm for cylinder A and B, 1.036 mm for cylinder C with a standard deviation less than 0.006 mm.

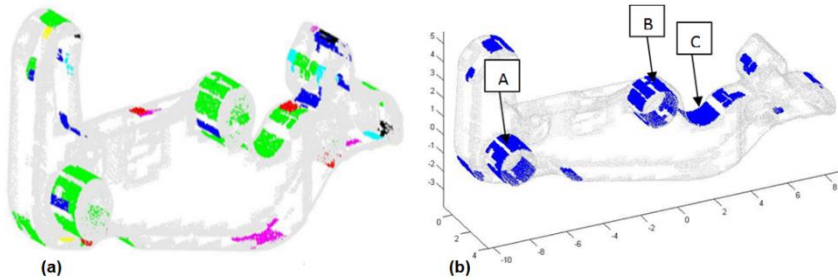


Figure 103. (a) Set of points of the clusters found in the X-direction; (b) Cluster of $R=1$ mm cylinders.

Using MLESAC with imposed axis $(1, 0, 0)$ as input parameter, similar results are obtained, with an improvement on the curvature detected in the free-form part (Figure 104).

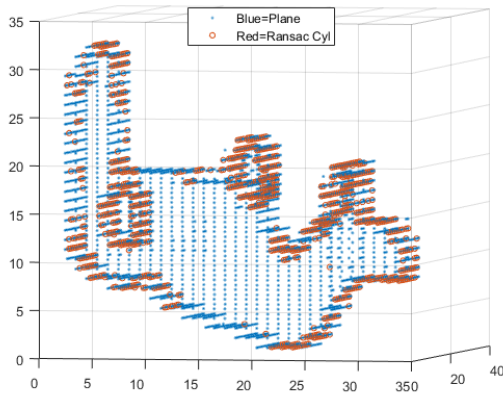


Figure 104. MLESAC with imposed axis $(1,0,0)$ applied on Latching Lever.

1.4 Handle

This component (Figure 105), made in Polycarbonate with addition of 12% of fibers of other polymers, is used for the users' control of the switch. The role of the handle is the interface with the user, due to this, the choice of a material like Polycarbonate can solve issues connected to the finishing and to the mechanical strength, (this piece is subject to little “crashes” against the wall of cover every time the lifesaver breaker changes condition).



Figure 105. Handle (Code: 04237711 Handle RCCB MIRAD).

The scope of this case study is to add information about acquisition set-up (it is an example of multicavities acquisition), and, mostly, about the measurement stage and data.

The component was available in eight samples one for each of the eight cavities of a die (Figure 106). For the acquisition set-up, the necessary STL nominal model and data reported in Table 21 were submitted as input to the developed GUI.

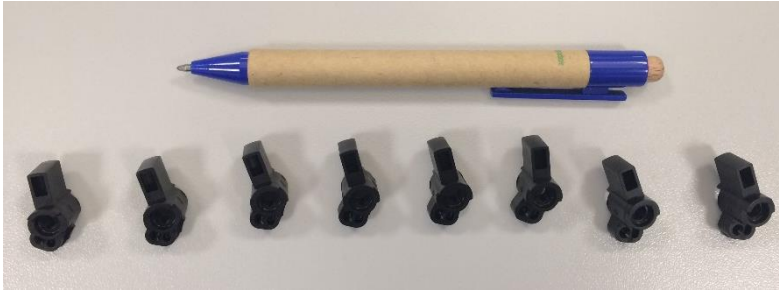


Figure 106. The 8 samples of Handle compared to a pen.

Number of cavities and clouds	8
Dimensions	16.5 x 22.5 x 15 mm
Number of views (suggested/possible)	3 of 4
Elapsed time for acquisition set-up (GUI)	3'

Table 21. Characteristics and input data of the Handle for the acquisition set-up.

The algorithms provided as output 4 orientations (in order from the most stable and easy to acquire to the worse), and we selected the first three (Figures 107, 108, 109) leaving the one reported in Figure 110.

In addition, the developed algorithms, due to the multicavities condition, is able to calculate the positioning of each sample on the acquiring table (see, for example, Figure 111), maintaining the capability of output optimal paths in terms of time and acquired features.

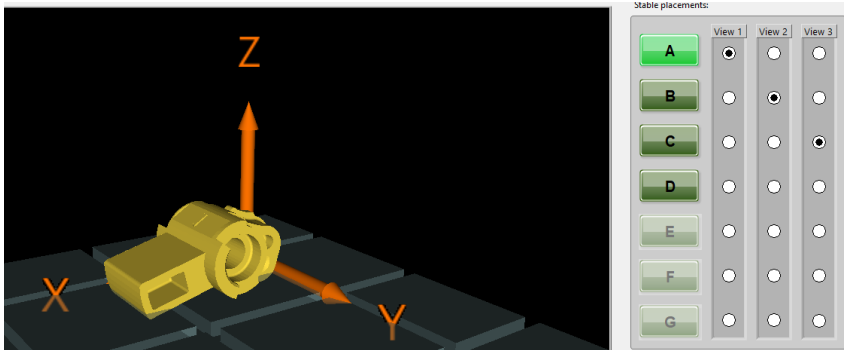


Figure 107. First selected orientation for Handle.

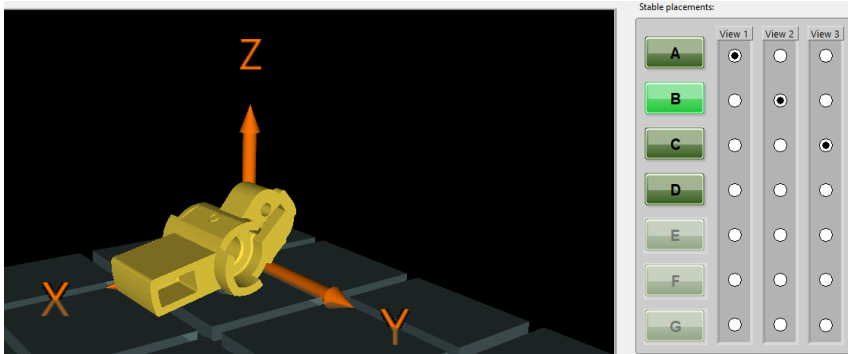


Figure 108. Second selected orientation for Handle.

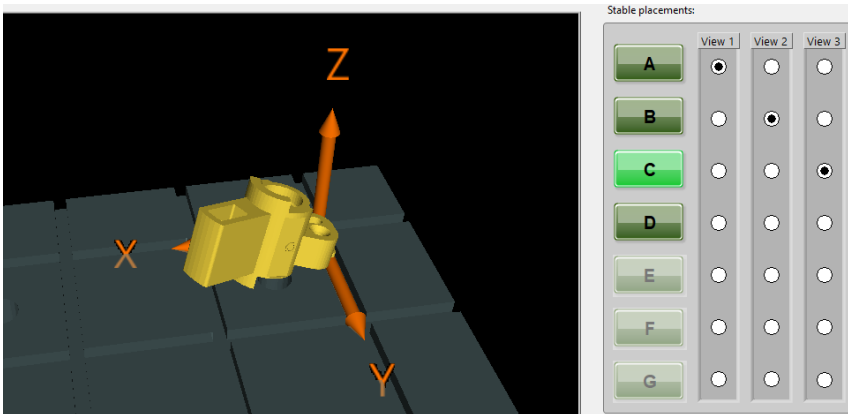


Figure 109. Third selected orientation for Handle.

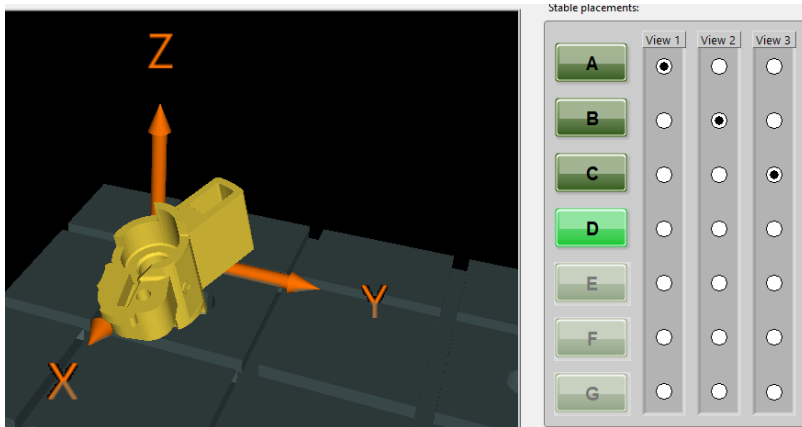


Figure 110. The unselected orientation given by the GUI for Handle.



Figure 111. The positioning of the eight samples of Handle, provided by the GUI.

As visible in Figure 111, due to the black colour of pieces, they were covered with mat spray (a white developer for porosity checks) to avoid reflection (as already done with the Johansson block, see section 3.1 of Chapter 5).

The obtained clouds were quite similar in terms of characteristics, so that we report just the elaboration made for the first cavity. After the registration and the recomposition of the partial clouds, the total cloud of

the considered cavity resulted to have 184782 points (each of other clouds has differences with it of few percentage points). In order to achieve a high level of resolution, we choose to divide the cloud through the usage of a 32x32x32 voxel structure (Figure 112) obtaining parameters reported in Table 22.

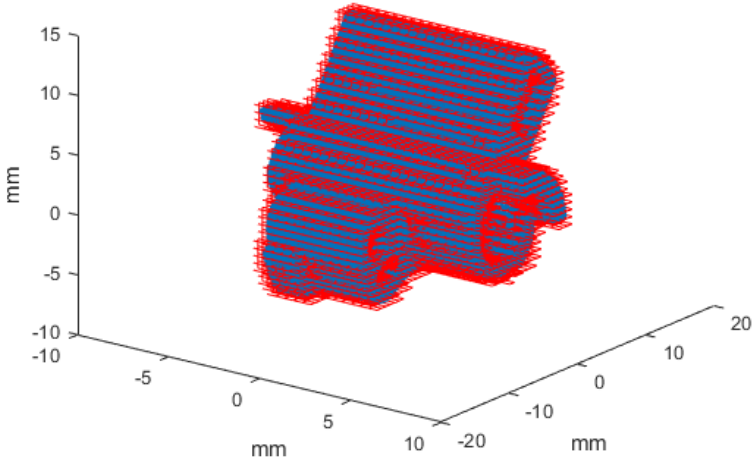


Figure 112. The obtained 32x32x32 voxel structure for Handle.

$k_x \times k_y \times k_z$	32x32x32
% of $V_{ijk} = 1$	13%
V_{ijk} length (mm)	0.49x0.65x0.62
%Planar $V_{ijk} = 0$ after thresholds	3%
Average No. of points per V_{ijk}	43
Clusters of plane orientation	10
%Curved $V_{ijk} = 0$ after thresholds	49%

Table 22. Data obtained through the segmentation procedure for Handle.

The occurrence histogram confirmed the goodness of voxel structure resolution (Figure 113), showing a flat occurrence for all the significant bins.

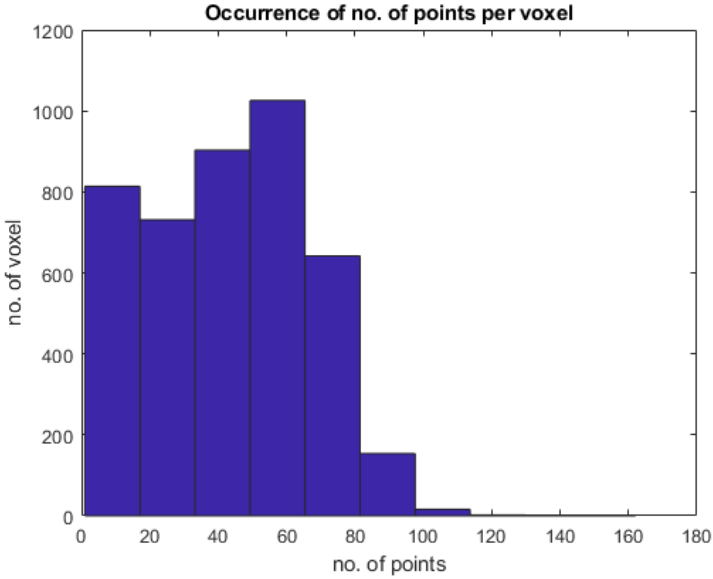


Figure 113. Occurrence of number of points per voxel with 32x32x32 structure for Handle.

The procedure allowed reaching a good level of planar clusterization, finding the majority of planar features (Figure 114(a)), also in details like the one reported in Figure 114(b).

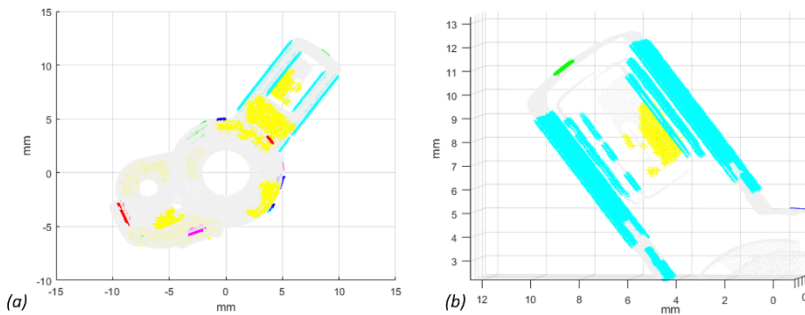


Figure 114. Planes orientation for the Handle: (a) the entire set with a 32x32x32 voxel structure; (b) a detail.

In this case MLESAC has been implemented with the imposed orientation (1, 0, 0), giving the results reported in Figure 115. The imposed orientation, confirming what explained previously, caused the high number of Curved $V_{ijk} = 0$, as reported in Table 22.

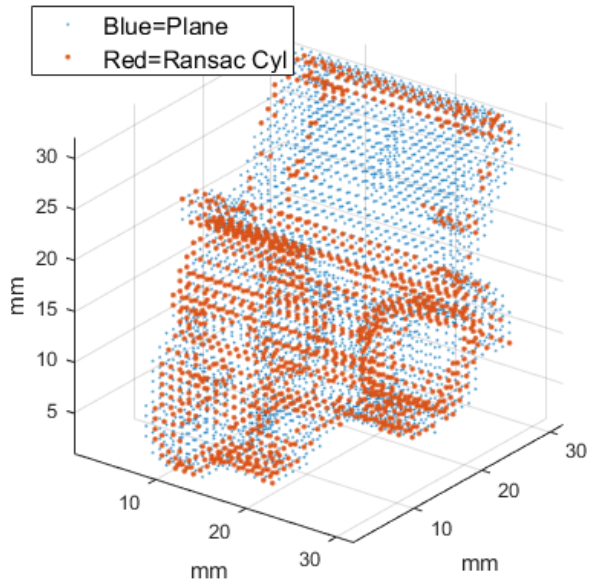


Figure 115. Partition of cylindrical voxel for Handle through MLESAC.

Conclusions

This work concerned with developing segmentation algorithms able to support the automation of plastic injection moulded part via Reverse Engineering (RE). Electromechanical components range from less than 10 mm up to 250 mm, so that die design asks for multicavity dies. They must be inspected in order to assess the goodness of the design, in terms of tolerances and absence of shape defects. This process is repetitive and a proper automation is appreciated to reduce errors and increase the robustness of the comparison.

RE via laser scanner on a CMM portal is suitable to approach this problem, thanks to an estimated accuracy of $3.9\ \mu\text{m}$ for the laser, and lower than $6\ \mu\text{m}$ for the portal. Usually, industrial applications related to inspection via RE are approached via commercial software that ask for cloud-CAD registration and measures via distance analysis. Automation is achieved via macros that replicate the comparison, without taking into account specific problems related to each part (alignment during acquisition, missed data, and so on).

This thesis presented a voxel-based segmentation technique, suitable to automatically recognise cluster of plane orientations and cylindrical surfaces for measurements according to an inspection protocol. The technique is derived from an octree subdivision, named Hierarchical Space Partitioning, which can be adaptive along x, y and z, selectively. Through these planes and cylinders are ready for the measure without the need of CAD model alignment nor mandatory surface reconstruction. Moreover, dense clouds may be analysed without filtering, since voxels substitute the tessellation, including more points without losing information. The core of the implementation is the voxel structure. For its definition, the most critical aspect is the selection of the number of final subdivisions. It means the selection of suitable k_L , k_M , k_N , to achieve the proper resolution to distinguish the surfaces that are interesting for the measures. In fact, each voxel may locally approximate the surface, through the points it has. Via threshold analysis, the local surface is

accepted or rejected as planar or cylindrical, than each of them is clustered via region-growing / hierarchical clustering, to find planes and cylinders. An iterative algorithm for automatic thresholding is here proposed to improve accuracy and robustness of the method. Thresholds for local planar voxels, namely the first bin of the variance histogram, has been studied, finding remarkable exception for axial symmetrical with low height/radius ratio (Flange for Aeronautical Applications). Nevertheless, the more stringent threshold can be also applied to the other case study with minor discrepancy (Din Rail Clip). In this case, small voxels approximate the large curvature wrongly, thus, some errors in the definition of planar voxels may occur. Making more stringent the L_2 orientation norm may release the problem.

Concerning surface recognition in this work, two algorithms were investigated to fit planes and cylinders: Levenberg- Marquardt using Kasa result as first-guess and a Ransac based algorithm (MLE SAC). LM(Kasa) shows good results despite the fact that asks for a preliminary knowledge of the cylinder axis directions. It can be solved by an Intrinsic Reference System, found through the voxel structure analysis or by the knowledge of the acquisition system. MLE SAC cannot overcome completely the problems of LM(Kasa), except in the case of small radius cylinders through points on a wide arc length. In fact, MLE SAC showed problems about finding large curvature cylinders through points on a small arc length, when no axis direction is given as first-guess. This makes the fit model highly scattered also among contiguous curved voxels, ruining the region growing – hierarchical clustering of large radius areas. Imposing a first-guess direction, many curved voxels are not fit (60%), but radius evaluation highly improves, and, obviously, computational time increases.

Application test-cases, taken from industrial assemblies were carried out to evaluate the technique and, when possible the associated inspection workflow. In particular, the plane clusterization always succeeded founding the most relevant planes in any cases. Curved voxels include both cylindrical and edge surfaces, nevertheless, MLE SAC may, with some scatter, evaluate radius of both if small voxel lengths is used along

small corner radii. Originally developed algorithms for threshold analysis and region growing / hierarchical partitioning work suitable for both planar and cylindrical voxels. Clusterization of 10^6 points on $200 \times 100 \times 50$ mm of volume can be analysed in less than 30 minutes with a laptop pc Intel CORE i3.

Considerations about the whole inspection workflow were also made. In particular, a PDM oriented to multicavities has been proposed and three methods to approach the plane tolerance inspection have been set. Also, an automatic acquisition path has been developed, to manage multicavities and speed up the inspection, assuring common and optimal scan conditions.

To evaluate possible benefits of the workflow, not only in terms of inspection speed, some considerations and preliminary tests about errors have been made, using virtual and real gauge a Johansson block. Virtual block reveals good agreement between measured planes distance and nominal, with errors less than 0.001 mm. It is a preliminary confirmation that, with adequate number of points per voxels, surface clusterization without fitting may not introduce errors in the post-processing. Concerning the real acquisition of the block, Palmer measurements may be not comparable with the RE elaboration, not being able to capture mat spray thickness, or shape deviations due to wear and bad storing conditions of the block.

The presented applications and preliminary validations have given encouraging results, in terms of soundness and general applicability of the proposed methodology. They are enforced by their industrial adoption to speed up the process. Nevertheless, further investigations will be necessary, mainly to validate statistical coherence of replicated measures in the respect of the proposed solutions for plane tolerance analysis, that aim to overcome distance analysis from CAD model. Doing so, the inspection process will be linked to design only by data extraction of the tolerance prescription, reducing the chain error of the measurement.

Acknowledgements

This work was supported by the Quality Control Department of ABB Sace S.p.A., site of Santa Palomba (Rome), Italy. The project has been developed into a wide “Accordo Quadro” submitted by the company and the Department of Mechanical and Aeronautical Engineering (DIMA) of Sapienza University of Rome.

I would like therefore to thank Alessio Trifirò (also for co-advising this thesis), Luca Tito, David Boron, Mauro Pappalardo, Giovanni Paris, Stefano Petriaggi, Carlo Catanzaro, Roberto Spallotta for all the support given to me and the proven professionalism.

I would also like to thank Prof. Giovanni B. Broggiato for the implementation of the algorithms for acquisitions optimisation, explained in Section 3 of Chapter 2, and for all the support during the entire duration of the project.

List of Figures

Figure 1. Example of Delaunay triangles (Peterson, 2017).....	9
Figure 2. An example of an injection moulding machine (a), and its main components (b), (c).....	14
Figure 3. Different typologies of material adduction solutions.....	16
Figure 4. Example of burr.	17
Figure 5. Example of ejector pin marks.	18
Figure 6. Different mechanical structures of CMMs.....	26
Figure 7. Examples of components with dimensional reference (cm). .	30
Figure 8. The laser scanner in use during the measurement of a series of components.	31
Figure 9. Nikon LC15Dx Laser Scanner.....	32
Figure 10. Dimensions and FOV of the Nikon LC15Dx (Nikon Metrology, 2017).	32
Figure 11. CMM 3Coord Hera 12.09.07.....	33
Figure 12. Scheme of the CMM 3Coord Hera 12.09.07.	34
Figure 13. Scheme of principal elements of a moving bridge CMM. ...	34
Figure 14. The developed GUI for acquisition set-up.....	37
Figure 15. Example of the three optimal positions for a component.	38
Figure 16. (a) Example of creation of paths (model of the component in yellow, acquirable zones in pointed black); (b) particular (different positions of the laser blade in cyan).....	39
Figure 17. Example of voxel structure (red lines) encompassing a clouds of points.	43
Figure 18. Structure of pixels: logical scheme for the assignment of V_{ij}	45
Figure 19. Effect related to a reduction of the resolution, $r=s=t$	46
Figure 20. Plane partition for a box-shaped component with small wall thickness ($r=s=t=5$, $L=M=N=32$).....	46
Figure 21. Plane partition: (a) occurrence histogram of the variance computed from the voxel's best-fit planes; (b) in green planar surfaces associated to the first bin of the histogram in Figure 20(a), points in blue example of small radii or non-planar region recognition.	48
Figure 22. Iterative evaluation of variance threshold for planar voxels. Highlighted areas are discharged from planar segmentation through the derivative of the minimum bin value.....	49

Figure 23. Comparison among Kasa, LM(Kasa), Taubin fitting a circular distribution of points, $C=[1;2]$, $R=3\text{mm}$, $\delta=0.05\text{mm}$, with small arc length.....	51
Figure 24. Comparison among Kasa, LM(Kasa), Taubin fitting a circular distribution of points, $C=[1;2]$, $R=3\text{mm}$, $\delta=0.01\text{mm}$, with small arc length.....	51
Figure 25. Comparison among Kasa, LM(Kasa), Taubin fitting a circular distribution of points, $C=[1;2]$, $R=3\text{mm}$, $\delta=0.05\text{mm}$, with large arc length.....	52
Figure 26. Comparison among Kasa, LM(Kasa), Taubin fitting a circular distribution of points, $C=[1;2]$, $R=15\text{mm}$, $\delta=0.05\text{mm}$	52
Figure 27. Point cloud #1: distance analysis from the cylinder fit made by CatiaV5R12.....	55
Figure 28. Point cloud #2: distance analysis from the cylinder fit made by CatiaV5R12.....	55
Figure 29. Point Cloud #1 - Sensitivity Analysis according to the input parameter related to the maximum distance of the inliers from the evaluated surface (MaxDistance). Upper plot: Mean Error of the fit; Middle plot: Radius of the fitting; Lower plot: percentage of inliers in the respect of the total number of points.	57
Figure 30. Point Cloud #2 - Sensitivity Analysis according to the input parameter related to the maximum distance of the inliers from the evaluated surface (MaxDistance). Upper plot: Mean Error of the fit; Middle plot: Radius of the fitting; Lower plot: percentage percentage of inliers in the respect of the total number of points.	59
Figure 31. (a) Voxel detection with small radii or non-planar region (blue points); (b) Clusters found for planes perpendicular to the reference axes – (blue for x axis; magenta for y axis; green for z axis).	62
Figure 32. Logical workflow of the proposed approach and applied methodologies (on the right) using LM(Kasa) algorithm.	63
Figure 33. Logical workflow of the proposed approach and applied methodologies (on the right) using Ransac-based algorithm.	64
Figure 34. Voxel structure obtained after the parallelisation in two processors; the upper part has been assigned to the first worker, the bottom to the other.	67
Figure 35. Din Rail Clip: Frequency of voxels (in %) with a specific No. of points.	74

Figure 36. Din Rail Clip: 16x16x16 (a) Local surface segmentation (blue points are planar, mustard are curved); (b) Voxel Structure..	75
Figure 37. Din Rail Clip: 32x16x8 (a) Local surface segmentation (blue points are planar, mustard are curved); (b) Voxel Structure..	76
Figure 38. Din Rail Clip: comparison among 16x16x16 and 32x32x32 - (a) cosines of the recognised directions; (b) cosines weighted with % of correspondent voxels.....	78
Figure 39. Din Rail Clip: 32x32x32 (a) Voxel Structure; (b) Detail of the local surface segmentation (red marks are planar, cyan are curved).....	79
Figure 40. Din Rail Clip: 32x16x8 final clusters.	80
Figure 41. Flange for Aeronautical Application: Voxel structure with 16x16x16 resolution.	82
Figure 42. Flange for Aeronautical Application: Voxel structure with 32x32x8 resolution.	82
Figure 43. Flange for Aeronautical Application: Voxel structure with 32x32x16 resolution.	83
Figure 44. Flange for Aeronautical Application: Voxel structure with 64x64x16 resolution.	83
Figure 45. Flange for Aeronautical Application: Frequency of voxels (in %) with a specific No. of points.....	84
Figure 46. Flange for Aeronautical Application - voxel structure 32x32x16. Points in planar (red) and curved (grey) voxels..	85
Figure 47. Voxel standard deviation in a transversal section of the acquisition.....	86
Figure 48. Flange for Aeronautical Application - voxel structure 32x32x16. Final clusters aggregated from the planar direction found, according to the change of the increasing number of first bin for threshold analysis	87
Figure 49. Din Rail Clip: Voxel Structure 32x32x32 - Sensitivity analysis on the normal dot product threshold: (a) no. of clusters normal to reference axis; (b) no. of clusters normal to reference axis, excluding clusters made of less than 4 voxels	89
Figure 50. Plane recognition with $L_2=0.0001$ for Flange.....	90
Figure 51. Plane recognition with $L_2=0.001$ for Flange.....	90
Figure 52. Transferability of the thresholds: (a) first-guess no. bin = 20, $L_2 = 0.0001$; (b) first guess no. bin = 100, $L_2 =0.0001$; (c) first guess no. bin = 100, $L_2 =0.0001$	91
Figure 53. The found IRS for Din Rail Clip.....	92

Figure 54. The found IRS for Flange (the x-axis of the recognised IRS is the central axis of the flange). 93

Figure 55. Flange for Aeronautical Application: LM(Kasa) evaluation of the radii associated to non-planar voxels. 94

Figure 56. Flange for Aeronautical Application: particular of the blueprint of the component..... 94

Figure 57. Validation of the surface reconstruction via CATIA V5. 95

Figure 58. in red, points in voxels that fails the MLESAC fit due to less than 6 points in the voxels; (Voxel structure 32x32x16, Max Distance=0.01 mm). 96

Figure 59. Final voxel partition in Cylindrical and Planar local surfaces (Voxel structure 32x32x16, Max Distance=0.01 mm). 97

Figure 60. Frequency distribution of the occurrence of the mean of the distance errors from the fit radius. 98

Figure 61. Fit radius distribution: (a) in section 3 of the 16 voxel subdivision along the z-axis; (b) in section 2 (on the left) and section 8 (on the right). 99

Figure 62. Frequency distribution of the occurrence of the mean of the distance errors from the fit radius – axis direction imposed in MLESAC. 100

Figure 63. Fit radius distribution in section 2 (on the left) and section 3 (on the right). 100

Figure 64. Steps of common workflow related to CMM acquisitions. 104

Figure 65. Workflow based on part-type recognition..... 106

Figure 66. Example of automatic part type recognition: logical workflow and example of binarisation and boundary tracing of four plane sections..... 107

Figure 67. Product-process integrated optimization of injection moulded parts: strategy (on the upper part); PIDM steps to support it (on the lower part). 109

Figure 68. ISO GPS standard matrix model, (ISO14638, 2015). 111

Figure 69. The independence principle. 111

Figure 70. Measurement by discrete points..... 112

Figure 71. Graphical visualisation of maximum measures done through three different methods. 113

Figure 72. Example of measurement GUI for Din Rail Clip. In the red box, for planarity evaluation, distances histogram from best-fit planes are reported; in the yellow box, the coupled measures with the three proposed methods (minimum, average and maximum values for each). 115

Figure 73. Example of the measurement GUI for Latching Lever.....	115
Figure 74. Johansson block point cloud.	118
Figure 75. Example of an electromechanical assembly produced by ABB (with and without the cover).	121
Figure 76. Cover (Code: 04237696 Cover 2P 35 MMQ RCCB MIRAD).	123
Figure 77. First selected orientation for Cover.....	124
Figure 78. Second selected orientation for Cover.	125
Figure 79. Third selected orientation for Cover.	125
Figure 80. The unselected orientation given by the GUI for Cover. ...	126
Figure 81. 32x32x32 Voxel structure superimposed on Cover point cloud.	127
Figure 82. Occurrence of number of points per voxel for Cover with the superimposed 32x32x32 structure.	128
Figure 83. Plane direction sets for Cover.	128
Figure 84. The application of MLESAC in the divided cloud of Cover.	129
Figure 85. Test Button (Code: 04237756 Test Button RCBO MIRAD).	130
Figure 86. First selected orientation for Test Button.....	131
Figure 87. Second selected orientation for Test Button.	132
Figure 88. Third selected orientation for Test Button.	132
Figure 89. The four unselected orientations given by the GUI for Test Button.	133
Figure 90. The obtained point cloud for the considered sample of Test Button.	134
Figure 91. Occurrences of number of points per voxel: (a) 32x32x32; (b) 32x64x16.	135
Figure 92. Plane orientations; 32x32x32 voxels (on the left) and 32x64x16 (on the right).	135
Figure 93. Example of nominal measure.....	136
Figure 94. 32x32x32 Cylindrical voxels through MLESAC: (a) partition; (b) Radius evaluation.	136
Figure 95. Latching Lever (Code: 04235556 Latching Lever RCBO).	137
Figure 96. First selected orientation for Latching Lever.....	138
Figure 97. Second selected orientation for Latching Lever.	138
Figure 98. Third selected orientation for Latching Lever	139
Figure 99. The four unselected orientations given by the GUI for Latching Lever.	139

Figure 100. Latching Lever: (a) 32x32x32 voxel structure; (b) local surface recognition planar features in green, curved features in blue.....	141
Figure 101. Lateral view of the Latching Lever with its IRS.....	142
Figure 102. Curved voxels recognized in the Lever before cylinder recognition.	142
Figure 103. (a) Set of points of the clusters found in the X-direction; (b) Cluster of R=1 mm cylinders.	144
Figure 104. MLESAC with imposed axis (1,0,0) applied on Latching Lever.	144
Figure 105. Handle (Code: 04237711 Handle RCCB MIRAD).....	145
Figure 106. The 8 samples of Handle compared to a pen.	146
Figure 107. First selected orientation for Handle.....	147
Figure 108. Second selected orientation for Handle.....	147
Figure 109. Third selected orientation for Handle.	147
Figure 110. The unselected orientation given by the GUI for Handle.	148
Figure 111. The positioning of the eight samples of Handle, provided by the GUI.....	148
Figure 112. The obtained 32x32x32 voxel structure for Handle.....	149
Figure 113. Occurrence of number of points per voxel with 32x32x32 structure for Handle.	150
Figure 114. Planes orientation for the Handle: (a) the entire set with a 32x32x32 voxel structure; (b) a detail.	150
Figure 115. Partition of cylindrical voxel for Handle through MLESAC.	151

List of Tables

Table 1. List of non-contact acquisition methods and general comparison regarding some properties (sensibility, speed, robustness, relation between performances and costs), (Broggiato, et al., 2002).....	24
Table 2. Fitting parameters found by CatiaV5R12.	54
Table 3. Time savings with parallelisation for the generation of the voxel structure.	67
Table 4. Test cases used for procedure development.	71
Table 5. Din Rail Clip: Voxel structure characteristics in function of the zoom ratios (r, s, t).	73
Table 6. Din Rail Clip: number of planar directions after segmentation in function of the zoom ratios (r, s, t).....	77
Table 7. Din Rail Clip: Final directions recognised via hierarchical clustering and region-growing algorithms ($L_2= 0.01$)	77
Table 8. Flange for Aeronautical Application: Voxel structure characteristics in function of the zoom ratios (r, s, t); data are referred to a 90° section of the whole cloud.	81
Table 9. Percentage of curved voxels that fail to find MLESAC solution – Maximum distance set to 0.1 mm, confidence=99%.....	96
Table 10. Sources of possible errors.	116
Table 11. Computation time of virtual Johansson block for different number of fixed voxels.	117
Table 12. Obtained thickness values (in mm) for the three methods. .	119
Table 13. Used case studies.....	122
Table 14. Characteristics and input data of the Cover for the acquisition set up.	124
Table 15. Data obtained through the segmentation procedure for Cover.	127
Table 16. Characteristics and input data of the Test Button for the acquisition set up.	131
Table 17. Comparison between the two considered voxel structures for Test Button.....	134
Table 18. Characteristics and input data of the Latching Lever for the acquisition set up.	138
Table 19. Data obtained through the segmentation procedure for Latching Lever.	140

Table 20. Automatic selection of variance threshold for finding cylindrical voxels. 143

Table 21. Characteristics and input data of the Handle for the acquisition set-up. 146

Table 22. Data obtained through the segmentation procedure for Handle. 149

References

- Aijazi, A. K., Checchin, P. & Trassoudaine, L., 2013. Segmentation Based Classification of 3D Urban Point Clouds: A Super-Voxel Based Approach with Evaluation. *Remote Sensor*, Volume 5, pp. 1624-1650.
- Akselrod-Ballin, A. et al., 2006. *An integrated segmentation and classification approach applied to multiple sclerosis analysis*. s.l., s.n., pp. 1122-1129.
- Alemán, J. et al., 2007. Definitions of terms relating to the structure and processing of sols, gels, networks, and inorganic-organic hybrid materials (IUPAC Recommendations 2007). *Pure and Applied Chemistry*, 79(10), pp. 1801-1829.
- Ali, F., Chowdary, B. V. & Imbert, C. A., 2009. Part design and evaluation through reverse engineering approach. *International Journal of Agile Manufacturing*, 11(1), pp. 73-82.
- Almasi, G. S. & Gottlieb, A., 1989. *Highly Parallel Computing*. Redwood City, CA, USA: Benjamin-Cummings Publishing Co., Inc..
- Al-Sharadqah, A. & Chernov, N., 2009. Error analysis for circle fitting algorithms. *Electronic Journal of Statistics*. 3, 886-- 911., Volume 3, pp. 886-911.
- Ameri, F. & Dutta, D., 2005. Product Lifecycle Management: Closing the Knowledge Loops. *Computer-Aided Design and Applications*, 2(5), pp. 577-590.
- Amodio, D. et al., 2001. *Automated defect detection on stamped panels by strain analysis and shape assessment*. Ancona (Italy), s.n.
- Anwer, N. & Mathieu, L., 2016. From reverse engineering to shape engineering in mechanical design. *CIRP Annals*, 65(1), pp. 165-168.
- Attene, M., Falcidieno, B. & Spagnuolo, M., 2006. Hierarchical mesh segmentation based on fitting primitives. *The Visual Computer*, 22(3), p. 181–193.
- Attene, M. et al., 2006b. *Mesh Segmentation - A Comparative Study*. Washington, DC, USA, IEEE Computer Society.

- Audfray, N., Mehdi-Souzani, C. & Lartigue, C., 2013. A Novel Approach for 3D Part Inspection Using Laser-plane Sensors. *Procedia CIRP*, Volume 10, pp. 23-29.
- Azernikov, S., Miropolsky, A. & Fischer, A., 2003. *Surface reconstruction of freeform objects based on multiresolution volumetric method*. New York, NY, USA, ACM, pp. 115-126.
- Babahajiani, P., Fan, L., Kamarainen, J. & Gabbouj, M., 2016. *Automated super-voxel based features classification of urban environments by integrating 3D point cloud and image content*. s.l., s.n., pp. 372-377.
- Baeurle, S. A., Hotta, A. & Gusev, A. A., 2006. On the glassy state of multiphase and pure polymer materials. *Polymer*, 47(17), pp. 6243-6253.
- Barbero, B. R., 2009. The recovery of design intent in reverse engineering problems. *Computers & Industrial Engineering*, Volume 56, pp. 1265-1275.
- Barbero, B. R. & Ureta, E. S., 2011. Comparative study of different digitization techniques and their accuracy. *CAD Computer Aided Design*, 43(2), pp. 188-206.
- Barone, S., Paoli, A. & Rationale, A. V., 2012. Three-dimensional point cloud alignment detecting fiducial markers by structured light stereo imaging. *Machine Vision and Applications*, 23(2), pp. 217-229.
- Beiter, K. A. & Ishii, K., 1997. *Incorporating dimensional requirements into material selection and design of injection molded parts*. s.l., s.n., p. 3295-3299.
- Benko, P., Martin, R. R. & Varady, T., 2001. Algorithms for reverse engineering boundary representation models. *Computer-Aided Design*, 33(11), pp. 839-851.
- Benko, P. & Varady, T., 2004. Segmentation methods for smooth point regions of conventional engineering objects. *Computer-Aided Design*, Volume 36, pp. 511-523.
- Bici, M., Broggiato, G. B., Campana, F. & Dughiero, A., 2017. Computer Aided Inspection Procedures to Support Smart Manufacturing

- of Injection Moulded Components. *Procedia Manufacturing*, Volume 11, pp. 1184-1192.
- Bici, M., Campana, F., Petriaggi, S. & Tito, L., 2014. Study of a Point Cloud Segmentation with Part Type Recognition for Tolerance Inspection of Plastic Components via Reverse Engineering. *Computer-Aided Design and Application*, 11(6), pp. 640-648.
- Bici, M., Campana, F. & Trifirò, A., 2016. Automatic post-processing for tolerance inspection of digitized parts made by injection moulding. *Computer-Aided Design and Applications*, 13(6), pp. 835-844.
- Bici, M., Campana, F., Trifirò, A. & Testani, C., 2014b. *Development of automatic tolerance inspection through Reverse Engineering*. Benevento, Italy, s.n., pp. 107-112.
- Bi, Z. M. & Wang, L., 2010. Advances in 3D data acquisition and processing for industrial applications. *Robotics and Computer-Integrated Manufacturing*, 26(5), pp. 403-413.
- Bradley, C. & Currie, B., 2005. Advances in the Field of Reverse Engineering. *Computer-Aided Design and Applications*, 2(5), pp. 697-706.
- Broggiato, G. B., Campana, F. & Gerbino, S., 2001. *Shape deviation analysis on sheet metal parts through reverse engineering techniques*. Rimini, Italy, s.n.
- Broggiato, G. B., Campana, F., Gerbino, S. & Martorelli, M., 2002. *Confronto tra diverse tecniche di digitalizzazione delle forme per il reverse engineering*. Santander, Spain, XIV Congreso Internacional de Ingeniería Gráfica.
- Buonamici, F., Carfagni, M. & Volpe, Y., 2017. Recent strategies for 3D reconstruction using Reverse Engineering: a bird's eye view. In: B. Eynard, et al. a cura di *Advances on Mechanics, Design Engineering and Manufacturing : Proceedings of the International Joint Conference on Mechanics, Design Engineering & Advanced Manufacturing (JCM 2016)*. Catania, Italy: Springer International Publishing, pp. 841-850.
- Busick, D. R., Beiter, K. A. & Ishii, K., 1994. Design for injection molding: Using process simulation to assess tolerance

- feasibility. *Computers in Engineering, Proceedings of the International Conference and Exhibit*, 1(-), pp. 113-120.
- Campana, F. & Germani, M., 2008. Datum identification for tolerance control on dense clouds of points. *Computer-Aided design and Applications*, 5(1-4), pp. 209-219.
- Campbell, R. J. & Flynn, P. J., 2001. A Survey Of Free-Form Object Representation and Recognition Techniques. *Computer Vision and Image Understanding*, 81(2), pp. 166-210.
- Cao, H. & Folan, P., 2012. Product life cycle: the evolution of a paradigm and literature review from 1950–2009. *Production Planning & Control*, 23(8), pp. 641-662.
- Carbone, V. et al., 2001. Combination of a vision system and a coordinate measuring machine for the reverse engineering of freeform surfaces. *International Journal of Advanced Manufacturing Technology*, 17(4), pp. 263-271.
- Che, C. & Ni, J., 2000. A ball-target-based extrinsic calibration technique for high-accuracy 3-D metrology using off-the-shelf laser-stripe sensors. *Precision Engineering*, 24(3), pp. 210-219.
- Courtial, A. & Vezzetti, E., 2008. New 3d segmentation approach for reverse engineering selective sampling acquisition. *The International Journal of Advanced Manufacturing Technology*, 35(9), pp. 900-907.
- Creehan, K. D. & Bidanda, B., 2006. Reverse engineering: a review & evaluation of non-contact based systems. In: *Rapid prototyping: theory and practice*. s.l.:Springer US, pp. 87-106.
- Cuesta, E. et al., 2009. Influence of roughness on surface scanning by means of a laser stripe system. *International Journal of Advanced Manufacturing Technology*, 43(11-12), pp. 1157-1166.
- Curless, B. & Levoy, M., 1996. *Volumetric method for building complex models from range images*. s.l., s.n., pp. 303-312.
- Curtis, S. K., Harston, S. P. & Mattson, C. A., 2011. The fundamentals of barriers to reverse engineering and their implementation into mechanical components. *Research in Engineering Design*, 22(4), pp. 245-261.

- Curtis, S. K., Harston, S. P. & Mattson, C. A., 2009. *A Generic Formulaic Characterization of the Time to Reverse Engineer the Tolerances of a Product*. Lake Buena Vista, Florida, USA, ASME, pp. 275-285.
- Custom Part Net, 2017. *Custom Part Net*. [Online] Available at: <http://www.custompartnet.com>
- Das, A., Franciosa, P., Pesce, A. & Gerbino, S., 2017. Parametric effect analysis of free-form shape error during sheet metal forming. *International Journal of Engineering Science and Technology*, 9(09S), pp. 117-124.
- Davis, J. et al., 2015. Smart Manufacturing. *Annual Review of Chemical and Biomolecular Engineering*, 6(1), pp. 141-160.
- De, S. K., 1996. *Rubber Technologist's Handbook*. First Edition a cura di s.l.:Smithers Rapra Press.
- Dey, T. K., Giesen, J. & Hudson, J., 2001. *Decimating samples for mesh simplification*. Waterloo, Canada, s.n., pp. 85-88.
- Di Angelo, L. & Di Stefano, P., 2014. A computational Method for Bilateral Symmetry Recognition in Asymmetrically Scanned Human Faces. *Computer-Aided Design and Applications*, 11(3), pp. 275-283.
- Di Angelo, L. & Di Stefano, P., 2015. Geometric segmentation of 3D scanned surfaces. *Computer Aided Design*, Volume 62, pp. 44-56.
- Di Angelo, L., Di Stefano, P. & Morabito, A. E., 2012. The RGM data structure: a nominal interpretation of an acquired high point density model for automatic tolerance inspection. *International Journal of Production Research*, 50(12), pp. 3416-3433.
- Di Angelo, L., Di Stefano, P. & Morabito, A. E., 2011. Automatic evaluation of form errors in high-density acquired surfaces. *International Journal of Production Research*, 49(7), pp. 2061-2082.
- Di Angelo, L., Di Stefano, P. & Morabito, A. E., 2013. Recognition of intrinsic quality properties for automatic geometric inspection. *Int. J. on Inter. Des. and Manufact.*, 7(4), pp. 203-215.

- Di Angelo, L., Di Stefano, P. & Morabito, A. E., 2017. Product model for Dimensioning, Tolerancing and Inspection. In: B. Eynard, et al. a cura di *Advances on Mechanics, Design Engineering and Manufacturing: Proceedings of the International Joint Conference on Mechanics, Design Engineering & Advanced Manufacturing (JCM 2016)*. Catania, Italy: Springer International Publishing, pp. 1033-1040.
- Di Angelo, L., Di Stefano, P. & Spezzaneve, A., 2013. A method for 3D detection of symmetry line in asymmetric postures. *Computer Methods in Biomechanics and Biomedical Engineering*, 16(11), pp. 1213-1220.
- Di Stefano, P., Bianconi, F. & Di Angelo, L., 2004. An approach for feature semantics recognition in geometric models. *Computer-Aided Design*, 36(10), pp. 993-1009.
- Ding, L.-j., Dai, S.-g. & Mu, P.-a., 2016. CAD-Based Path Planning for 3D Laser Scanning of Complex Surface. *Procedia Computer Science*, 92(Supplement C), pp. 526-535.
- Dutailly, B. et al., 2009. *3D surface reconstruction using HMM algorithm*. s.l., s.n., pp. 2505-2508.
- Fasbinder, D. J., 2010. Digital dentistry: innovation for restorative treatment. *Compendium of continuing education in dentistry (Jamesburg, N.J. : 1995)*, 31(4), pp. 2-11.
- Feng, H.-Y., Liu, Y. & Xi, F., 2001. Analysis of digitizing errors of a laser scanning system. *Precision Engineering*, 25(3), pp. 185-191.
- Fudos, I., 2006. CAD/CAM Methods for Reverse Engineering: A Case Study of Re-engineering Jewelry. *Computer-Aided Design and Applications*, 3(6), pp. 683-700.
- Gabbia, A., 2016b. *PMI: Product Manufacturing Information*. Brescia, Italy, CMM Club, pp. 16-19.
- Gabbia, A., 2016. *ISO 14405-1:Dimensioni lineari*. Brescia, Italy, CMM Club, pp. 2-7.
- Gagnon, H., Soucy, M., Bergevin, R. & Laurendeau, D., 1994. *Registration of multiple range views for automatic 3-D model building*. s.l., s.n., pp. 581-586.

- Gao, J., Gindy, N. & Chen, X., 2006. An automated GD&T inspection system based on non-contact 3D digitization. *International Journal of Production Research*, 44(1), pp. 117-134.
- Genta, G., Minetola, P. & Barbato, G., 2016. Calibration procedure for a laser triangulation scanner with uncertainty evaluation. *Optics and Lasers in Engineering*, Volume 86, pp. 11-19.
- Germani, M., Mandorli, F., Mengoni, M. & Raffaelli, R., 2010. CAD-based environment to bridge the gap between product design and tolerance control. *Precision Engineering*, 34(1), pp. 7-15.
- Harrington, H. J., 1991. *Business process improvement: the breakthrough strategy for total quality, productivity, and competitiveness*. s.l.:McGraw-Hill Professional.
- Harston, S. P. & Mattson, C. A., 2010. *Metrics for evaluating the barrier and time to reverse engineer a product*. s.l., s.n., pp. 0410091-0410099.
- Hsiao, S. W. & Chuang, J. C., 2003. A reverse engineering based approach for product form design. *Des. Stud.*, 24(2), pp. 155-171.
- Huang, M. C. & Tai, C. C., 2000. The pre-processing of data points for curve fitting in reverse engineering. *The International Journal of Advanced Manufacturing Technology*, Volume 16, p. 635–642.
- Huang, M. C. & Tai, C. C., 2001. Effective factors in the warpage problem of an injection-molded part with a thin shell feature. *Journal of Materials Processing Technology*, 110(4), pp. 1-9.
- Ingle, K. A., 1994. *Reverse engineering*. New York, NY: McGraw-Hill.
- ISO10360-2, 2009. *Geometrical product specifications (GPS) -- Acceptance and reverification tests for coordinate measuring machines (CMM) -- Part 2: CMMs used for measuring linear dimensions*. s.l.:s.n.
- ISO14405-1, 2016. *Geometrical product specifications (GPS) -- Dimensional tolerancing -- Part 1: Linear sizes*. s.l.:s.n.

- ISO14405-2, 2011. *Geometrical product specifications (GPS) -- Dimensional tolerancing -- Part 2: Dimensions other than linear sizes*. s.l.:s.n.
- ISO14638, 2015. *Geometrical product specifications (GPS) -- Matrix model*. s.l.:s.n.
- ISO16792, 2015. *Technical product documentation -- Digital product definition data practices*. s.l.:s.n.
- ISO2011, 2004. *Geometrical product specifications (GPS). Geometrical tolerancing. Tolerances of form, orientation, location and run-out*. s.l.:s.n.
- Jamieson, R. & Hacker, H., 1995. Direct slicing of CAD models for rapid prototyping. *Rapid Prototyping Journal*, 1(2), pp. 4-12.
- Kaisarlis, G. J., 2012. A Systematic Approach for Geometrical and Dimensional Tolerancing in Reverse Engineering. In: InTech, a cura di *Reverse Engineering - Recent Advances and Applications*. s.l.:Dr. A.C. Telea (Ed.).
- Kasa, I., 1976. A circle fitting procedure and its error analysis. *IEEE Transactions on Instrumentation and Measurement*, IM-25(1), pp. 8-14.
- Keller, P., Hering-Bertram, M. & Hagen, H., 2007. Reverse engineering with subdivision surfaces. *Computing*, 79(2-4), pp. 119-129.
- Keller, P., Hering-Bertram, M. & Hagen, H., 2012. Surface Reconstruction from Unorganized 3D Point Clouds. In: InTech, a cura di *Reverse Engineering - Recent Advances and Applications*. s.l.:Dr. A.C. Telea (Ed.).
- Kim, G. B. et al., 2016. Three-Dimensional Printing: Basic Principles and Applications in Medicine and Radiology. *Korean Journal of Radiology*, 17(2), pp. 182-197.
- Knight, D. C., Mattson, C. A. & Adams, B. L., 2009. *Maximizing return on investment by constructing optimal barriers against competitors' market entry*. Palm Springs, AIAA.
- Knopf, G. & Al-Naji, R., 2001. Adaptive reconstruction of bone geometry from serial cross-section. *Artificial Intelligence in Engineering*, Volume 15, pp. 227-239.

- Lee, K. H. & Park, H., 2000. Automated inspection planning of free-form shape parts by laser scanning. *Robotics and Computer-Integrated Manufacturing*, 16(4), pp. 201-210.
- Lee, Y., Park, S., Jun, Y. & Choi, W. C., 2003. A robust approach to edge detection of scanned point data. *International Journal of Advanced Manufacturing Technology*, Volume 23, pp. 263-271.
- Li, Y. & Gu, P., 2004. Free-form surface inspection techniques state of the art review. *Computer-Aided Design*, 36(13), pp. 1395-1417.
- Mahmud, M. et al., 2011. 3D part inspection path planning of a laser scanner with control on the uncertainty. *Computer-Aided Design*, 43(4), pp. 345-355.
- Malloy, R. A., 1994. *Plastic part design for injection molding: an introduction*. Munich: Hanser.
- Martínez, S., Cuesta, E., Barreiro, J. & Álvarez, B., 2010. Analysis of laser scanning and strategies for dimensional and geometrical control. *International Journal of Advanced Manufacturing Technologies*, 46(5), pp. 621-629.
- Martínez, S., Cuesta, E., Barreiro, J. & Fernández, P., 2008. *Testing the capabilities of the three-spheres alignment method for laser triangulation sensors*. Tallinn, Estonia, s.n.
- Martorelli, M. & Ausiello, P., 2013. A novel approach for a complete 3D tooth reconstruction using only 3D crown data. *International Journal on Interactive Design and Manufacturing*, 7(2), pp. 125-133.
- Masuda, H. & Murakami, K., 2010. A study on smooth surface reconstruction from large-scale noisy point-clouds (1st Report) - Smoothing operators based on robust estimate. *Journal of the Japan Society for Precision Engineering*, 76(5), pp. 582-586.
- McNaught, A. D. & Wilkinson, A., 1997. *Compendium of Chemical Terminology*. Second Edition a cura di s.l.:Blackwell Science.
- Mehdi-Souzani, C., Thiébau, F. & Lartigue, C., 2006. Scan Planning Strategy for a General Digitized Surface. *Journal of Computing*

and *Information Science in Engineering (ASME)*, 6(4), pp. 331-339.

- Meneghello, R., Savio, E. & Concheri, G., 2003. *CAD based Measurements in Profile Tolerances Verification*. Aachen, Germany, s.n., pp. 483-486.
- Milroy, M. J., Weir, D. J., Bradley, C. & Vickers, G., 1996. Reverse engineering employing a 3D laser scanner: A case study. *International Journal of Advanced Manufacturing Technology*, 12(2), pp. 111-121.
- Moening, C. & Dodgson, N. A., 2003. *A new point cloud simplification algorithm*. Spain, s.n.
- Mowery, K. A., Blanchard, D. E., Smith, S. & Betts, T. A., 2004. Investigation of imposter perfumes using GC-MS. *Journal of Chemical Education*, 81(1), pp. 87-89.
- Musker, D. C., 1998. *Reverse engineering*. s.l., s.n.
- Nikon Metrology, 2017. *Nikon Metrology Products*. [Online] Available at: <https://www.nikonmetrology.com>
- Noble, J. A., 1995. From inspection to process understanding and monitoring: a view on computer vision in manufacturing. *Image and Vision Computing*, 13(3), pp. 197-214.
- Núñez Andrés, A., Buill Pozuelo, F., Regot Marimón, J. & de Mesa Gisbert, A., 2012. Generation of virtual models of cultural heritage. *Journal of Cultural Heritage*, 13(1), pp. 103-106.
- Ohly, A., 2009. Reverse engineering: unfair competition or catalyst for innovation?. In: *Patents and technological progress in a globalized world*. 6th edn a cura di s.l.:Springer-Verlag, p. 535-552.
- Okabe, A., Boots, B., Sugihara, K. & Sung, N. C., 1992. *Spatial Tessellations: Concepts and Applications of Voronoi Diagrams*. New York, USA: Wiley.
- Onuh, S., Bennett, N. & Baker, J., 2001. Rapid prototyping: Practical approach to enabling reverse engineering. *Proceedings of SPIE - The International Society for Optical Engineering*, Volume 4566, pp. 145-151.

- Orazi, L. & Tani, G., 2007. Geometrical inspection of designed and acquired surfaces. *The International Journal of Advanced Manufacturing Technology*, 34(1), pp. 149-155.
- Pal, D. K., Ravi, B., Bhargava, L. S. & Chandrasekhar, U., 2006. Computer aided reverse engineering for replacement parts: a case study. *Def. Sci. J.*, 56(2), pp. 225-238.
- Pauly, M., Gross, M. & Kobbelt, L. P., 2002. *Efficient simplification of point sampled surfaces*. Boston, US, s.n.
- Peterson, S., 2017. *Computing Constrained Delaunay Triangulations*. [Online]
Available at:
http://www.geom.uiuc.edu/~samuelp/del_project.html
- Piegl, L. A. & Tiller, W., 2001. Parameterization for surface fitting in reverse engineering. *Computer-Aided Design*, 33(8), pp. 593-603.
- Prieto, F., Lepage, R., Boulanger, P. & Redarce, T., 2003. A CAD-based 3D data acquisition strategy for inspection. *Machine Vision & Applications*, 15(2), pp. 76-91.
- Prieto, F., Redarce, T., Lepage, R. & Boulanger, P., 2002. An Automated Inspection System. *The International Journal of Advanced Manufacturing Technology*, 19(12), pp. 917-925.
- Rabbani, T., Dijkman, S., van den Heuvel, F. & Vosselman, F., 2007. An integrated approach for modelling and global registration of point clouds. *ISPRS Journal of Photogrammetry and Remote Sensing*, 61(6), pp. 355-370.
- Raja, V. & Fernandes, K. J., 2008. *Reverse engineering: an industrial perspective*. London: Springer-Verlag.
- Rekoff, M. G., 1985. On Reverse Engineering. *IEEE Transactions on Systems, Man and Cybernetics*, 15 (SMC)(2), pp. 244-252.
- Rockwood, A. P. & Winget, J., 1997. Three-dimensional object reconstruction from two-dimensional images. *Computer-Aided Design*, 29(4), pp. 279-285.

- Rodrigues Martins, F. A., García-Bermejo, J. G., Zalama Casanova, E. & Perán González, J. R., 2005. Automated 3D surface scanning based on CAD model. *Mechatronics*, 15(7), pp. 837-857.
- Sansoni, G. & Docchio, F., 2005. 3-D optical measurements in the field of cultural heritage: The case of the Vittoria Alata of Brescia. *IEEE Transactions on Instrumentation and Measurement*, 54(1), pp. 359-368.
- Sansoni, G., Trebeschi, M. & Docchio, F., 2009. State-of-the-art and applications of 3D imaging sensors in industry, cultural heritage, medicine, and criminal investigation. *Sensors*, 9(1), pp. 568-601.
- Savio, E., De Chiffre, L. & Schmitt, R., 2007. Metrology of freeform shaped parts. *CIRP Annals*, 56(2), pp. 810-835.
- Schnabel, R., Wahl, R. & Klein, R., 2007. Efficient RANSAC for point-cloud shape detection. *Computer Graphics Forum*, 26(2), pp. 214-226.
- Sequeira, V. et al., 1998. Automated 3D reconstruction of interiors with multiple scan-views. *Proceedings of SPIE - The International Society for Optical Engineering*, Volume 3641, pp. 106-117.
- Shamir, A., 2008. A survey on Mesh Segmentation Techniques. *Computer Graphics Forum*, 27(6), p. 1539-1556.
- Shen, J. & Yoon, D., 2012. Advances and prospects of digital metrology. *Computer-Aided Design and Applications*, 9(6), pp. 825-835.
- Song, M. et al., 2011. Analysis of injection molding defects for microfluidic chip. *Jixie Gongcheng Xuebao/Journal of Mechanical Engineering*, 47(6), pp. 33-38.
- Son, S., Park, H. & Lee, K. H., 2002. Automated laser scanning system for reverse engineering and inspection. *International Journal of Machine Tools and Manufacture*, 42(8), pp. 889-897.
- Stamati, V. & Fudos, I., 2005. A Feature-Based CAD Approach to Jewellery Re-engineering. *Computer-Aided Design and Applications*, 2(1-4), pp. 1-9.
- Stanek, M., Manas, D., Manas, M. & Javorik, J., 2011b. *Simulation of injection molding process*. s.l., s.n., pp. 231-234.

- Stanek, M., Manas, D., Manas, M. & Suba, O., 2011. Optimization of injection molding process. *International Journal of Mathematics and Computers in Simulation*, 5(5), pp. 413-421.
- Sun, X. et al., 2006. Injection molding defects and its generation mechanism based on visualization. *Advanced Materials Research*, Volume 11-12, pp. 705-708.
- Tao, J. & Jiyong, K., 2007. A 3-D point sets registration method in reverse engineering. *Computers and Industrial Engineering*, 53(2), pp. 270-276.
- Taubin, G., 1991. Estimation of planar curves, surfaces, and nonplanar space curves defined by implicit equations with applications to edge and range image segmentation. *IEEE Transactions on Pattern Analysis and Machine Intelligence*, 13(11), pp. 1115-1138.
- Testani, C., Squillace, A. & Fratini, L., 2013. *Beta-forging of Ti6Al4V Titanium Alloy powders consolidated by HIP: Plastic Flow and Strain Rate relation*. Las Vegas, USA, Trans Tech Publications.
- Testani, C. & Tului, M., 2012. Improved Performance in Aerospace Structures with Ti and Ni metal matrix composites. *Materials Science Forum*, Volume 706 – 709, pp. 240-245.
- Thompson, W. B. et al., 1999. Feature-based reverse engineering of mechanical parts. *IEEE Trans. Robot Autom.*, 15(1), pp. 57-66.
- Todd, R. H., Allen, D. K. & Alting, L., 1994. *Manufacturing Processes Reference Guide*. s.l.:Industrial Press.
- Torr, P. H. S. & Zisserman, A., 2000. MLESAC: A New Robust Estimator with Application to Estimating Image Geometry. *Computer Vision and Image Understanding*, 78(1), pp. 138-156.
- Urbanic, R. J. & El Maraghy, W. H., 2009. Using a modified failure modes and effects analysis within the structured design recovery framework. *J. Mech. Des.*, Volume 131:111,005.
- Van Gestel, N., Cuyper, S., Bleys, P. & Kruth, J.-P., 2009. A performance evaluation test for laser line scanners on CMMs. *Optics and Lasers in Engineering*, 47(3), pp. 336-342.

- Várady, T., Facello, M. A. & Terék, Z., 2007. Automatic extraction of surface structures in digital shape reconstruction. *Computer-Aided Design*, 39(5), pp. 379-388.
- Varady, T., Martin, R. R. & Cox, J., 1997. Reverse engineering of geometric models - an introduction. *Computer Aided Design*, 29(4), pp. 255-268.
- Wang, L. & Bi, Z. M., 2010. Advances in 3D data acquisition and processing for industrial applications. *Robotics and Computer-Integrated Manufacturing*, Volume 26, pp. 403-413.
- Wang, T., Li, J. & An, X., 2015. *An Efficient Scene Semantic Labeling Approach for 3D Point Cloud*. s.l., s.n., pp. 2115-2120.
- Wikipedia (EN), 2017. *Wikipedia (EN)*. [Online] Available at: <https://en.wikipedia.org>
- Wolf, K., Roller, D. & Schäfer, D., 2000. An approach to computer-aided quality control based on 3D coordinate metrology. *Journal of Materials Processing Technology*, 107(1), pp. 96-110.
- Xie, P. et al., 2010. Visual experiment study on the influence of mold structure design on injection molding product's defects. *Advanced Materials Research*, Volume 87-88, pp. 31-35.
- Xi, F. & Shu, C., 1999. CAD-based path planning for 3-D line laser scanning. *Computer-Aided Design*, 31(7), p. 473-479.
- Yau, H.-T., Chen, C.-Y. & Wilhelm, R. G., 2000. Registration and integration of multiple laser scanned data for reverse engineering of complex 3D models. *International Journal of Production Research*, 38(2), pp. 269-285.

Annex 1.

List of common plastic material used for injection moulding

Material name	Abbreviation	Trade names	Description and Properties	Common Applications
Acetal (Polyoxymethylene)	POM	Celcon, Delrin, Duracon, Hostaform, Lucel	Strong, rigid, excellent fatigue resistance, excellent creep resistance, chemical resistance, moisture resistance, naturally opaque white, low/medium cost	Bearings, cams, gears, handles, plumbing components, rollers, rotors, slide guides, valves
Acrylic	PMMA	Diakon, Oroglas, Lucite, Plexiglas	Rigid, brittle, scratch resistant, transparent, optical clarity, low/medium cost	Display stands, knobs, lenses, light housings, panels, reflectors, signs, shelves, trays
Acrylonitrile Butadiene Styrene	ABS	Cycolac, Magnum, Novodur, Terluran	Strong, flexible, low mold shrinkage (tight tolerances), chemical resistance, electroplating capability, naturally opaque, low/medium cost	Automotive (consoles, panels, trim, vents), boxes, gauges, housings, inhalors, toys
Cellulose Acetate	CA	Dexel, Cellidor, Setilithe	Tough, transparent, high cost	Handles, eyeglass frames

Material name	Abbreviation	Trade names	Description and Properties	Common Applications
Polyamide 6 (Nylon)	PA6	Akulon, Ultramid, Grilon	High strength, fatigue resistance, chemical resistance, low creep, low friction, almost opaque/white, medium/high cost	Bearings, bushings, gears, rollers, wheels
Polyamide 6/6 (Nylon)	PA6/6	Kopa, Zytel, Radilon	High strength, fatigue resistance, chemical resistance, low creep, low friction, almost opaque/white, medium/high cost	Handles, levers, small housings, zip ties
Polyamide 11+12 (Nylon)	PA11+12	Rilsan, Grilamid	High strength, fatigue resistance, chemical resistance, low creep, low friction, almost opaque to clear, very high cost	Air filters, eyeglass frames, safety masks
Polycarbonate	PC	Calibre, Lexan, Makrolon	Very tough, temperature resistance, dimensional stability, transparent, high cost	Automotive (panels, lenses, consoles), bottles, containers, housings, light covers, reflectors, safety helmets and shields

Material name	Abbreviation	Trade names	Description and Properties	Common Applications
Polyester - Thermoplastic	PBT, PET	Celanex, Crastin, Lupox, Rynite, Valox	Rigid, heat resistance, chemical resistance, medium/high cost	Automotive (filters, handles, pumps), bearings, cams, electrical components (connectors, sensors), gears, housings, rollers, switches, valves
Polyether Sulphone	PES	Victrax, Udel	Tough, very high chemical resistance, clear, very high cost	Valves
Polyetheretherketone	PEEK/PEEK		Strong, thermal stability, chemical resistance, abrasion resistance, low moisture absorption	Aircraft components, electrical connectors, pump impellers, seals
Polyetherimide	PEI	Ultem	Heat resistance, flame resistance, transparent (amber color)	Electrical components (connectors, boards, switches), covers, shields, surgical tools

Material name	Abbreviation	Trade names	Description and Properties	Common Applications
Polyethylene - Low Density	LDPE	Alkathene, Escorene, Novex	Lightweight, tough and flexible, excellent chemical resistance, natural waxy appearance, low cost	Kitchenware, housings, covers, and containers
Polyethylene - High Density	HDPE	Eraclene, Hostalen, Stamylan	Tough and stiff, excellent chemical resistance, natural waxy appearance, low cost	Chair seats, housings, covers, and containers
Polyphenylene Oxide	PPO	Noryl, Thermocomp, Vamporan	Tough, heat resistance, flame resistance, dimensional stability, low water absorption, electroplating capability, high cost	Automotive (housings, panels), electrical components, housings, plumbing components
Polyphenylene Sulphide	PPS	Ryton, Fortron	Very high strength, heat resistance, brown, very high cost	Bearings, covers, fuel system components, guides, switches, and shields

Material name	Abbreviation	Trade names	Description and Properties	Common Applications
Polypropylene	PP	Novolen, Appryl, Escorene	Lightweight, heat resistance, high chemical resistance, scratch resistance, natural waxy appearance, tough and stiff, low cost.	Automotive (bumpers, covers, trim), bottles, caps, crates, handles, housings
Polystyrene - General purpose	GPPS	Lacqrene, Styron, Solarene	Brittle, transparent, low cost	Cosmetics packaging, pens
Polystyrene - High impact	HIPS	Polystyrol, Kostil, Polystar	Impact strength, rigidity, toughness, dimensional stability, naturally translucent, low cost	Electronic housings, food containers, toys
Polyvinyl Chloride - Plasticised	PVC	Welvic, Varlan	Tough, flexible, flame resistance, transparent or opaque, low cost	Electrical insulation, housewares, medical tubing, shoe soles, toys

Material name	Abbreviation	Trade names	Description and Properties	Common Applications
Polyvinyl Chloride - Rigid	UPVC	Polycol, Trosiplast	Tough, flexible, flame resistance, transparent or opaque, low cost	Outdoor applications (drains, fittings, gutters)
Styrene Acrylonitrile	SAN	Luran, Arpylene, Starex	Stiff, brittle, chemical resistance, heat resistance, hydrolytically stable, transparent, low cost	Housewares, knobs, syringes
Thermoplastic Elastomer/Rubber	TPE/R	Hytrel, Santoprene, Sarlink	Tough, flexible, high cost	Bushings, electrical components, seals, washers

